Search for Doubly-charged Higgs Boson Production in the Decay $H^{++}H^{--} \rightarrow \mu^{+}\mu^{+}\mu^{-}\mu^{-}$ with 1.1 fb^{-1} at D0 Detector

by

Tae Jeong Kim

Department of Physics

Graduate School

Korea University

Korea University

The Graduate School

Tae Jeong Kim

We, the dissertation committee for the above candidate for the Doctor of

Philosophy degree, hereby recommend acceptance of the dissertation.

_____

Professor Sung Keun Park
Chairman of Defense

_____

Professor Kwang Souk Sim
Committee Member

_____

Professor Byung Sik Hong
Committee Member

_____

Professor Sun Kee Kim
Committee Member

_____

Professor Suyong Choi
Committee Member

This dissertation is accepted by the Graduate School.

Abstract of the Dissertation

Search for Doubly-charged Higgs Boson

Production in the Decay

$\mathrm{H}^{++}\mathrm{H}^{--} \rightarrow \mu^+\mu^+\mu^-\mu^-$ with 1.1 fb^{-1} at D0 Detector

by

Tae Jeong Kim

Doctor of Philosophy

in

Physics

Korea University

2007

This work presents a search for the pair production of doubly-charged Higgs bosons in the process $\mathrm{p}\bar{\mathrm{p}} \rightarrow \mathrm{H}^{++}\mathrm{H}^{--} \rightarrow \mu^+\mu^+\mu^-\mu^-$ using the data corresponding to an integrated luminosity of about 1.1 fb^{-1}. This is the complete dataset of RunIIa taken from April 19, 2002 to February 22, 2006 by the D0 experiment at the Fermilab Tevatron Collider. In the absence of significant excess above standard model background, 95% confidence level mass limits of $M(\mathrm{H}_L^{\pm\pm}) > 150$ GeV and $M(\mathrm{H}_R^{\pm\pm}) > 126.5$ GeV are set for left-handed and right-handed doubly-charged Higgs bosons respectively assuming a 100% branching ratio into muons.

Contents

List of Figures

viii

x

List of Tables

Acknowledgments

First of all, I would like to thank all the members of the D0 collaboration both their hard work building and operating the detector and for putting up with me for the past years.

I am deeply grateful to my adviser, Sung Keun Park, for giving me the opportunity to be based at the leading particle physics experiment, D0, and repeatedly encouraging me to keep going ahead with confidence. He has given support to me in many ways. There is no way that I would have been able to write this thesis without his support and encouragement.

Suyong Choi deserves a special mention here for giving me the direction to do this analysis, for putting up with me camping out in his office while he taught me how to do physics. He is always willing to spend time to discuss with me about my research progress. He has been an extraordinary teacher to me, both for analysis techniques and phenomenology. I can definitely say that I could not have done this analysis without his constant help. I feel very lucky to work with him.

Special thanks go to the members of the Higgs physics group: Harald Fox, Alexandre Khanov and Gregorio Bernardi for having many discussions in detail to improve this analysis and giving me the many valuable suggestions.

Thanks go to all the faculty and students at Korea University from whom I have learned in the last five years. I would like to thank Kyong Sei Lee for

encouraging me, Kwang Souk Sim for supporting me and Byung Sik Hong for the best particle physics course I have taken.

I would also like to thank all the members of the D0 Korea University group: Seong Jong Hong for giving me the direction how I start to work at Fermi Lab and Sung Hwan Ahn for helping me staying cool in many ways whenever I wanted to smash the computers.

Finally I would like to profusely thank my family. My sisters have always been there for me with patience and my parents have supported me throughout the many years and difficult moments. They have never wavered even though when it seemed that things would not work out and I felt like I would never finish it. I feel extremely grateful to them. I know I would not be getting this degree without them.

Most importantly I would like to thank my lovely friend, Jung Hyun. She has always been caring about me and made me stand this endless hard work. Her willingness to help me make nice figures for my presentations was incredible. She is my beautiful future wife and the wonderful companion. I am eternally grateful to her presence all my life.

Chapter 1

Introduction

In the last decades the standard model has proven enormously successful for describing the known forces, the strong and electroweak interactions, between particles. But it need not be the case that a single Higgs-doublet field is responsible for giving masses to the weakly interacting vector bosons and the fermions. This thesis presents a detailed account of the search for an exotic doubly-charged Higgs boson in the muon final states at D0.

The general layout is as follows. In Chapter 2 we explore the phenomenology of models which contain doubly-charged Higgs bosons, describe its properties, production and decay channels and review several measurements that set a limit on doubly-charged Higgs bosons. Chapter 3 discusses the experimental apparatus used for this analysis, the D0 Run II detector. Chapter 4 describes how the di-muon data sample was selected, while Chapter 5 describes the Monte Carlo simulation of signal and background samples. It also explains all corrections that have to be applied to fix track transverse momenta and smear them in Monte Carlo. The estimation of the QCD background contribution is explained in Chapter 6. The charge flip probability is described in great details

in Chapter 7. The comparison of the data and Monte Carlo is made in Chapter 8. The most important part of the analysis is to understand the like-sign background and third muon background. This is why a discussion of major contributing backgrounds is given in Chapter 8. No search analysis can be made without optimization of selection cuts, an overview is provided in Chapter 9. Chapter 10 describes the candidate events. Chapter 11 shows the limit calculation method. The limits on doubly-charged Higgs boson mass are calculated by taking into account systematic uncertainties listed in Chapter 12. Results and conclusion of this thesis are briefly summarized in Chapter 13. Finally, appendices A and B present some of the studies made before and in the course of performing this analysis. They are included because they all made this search possible. Monitoring and calibration system for the CFT are presented in a great level of detail there.

Chapter 2

Phenomenology of a doubly-charged Higgs boson

In the Standard Model of the electroweak interactions the masses of the fermions and bosons are acquired by the Higgs mechanism. This mechanism results in the existence of an additional particle, the Higgs boson, which, to date, has not been directly observed. Extensions of the Standard Model predict additional Higgs bosons which can be lighter and hence accessible at current experimental facilities. Among these, doubly-charged Higgs bosons, $(\Delta^{++}/\Delta^{--})$[1] , are predicted in many scenarios such as left-right symmetric models [1, 2], higgs triplet models [3] and little Higgs models [4]. The theoretical motivation for the doubly-charged Higgs boson will be covered in this chapter. The current limits from different experiments will be presented. A special attention is paid to the Fermilab Tevatron searches.

---

[1]Doubly-charge Higgs is denoted as Δ^{++}/Δ^{--} in the theoretical literature, it is usually named H^{++}/H^{--} in the experimental papers.

2.1 Doubly-charged Higgs Bosons in extensions of Standard Model

In the last decades an enormously successful model, the standard model, has been developed by particle physicists for describing the elementary particles and forces between them. The standard model plays a key role to unify the electromagnetic force and the weak force into the so-called electroweak force. So far this unification is well known for the biggest success of the standard model. Each force is carried by characteristic particles called bosons. The photon carries the electromagnetic force; it also transmits light. The W and Z bosons represent the weak force.

The electroweak unification results in a problem: it requires all particles which carry forces to be massless like the photon. But experiments show that the W and Z bosons are not massless at all; their mass is comparable to the mass of a gold nucleus.

This problem is solved by introducing a new field, the Higgs field. It interacts with W and Z bosons to give them mass. The Higgs field gives rise to a new particle, called the Higgs boson, which has not yet been observed. It is the keystone of the standard model and finding the Higgs boson is one of the primary goals of the D0 Experiment.

It turns out that the standard model is not the final answer to all our questions since there are phenomena in particle physics for which the standard model makes predictions which contradict basic physical principles. In addition, it just describes many phenomena but does not explain why these phenomena occur. Many of the new theories which try to answer these questions predict the existence of several different Higgs bosons.

One set of models predicts a 'triplet' of Higgs bosons: one neutral Higgs boson, one charged Higgs boson which has the same electric charge as an electron, one 'doubly-charged' Higgs boson which has twice the electric charge of an electron. In this thesis the search for the doubly-charged Higgs bosons has been performed.

We know that models with only Higgs $SU(2)_L \times U(1)_Y$ doublets provide the most straightforward extensions of the SM that satisfy constraints deriving from $\rho \equiv m_W^2 / \cos^2 \theta_W M_Z^2 \approx 1$ and the absence of flavor-changing neutral currents [3]. However, nature might have chosen a more complicated path, leading to several Higgs bosons with different properties. For example, conventional left-right-symmetric models are often constructed using a Higgs sector containing several triplet representations [2]. In those models, it is necessary to assign a very small vacuum expectation value (*v.e.v.*) to the neutral member of the left-handed triplet in order to avoid unacceptable corrections to the $W - Z$ mass ratio. However, it is certainly not necessary to go to left-right-symmetric extensions of the SM in order to consider Higgs-triplet fields. Large tree-level deviations of the electroweak ρ parameter from unity can be avoided by two means:

- the neutral triplet fields can be given *v.e.v* that are much smaller than those for the neutral doublet fields.

- or, the triplet fields and the *v.e.v* of their neutral members can be arranged so that a custodial $SU(2)$ symmetry is maintained.

Only the latter type of models are further considered. By custodial $SU(2)$ symmetry at the tree level is meant that the hypercharges Y and *v.e.v* of all Higgs multiplets are chosen so that $\rho = 1$ is maintained.

A number of models with custodial $SU(2)$ symmetry, have been proposed in the literature [6]. For example, a Higgs doublet representation with $Y = -3$ contains a doubly-charged Δ^{--} and a singly charged Δ^{-}. If part of a multiplet with a neutral member, a Δ^{--} would immediately signal the presence of a Higgs representation with total isospin $T = 1$ or higher. Most popular are the complex $Y = -2$ triplet Higgs representations, such as those required in left-right symmetric models, that contain a Δ^{--}, a Δ^{-} and Δ^{0}.

In assessing the attractiveness of a Higgs sector model containing a Δ^{--} many constraints need to be considered. For triplet and higher representations containing a neutral member, limit on the latter's *v.e.v.* required for $\rho = 1$ at tree-level are generally severe. Models with $T = 1$, $Y = 2$ can have $\rho = 1$ at tree-level by combining representations. However, such models generally require fine-tuning, in order to preserve $\rho = 1$ at one-loop. The simplest way to avoid all ρ problem is to either consider representations that simply do not have a neutral member (e.g. a $Y = -3$ doublet or a $Y = -4$ triplet representation), or else models in which the *v.e.v* is precisely zero. We will only consider models of this type in what follows [3].

Further constraints on Higgs representation arise if we require unification of the coupling constants without intermediate scale physics. In the SM, unification is possible for a relatively simple Higgs sector that includes a single $|Y| = 2$ triplet in combination with either one or two $|Y| = 1$ doublets (the preferred number of doublets depends upon the precise value of $\alpha_s(m_Z)$). In the case of minimal supersymmetric extension of the Standard Model ($MSSM$), precise unification requires exactly two doublet Higgs representations; any extra doublet representations or any number of triplet or higher representations would destroy unification.

In short, the popular two-doublet $MSSM$ [7, 8, 9, 10, 11], need not be nature's choice. We should be on the look-out for signatures of exotic Higgs representations, the clearest of which would be the existence of a doubly-charged Higgs Boson. Thus it is important to understand how to search for and study such a particle.

Naturally, the phenomenology of the Δ^{--} derives from its couplings. Tri-linear couplings of the type $W^- W^- \to \Delta^{--}$ are not present in the absence of an enabling non-zero *v.e.v.* for the neutral member (if present) of the representation, and $q' \bar{q} \Delta^{--}$ couplings are obviously absent. There are always couplings of the form $Z/\gamma \to \Delta^{--} \Delta^{++}$. In addition, and of particular interest, there is the possibility of lepton-number-violating $l^- l^- \to \Delta^{--}$ couplings in some models. For $Q = T_3 + \frac{Y}{2} = -2$ the allowed cases are

$$
\begin{aligned}
l_R^- l_R^- &\to \Delta^{--}(T = 0, \ T_3 = 0, \ Y = -4), \\
l_L^- l_R^- &\to \Delta^{--}(T = \frac{1}{2}, \ T_3 = -\frac{1}{2}, \ Y = -3), \\
l_L^- l_L^- &\to \Delta^{--}(T = 1, \ T_3 = -1, \ Y = -2).
\end{aligned}
\tag{2.1}
$$

Note that the above cases do not include the $T = 3, \ Y = -4$ representation that yields $\rho = 1$, nor the $T = 1, \ Y = -4$ triplet with no neutral member, but do include the $T = \frac{1}{2}, \ Y = -3$ doublet representation with no neutral member, and the popular $T = 1, \ Y = -2$ triplet representation.

In left-right symmetric (LR) electroweak theory [12, 13, 14, 15] the doubly-charged Higgs boson is a member of a triplet Higgs representation which plays a crucial part in the model. The gauge symmetry $SU(2)_L \times SU(2)_R \times U(1)_{B-L}$ of the LR model is broken to the SM symmetry $SU(2)_L \times U(1)_Y$ due to a triplet Higgs Δ_R, whose neutral component acquires a non-vanishing *v.e.v.*. The Δ_R,

called the 'right-handed' triplet, transforms according to $\Delta_R = (1,2,3)$, and it consists of the complex fields Δ_R^0, Δ_R^+ and Δ_R^{++}. If the Lagrangian is assumed to be invariant under a discrete $L - R$ symmetry, it must contain, in addition to Δ_R, also a 'left-handed' triplet $\Delta_L = (\Delta_L^0, \Delta_L^+, \Delta_L^{++}) = (3,1,2)$. Hence the LR model predicts two kinds of doubly-charged particles with different interactions. They are both with $|Y| = 2$. Phenomenologies of the right-handed and left-handed isospin triplets are completely different [16]. In contrast with Δ_R, the existence of Δ_L is not essential from the point of view of the spontaneous symmetry breaking of the gauge symmetry. The *v.e.v.* of its neutral member is actually quite tightly bound by the ρ parameter, i.e. by the measured mass ratio of the ordinary weak bosons.

In the case of a $|Y| = 2$ triplet representation the lepton-number-violating coupling to left-handed leptons is specified by the Lagrangian form [17]

$$\mathcal{L}_Y = ih_{L,ij}\psi_{iL}^T C\tau_2 \Delta_L \psi_{jL} + ih_{R,ij}\psi_{iR}^T C\tau_2 \Delta_R \psi_{jR} + h.c. \qquad (2.2)$$

where $i, j = e, \mu, \tau$ are generation indices, the ψ's are the two-component left-handed(right-handed respectively) lepton fields ($\psi_{lL,R} = (\nu_l, l^-)_{L,R}$) , and Δ is the 2×2 matrix of Higgs fields [6].

$$\Delta_{L,R} = \begin{pmatrix} \Delta_{L,R}^-/\sqrt{2} & \Delta_{L,R}^{--} \\ \Delta_{L,R}^0 & -\Delta_{L,R}^-/\sqrt{2} \end{pmatrix} \qquad (2.3)$$

From the point of view of phenomenology a very important fact is that the $U(1)_{B_L}$ symmetry prevents quarks from coupling to Δ_R and Δ_L [18]. In the process that involve hadrons the triplet Higgses appear therefore only through higher-order corrections.

The Yukawa Lagrangian form 2.2 leads to large Majorana mass terms of

the form $h_{R,ij}\langle\Delta_R^0\rangle\nu_{iR}\nu_{jR}$ for the right-handed neutrinos [19]. These give rise to the see-saw mechanism [19, 20], which provides the simplest explanation to the lightness of ordinary neutrinos, if neutrinos do have a mass.

Apart from the question of neutrino mass, the LR model is more satisfactory than the SM also because it gives a better understanding of parity violation and it maintains the lepton-quark symmetry in weak interactions. Nevertheless, so far there has been no direct evidence of left-right symmetry in weak interactions. This also sets a lower bound to the energy scale of the breaking of that symmetry.

Decays of a Δ^{--} are generally quite exotic [1, 2, 6]. At the Fermilab Tevatron Collider, there are two major production mechanisms. The first mechanism is (Drell-Yan)pair production, $p\bar{p} \to \gamma/Z^0X \to \Delta^{--}\Delta^{++}X$. The second mechanism is single production via WW fusion, $p\bar{p} \to W^-W^-X \to \Delta^{--}X$. However, existing phenomenological and theoretical constraints can be easily satisfied if the $W^-W^- \to \Delta^{--}$ coupling is vanishing (small) [5]. Therefore, in this analysis only $\Delta^{--}\Delta^{++}X$ pair production is considered.

For a vanishing $\Delta^{--} \to W^-W^-$ coupling, the only two-body decays that might be important are $\Delta^{--} \to \Delta^-W^-, \Delta^{--} \to \Delta^-\Delta^-$ and, if the lepton coupling is present, $\Delta^{--} \to l^-l^-$. Typically, the Δ^{--} and Δ^{++} have similar masses, in which case $\Delta^{--} \to \Delta^-\Delta^-$ is likely to be disallowed. Thus, the focus is on the Δ^-W^- and l^-l^- final states. Decays into $\Delta^\pm$ would only be relevant if the singly-charged Higgs boson is lighter than the doubly-charged Higgs boson. In many models, it is possible for the Δ^{--} to couple to like-sign lepton pairs, l^-l^-. If the $W^-W^- \to \Delta^{--}$ coupling is vanishing (or very small), it is then very likely that the doubly-charged Higgs will dominantly decay to like-sign leptons via the lepton-number-violation coupling.

The dominant final states are therefore expected to be like-sign lepton pairs. The possible decay modes are decays in the e, μ and τ channel. Since these decays violate lepton flavor conservation, decay modes with mixed lepton flavor are also possible. Left-handed and right-handed states are distinguished by their decays into left-handed leptons or right-handed leptons. An exact measurement of the branching ratio for this kind of decay process gives a very impressive limit on the coupling constant.

For a $T = 1, Y = -2$ triplet we find [1, 2, 6]

$$\Gamma_{\Delta^{--}}^{\Delta^- W^-} = \frac{g^2}{16\pi} \frac{M_{\Delta^{--}}^3 \beta^3}{m_W^2} \sim (1.3 \text{ GeV})(\frac{m_{\Delta^{--}}}{100 \text{ GeV}})^3 \beta^3 \tag{2.4}$$

$$\Gamma_{\Delta^{--}}^{l^- l^-} = \frac{|h_{ll}|^2}{8\pi} M_{\Delta^{--}} \sim (0.4 \text{ GeV})(\frac{c_{ll}}{10^{-9}})(\frac{m_{\Delta^{--}}}{100 \text{ GeV}})^3 \tag{2.5}$$

where β is the usual phase space suppression factor, and h_{ll} stands for

$$|h_{ll}| \equiv c_{ll} m_{\Delta^{--}}^2 (\text{GeV}) \tag{2.6}$$

with c_{ll} a dimensionless coupling constant to be estimated from the experiment. The Higgs bosons are therefore short-lived (in an experimental sense) unless the coupling h_{ll} are very small (less than 10^{-9}). These constants are the subject of a further discussion in this paper. Their relative ratio provides an insight into the branching ratios of $\Delta^{--} \to l^- l^-$ into $l = e, \mu$ or τ.

Alternatively, if the $\Delta^{--} \to l^- l^-$ and $\Delta^{--} \to W^- W^-$ couplings are both vanishing or very small, then the Δ^{--} can have a sufficiently long lifetime that it will decay outside the detector. Identification of the $\Delta^{--}\Delta^{++}$ pair via the associated dE/dx distributions in the tracker would then be possible.
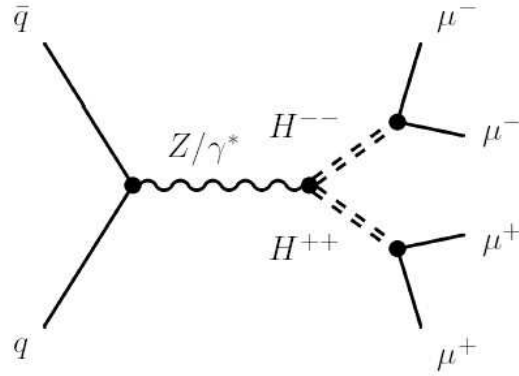
Figure 2.1: Leading order diagram for the pair production of doubly-charged Higgs bosons in p$\bar{\text{p}}$ scattering, where both Higgs bosons decay into muons.

2.2 Experimental limits on the doubly-charged Higgs bosons

The contribution of a doubly-charged Higgs boson Δ^{--}/Δ^{++} exchange in several physics processes was considered in this chapter. It was demonstrated that the effective Hamiltonian that is typically used to interpret the results of muonium-antimuonium oscillation experiment also describes the t-channel exchange of a Δ^{--} [17]. And a limit on the existence of the Δ^{--} can be extracted from the most recent muonium oscillation results [16]. The effect of Δ^{--} exchange on high-energy Bhabha scattering is discussed, and a limit is extracted from the published cross sections of several experiments at SLAC, DESY, as well as LEP searches at OPAL and L3 [16]. The case of a non-diagonal coupling of the Δ^{--} to the charged leptons (non-diagonal in lepton

flavor) is considered. A limit is extracted from the result of the most recent search for the most recent search for the rare decay $\mu \to 3e$ [16]. Finally, the contribution to the anomalous magnetic moment of the muon $(g - 2)_\mu$ is discussed and the limit is derived from very recent measurement published by the Muon $(g-2)$ Collaboration in Brookhaven [21]. These measurements represent indirect searches for a doubly-charged Higgs boson, it is possible however, to search for Δ^{--} directly. Limits from LEP experiments are given [53, 54]. This thesis presents a direct search for a doubly-charged Higgs in the muon channel at D0.

2.2.1   Indirect signals

Low-energy bounds on the doubly-charged Higgs can be derived from the good agreement between theory and experiment in many process expected in the Standard Model, and from non-observation of reactions which are forbidden or suppressed in the SM. These processes represent indirect signals for a doubly-charged Higgs, from their results are derived present low-energy bounds on the doubly-charged Higgs couplings and mass.

A. Muonium-Antimuonium transitions

The origin of the apparent family structure of all known fermions is a complete mystery. It has been known since the discovery of the kaon that the weak eigenstates of the quark sector do not respect this family structure. However, no analogous behavior has ever been observed in the lepton sector. Most searches for lepton-flavor violation have concentrated upon processes

which change lepton flavor L_f by one unit (e.g. $K \to \mu e$ or $\mu \to e\gamma)^2$. There have been relatively few searches done for those processes that change lepton flavor by two units.

An example of such a transition is the process $e^+ e^- \to \mu^- \mu^-$, or the transformation of muonium $(\mu^+ e^- \equiv \bar{M})$. The latter process is the exact analog of neutral kaon mixing. There is a number of physical models that incorporate lepton-flavor-changing processes. Feynman diagram for three processes that mediate the conversion of muonium into antimuonium are shown in Figure 2.2.

Figure 2.2 (a) represents the second-order exchange of ordinary massive Dirac neutrinos. Since the external (lepton) masses are at least as large as the internal (neutrino) masses, this process is more analogous to $B^0 - \bar{B}^0$ mixing than to neutral-kano mixing. Several authors have calculated the effective Hamiltonian for B-meson mixing. Changing quark labels to lepton labels, we can write that the effective Hamiltonian for second-order neutrino exchange is given by the expression [22]

$$\mathcal{H}_{eff} = \frac{G_A}{\sqrt{2}} \bar{\psi}_\mu \gamma^\alpha (1 + \gamma_5) \psi_e \bar{\psi}_\mu \gamma_\alpha (1 + \gamma_5) \psi_e$$
$$+ \frac{G_B}{\sqrt{2}} \bar{\psi}_\mu \gamma^\alpha (1 - \gamma_5) \psi_e \bar{\psi}_\mu \gamma_\alpha (1 - \gamma_5) \psi_e + h.c. \qquad (2.7)$$

where the coupling constants G_A and G_B are complicated functions of lepton masses, neutrino masses and mixing angles.

The process presented in Figure 2.2 (b) is quite similar to that represented by Figure 2.2(a) except that Majorana neutrinos are exchanged instead of Dirac ones. The limit on the coupling constant can be derived from the absence

---

[2] A change of lepton flavor ΔL_f is defined as the change in lepton number for each species of lepton.
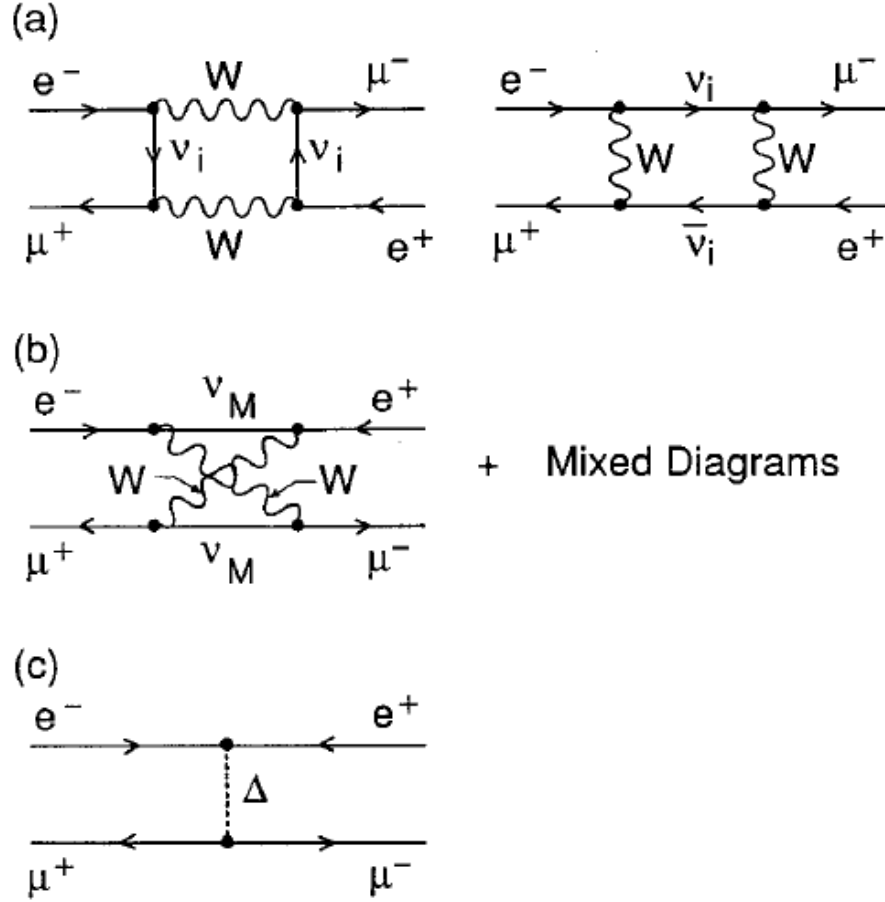
Figure 2.2: Three possible subprocesses for muonium to antimuonium conversion. (a) represents a second-order exchange of ordinary Dirac neutrinos. (b) is a similar process but with Majorana neutrinos instead. (c) represents the t-channel exchange of a doubly-charged Higgs boson. All diagrams can be reordered to describe the process $e^-e^- \rightarrow \mu^-\mu^-$.

of neutrinoless double-beta decay [23].

The third process shown in Figure 2.2 (c) involves the t-channel exchange

of a doubly-charged Higgs boson.

The mass of the doubly-charge Higgs boson M_Δ is certainly large on the scale of the momentum transfer that is associated with muonium to antimuonium oscillation. The effective Hamiltonian for $M-\bar{M}$ conversion can therefore be written as [17]

$$\mathcal{H}_\Delta = \frac{g_{ee}g_{\mu\mu}}{8M_\Delta^2}\bar{\psi}_\mu\gamma^\alpha(1+\gamma_5)\psi_e\bar{\psi}^\mu\gamma_\alpha(1+\gamma_5)\psi_e + h.c. \tag{2.8}$$

with the coupling constant defined as

$$G_{M\bar{M}} \equiv \frac{g_{ee}g_{\mu\mu}}{4\sqrt{2}M_\Delta^2} = \frac{g_{ee}g_{\mu\mu}}{g^2}[\frac{M_W}{M_\Delta}]^2 G_F \tag{2.9}$$

where g is the $SU(2)$ coupling constant and M_W is the W boson mass. Using Equation 2.9, the current limit on $G_{M\bar{M}}$ can be converted into a limit on the ratio of couplings to M_Δ^2 (at 90% CL) [24]

$$\frac{g_{ee}g_{\mu\mu}}{M_{\Delta^{++}}^2} \leq 5.8 \times 10^{-5} \text{ GeV}^{-2}. \tag{2.10}$$

Processes that exhibit lepton flavor violation may be the most spectacular to contemplate but are not necessarily the most sensitive ones to use in experimental searches.

B. Bhabha scattering

The doubly-charged Higgs boson could contribute to both Bhabha and Moller scattering, even if they were too heavy to be directly produced at the given collider energy. They can therefore be detected via deviations from the SM expectations for the total cross sections and angular correlations. In the

presence of off-diagonal flavor couplings, they may even produce states which are not expected in the realm of the standard model.

Doubly-charged scalar Higgs boson contribution to Bhabha scattering at the tree level, shown in Figure 2.3, involves the t-channel exchange of a Δ^{--}. Moller scattering involves the s-channel exchange which is experimentally less interesting.
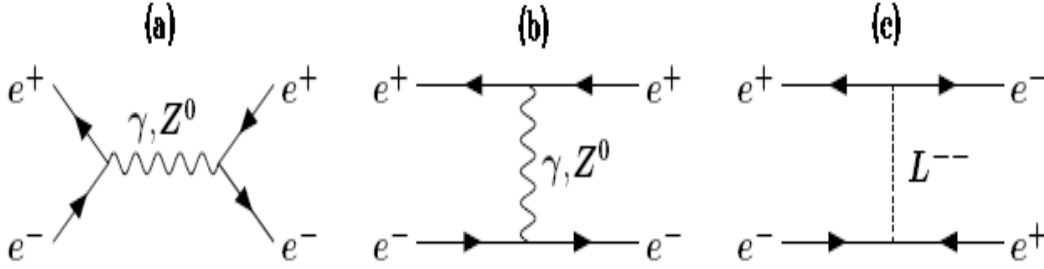
Figure 2.3: Lowest order Feynman diagrams contributing to $e^+e^- \rightarrow e^+e^-$ scattering. (c) The contribution from doubly-charged Higgs is given in the third diagram.

If we assume that M_Δ is large as compared with the center-of-mass energy of the scattering process, the effective Hamiltonian for Bhabha scattering process can be written as [25]

$$\mathcal{H}_{Bhabha} = \frac{g_{ee}^2}{2M_\Delta^2}\bar{\psi}_{eR}\gamma^\alpha\psi_{eR}\bar{\psi}_{eR}\gamma_\alpha\psi_{eR} + h.c. \tag{2.11}$$

where we have chosen to express all fields as chiral fields. From Equation 2.11 is trivial to extract the cross section for unpolarized Bhabha scattering [25]

$$\sigma_{Higgs}(\cos\theta) \equiv \frac{d\sigma}{d(\cos\theta)}$$

$$= \frac{\pi\alpha^2}{4s}[4A_0 + A_-(1-\cos\theta)^2 \tag{2.12}$$

$$+A_+(1+\cos\theta)^2], \tag{2.13}$$

where the coefficients A_0, A_- and A_+ are defined as

$$A_0 = [\frac{s}{t}]^2|1 + \frac{g_r g_l}{e^2}\frac{t}{t_Z}|^2,$$

$$A_- = |1 + \frac{g_r g_l}{e^2}\frac{s}{s_z}|^2,$$

$$A_+ = \frac{1}{2}|1 + \frac{s}{t} + \frac{g_r^2}{e^2}[\frac{s}{s_z} + \frac{s}{t_z}] + \frac{2g_{ee}^2 s}{e^2 M_\Delta^2}|^2$$

$$+\frac{1}{2}|1 + \frac{s}{t} + \frac{g_l^2}{e^2}[\frac{s}{s_z} + \frac{s}{t_z}]|^2. \tag{2.14}$$

The various quantities used in Equation 2.13 are defined as follows: θ is the scattering angle in the center of mass (c.m.) frame; s is the square of the c.m. frame energy; $t = -s(1-cos\theta)/2$; $s_Z = s - M_Z^2 + iM_Z\Gamma_Z$ (M_Z and Γ_Z are the mass and decay width of the Z^0 boson, respectively); $t_Z = t - M_Z^2 + iM_Z\Gamma_Z$; $g_r = e\tan\theta_W$ (e and θ_W are the electric charge and electroweak mixing angle, respectively); and $g_l = -e\cot 2\theta_W$.

Equation 2.13 is valid only for the case $M_\Delta^2 \gg s$. If s is comparable to or larger than M_Δ^2, the coefficient A_+ must be modified to account for effect of the Δ^{--} propagator.

From the Bhabha scattering cross-section at SLAC [26, 27] and DESY [28, 29] the following bound on the g_{ee} was established

- at 90% confidence limit:

$$\frac{g_{ee}^2}{M_{\Delta^{++}}^2} \leq 8.0 \times 10^{-6} \text{ GeV}^{-2} \tag{2.15}$$

- at 95% confidence limit:

$$\frac{g_{ee}^2}{M_{\Delta^{++}}^2} \leq 9.7 \times 10^{-6} \text{ GeV}^{-2} \tag{2.16}$$

C. Muon decays

Many of the best limits on lepton-flavor violation come from searches for rare decay modes of the muon [30]. If the coupling of the doubly-charged Higgs is purely diagonal in the lepton flavor as described in Equation 2.2, the Δ^{--} does not mediate muon decay at the tree level.

We consider the case when the doubly-charged Higgs boson couples non-diagonally to the charged-lepton sector [31, 32]. In such a case, the doubly-charged Higgs can mediate the decay $\mu \to e^- e^+ e^-$. This process is shown in Figure 2.4.

A very stringent coupling constant limit can be obtained from an existing limit on branching ratio for the $\mu \to 3e$ process [33].

The non-diagonal coupling can be defined by the following Lagrangian form [34]

$$\mathcal{L} = \frac{g_{e\mu} g_{ee}}{8 M_\Delta^2} \bar{\psi}_\mu \gamma^\alpha (1 + \gamma_5) \psi_e \bar{\psi}_e \gamma_\alpha (1 + \gamma_5) \psi_\mu + h.c. \tag{2.17}$$

where the coupling constant $g_{e\mu}$ is presumably suppressed by the sine of a mixing angle as compared to the regular diagonal coupling constants.

Equation 2.17 can be used to calculate the $\mu \to 3e$ branching ratio [17]
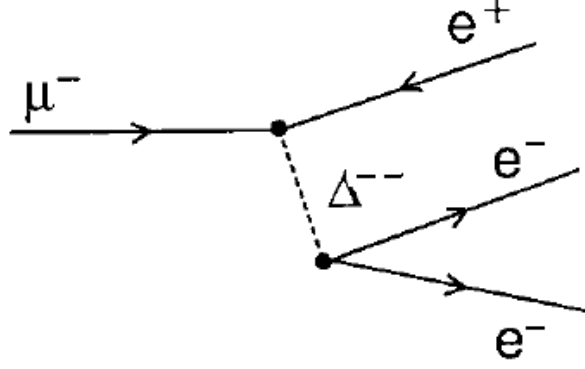
Figure 2.4: The decay $\mu \to e^- e^+ e^-$ mediated by a Δ^{--}.

$$
\begin{aligned}
BR(\mu \to 3e) &\equiv \frac{\Gamma(\mu^+ \to e^- e^+ e^-)}{\Gamma(\mu^- \to e^- \nu_\mu \bar{\nu}_e)} \\
&= \frac{g_{e\mu}^2 g_{ee}^2}{16 G_F^2 M_\Delta^4} \\
&= 2 \left[\frac{g_{e\mu} g_{ee}}{g^2}\right]^2 \left[\frac{M_W}{M_\Delta}\right]^4.
\end{aligned}
\tag{2.18}
$$

The best published limit on the branching ratio of $\mu \to 3e$ is $BR(\mu \to 3e) < 6.8 \times 10^{-13}$ at 90% confidence level [36]. The limit on $g_{e\mu} g_{ee}/M_\Delta^2$ can be found using Equation 2.19 [37]

$$
\frac{g_{e\mu} g_{ee}}{M_{\Delta^{++}}^2} \leq 3.2 \times 10^{-11} \text{ GeV}^{-2}
\tag{2.19}
$$

This appears to be the most stringent limit on the existence of doubly-charged Higgs boson.

Another interesting lepton-flavor violation process is the radiative muon decay, $\mu \to e\gamma$ [38, 39, 40, 41]. This process is forbidden in the SM, but it can

be mediated at the one-loop level by doubly-charged Higgs boson as depicted in Figure 2.5.
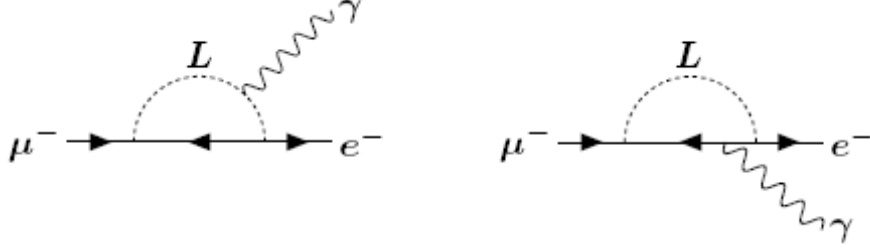
Figure 2.5: The radiative muon decay $\mu \to e\gamma$ mediated by $\Delta^{\pm\pm}$ (labeled as L because contribution from a singly-charged Higgs (L=$\Delta^{\pm\pm}$ or $\Delta^{\pm}$) is possible too).

The branching ratio of the radiative decay is indeed constrained to be very small [42]

$$BR(\mu \to e\gamma) \leq 4.0 \times 10^{-11} \tag{2.20}$$

However, one should keep in mind that being this a one-loop process, the matrix element is suppressed by a factor $(1/4\pi)^2$. This is why decay $\mu \to 3e$ gives a stronger bound. Nevertheless, $\mu \to e\gamma$ applies to different combinations of generation indices, because one can observe any lepton flavor in the loop. That makes this process to be equally interesting.

From non-observation of this decay follows [36, 37]

$$\frac{g_{e\mu}g_{\mu\mu}}{M^2_{\Delta_{++}}} \leq 2.0 \times 10^{-10} \ \ \text{GeV}^{-2} \tag{2.21}$$

D. Anomalous magnetic moment of the muon

The anomalous magnetic moment of the electron and the muon are two of the most accurately measured quantities in physics. The Muon $(g-2)$ Collaboration in Brookhaven has measured the anomalous magnetic moment of the negative muon $a_\mu = (g-2)/2$ to a precision of 0.7 parts per million (ppm) at the Brookhaven Alternation Gradient Synchrotron (AGS) [43].

The measurement is based on muon spin precession in a magnetic storage ring with electrostatic focusing [44, 45, 46, 47, 48]. Protons from AGS are sent on a fixed target, where pions are produced dominantly. They decay into muons in-flight ($c\tau$ of a pion is 6.7 m). Muons are fed into a uniform, doughnut-shaped magnetic field and travel in a circle (central orbit radius is 7.11 m). After each circle, muon's spin axis changes by 12°, and it keeps on precessing in the same direction (precession period is 4.37 μs). After circling the ring many times, muons spontaneously decay to electron (plus neutrino) in the direction of the muon spin.

Inside the ring, there are 24 scintillating counter detectors on the inside of the ring. The $(g-2)_\mu$ parameter is then azimuthal angle measured between electron direction of flight and muon momentum orientation, divided by the magnetic field $B = 1.45$T the muon is traveling through in the ring.

The $(g-2)_\mu$ value of the negative muon magnetic anomaly was announced on January 8, 2004.

The published experimental value is [21]

$$
\begin{aligned}
a_{\mu^-}(BNL2001) &= 1165214(8)(3) \times 10^{-10}(0.7ppm) \\
a_{\mu^-(exp)} &= 11659208(6) \times 10^{-10}(0.5ppm)
\end{aligned}
\tag{2.22}
$$

in which the total uncertainty consists of 5×10^{-10} (0.4 ppm) statistical uncertainty and 4×10^{-10} (0.3 ppm) systematic uncertainty.

SM prediction for a_μ consists of QED, hadronic and weak contributions. The uncertainty on the SM value is dominated by the uncertainty on the lowest-order hadronic vacuum polarization. The same can be determined indirectly using hadronic τ decay data [49]. In principle, the τ data should even improve the precision of a_μ(had) measurement. However, discrepancies between the τ and the e^+e^- results exist. These two data sets do not give consistent results for the pion form factor. Using the annihilation of e^+e^- to hadrons data gives the corresponding theoretical value [50]

$$a_{\mu-}(SM) = 11659181(8) \times 10^{-10}(0.7ppm) \tag{2.23}$$

The number deduced from τ decay is larger by 15×10^{-10}. The difference between the experimental determination of a_μ and the SM theory using the e^+e^- or τ data for the calculation of the hadronic vacuum polarization is 2.7σ and 1.4σ, respectively [21].

The new physics contribution could be of the order of

$$\delta(a_{\mu-}(exp) - a_{\mu-}(SM)) = 2.7\sigma = 2.7 \times 10^{-9}. \tag{2.24}$$

As we will see, these constraints are not particularly strong. The $(g-2)/2$ unlike other low energy bounds are square of a coupling constant.

There are two one-loop Feynman diagrams mediated by doubly-charged Higgs that could contribute to $(g-2)$. They are given in Figure 2.6.

The contribution of both diagrams has been evaluated [34]. They contribute to $a_{\mu-}$ as [35]
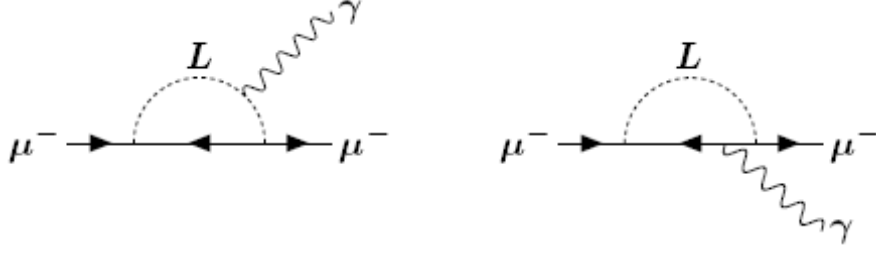
Figure 2.6: One-loop diagrams mediated by doubly-charged Higgs bosons that contribute to $(g-2)$ (labeled as L because contribution from a singly-charged Higgs is easily possible too).

$$a_{\mu^-} = -\frac{3h_{\mu\mu}^2 m_\mu^2}{16\pi M_{\Delta^2}}$$

(2.25)

If one assumes that the total discrepancy between the SM and $(g-2)$ measurement is caused by extra contribution from $\Delta^{\pm\pm}$ bosons, the limit on the coupling is the following

$$\frac{g_{\mu\mu}^2}{M_{\Delta^{++}}^2} \leq 4.0 \times 10^{-6} \text{ GeV}^{-2}.$$

(2.26)

2.2.2 Direct signals

When the doubly-charged Higgs bosons are obtained from the study of virtual processes, the limits on the existence of the signal have the property that the limit on the mass M_Δ is correlated with the size of the coupling g_{ll}. This correlation could be removed by searching for the production of real $\Delta^{--}\Delta^{++}$ pairs. The direct signal process $e^+e^- \to \Delta^{++}\Delta^{--}$ would produce rather spectacular four-lepton events (such as $\mu^-\mu^-\mu^+\mu^+$ combinations). This section re-

views coupling-independent limits from published measurements of the process $e^+e^- \to 4l$ (by LEP experiments) and it provides an insight into calculating of the NLO cross-section for the doubly-charged Higgs boson production at Tevatron and LHC.

A. Limits from $e^+e^- \to \Delta^{++}\Delta^{--} \to 4l$ searches at LEP

The tree level differential cross section for the process $e^+e^- \to \Delta^{++}\Delta^{--}$ is given by the expression [6]

$$\frac{d\sigma}{d(cos\theta)} = \frac{\pi\alpha^2 Q_\Delta^2}{4s} \sin^2\theta [1 - \frac{4M_\Delta^2}{s}]^{3/2}, \qquad (2.27)$$

where $\sqrt{s}$ is the total center of mass frame energy of the e^+e^- system; θ is the polar angle of the outgoing Δ^{--} with respect to the incident electron direction; and Q_Δ is the charge of the Higgs boson ($Q_\Delta = 2$). The total cross section for the process can therefore be written as [17]

$$\sigma = \frac{4\pi\alpha^2}{3s} [1 - \frac{4M_\Delta^2}{s}]^{3/2}. \qquad (2.28)$$

In the limit $M_\Delta/s \to 0$, the total cross section is equal to the cross section for the production of muon pairs.

Each of the Higgs bosons then decays into a same-sign pair of leptons with a characteristic decay width $\Gamma^{l\pm\pm}$ that is described by Equation 2.5. For a mass $M(\Delta^{\pm\pm})$ of about 100 GeV/c^2, Yukawa couplings of $h_{\mu\mu} < 0.5$ are still allowed. The requirement that the $\Delta^{\pm\pm}$ is not stable and decays within $\simeq$ 1 cm then according to Equation 2.5 corresponds to $h_\mu\mu > 10^{-7}$.

Direct searches were performed by the OPAL, L3 and DELPHI collaborations at LEP in e^+e^- scattering. From $e^+e^- \to \Delta^{++}\Delta^{--} \to 4l$ searches at

LEP, mass limits of $M(\Delta_L^{\pm\pm}) > 100.5$ GeV/c^2 and $M(\Delta_R^{\pm\pm}) > 100.1$ GeV/c^2 were obtained by OPAL [51] and a limit of $M(\Delta_{L(R)}^{\pm\pm}) \geq 99.4$ GeV by L3 [52], assuming a 100% branching ratio into muons[3].

The lower limit for left- or right- handed doubly-charged Higgs bosons decaying via any single lepton channel $\Delta^{\pm\pm} \to ll(l = \tau, \mu, e)$, assuming a 100% branching ratio in that channel, is $M_{\Delta^{\pm\pm}} > 98.5$ GeV/c^2 (OPAL) and 97.3 GeV/c^2 (L3). DELPHI has searched in the channel $\Delta^{\pm\pm} \to \tau^\pm \tau^\pm$, obtaining a limit of $M_{\Delta^{\pm\pm}} > 97.3$ GeV/c^2 [53].

OPAL has also searched for the production of single doubly-charged Higgs bosons, which constrains the Yukawa coupling to elections, h_{ee}, to be less than 0.071 for $M(H^\pm) < 160$ GeV/c^2 [54].

B. Doubly-charged Higgs searches at Tevatron and LHC

At hadron colliders, the lowest order (LO) partonic cross section for doubly-charged Higgs boson pair production is given by

$$\hat{\sigma}_{LO}(q\bar{q} \to \Delta^{++}\Delta^{--}) = \frac{\pi\alpha^2}{9Q^2}\beta^3[e_q^2 e_\Delta^2 + \frac{e_q e_\Delta \nu_q \nu_\Delta (1 - M_Z^2/Q^2) + (v_q^2 + a_q^2)\nu_\Delta^2}{(1 - M_Z^2/Q^2)^2 + M_Z^2\Gamma_Z^2/Q^4}]$$

(2.29)

with $\nu = (2\ I_{3q} - 4\ e_q s_W^2)/(2\ s_W c_W)$, $a_q = 2\ I_{3q}/(2\ s_W c_W)$ and $\nu_\Delta = (2\ I_{3\ \Delta} - 2\ e_\Delta s_W^2)/(2\ s_W c_W)$, where $I_{3q}(I_3\Delta)$ denotes the third isospin component and $e_q(e_\Delta)$ the electric charge of the quark q (doubly-charged Higgs boson Δ^{--}) and $s_W = \sin\theta_W, c_W = \cos\theta_W$. Q^2 is the squared partonic center of mass frame energy, α is the QED coupling evaluated at the scale Q, M_Z the Z boson mass and Γ_Z the Z boson width. The Higgs velocity is defined

---

[3]All limits in this note are given at 95% CL, unless specified otherwise.

as $\beta = \sqrt{1 - 4M_\Delta^2/Q^2}$.

The hadronic cross sections can be obtained from convolution the partonic cross section with the corresponding (anti)quark densities of the (anti)protons

$$\sigma_{LO}(pp/p\bar{p} \to \Delta^{++}\Delta^{--}) = \int_{\tau_0}^{1} d\tau \sum_q \frac{d\mathcal{L}^{q\bar{q}}}{d\tau} \hat{\sigma}_{LO}(Q^2 = \tau s) \qquad (2.30)$$

where $\tau_0 = 4\ M_\Delta^2/s$ with s being the total hadronic center of mass energy squared, and $\mathcal{L}^{q\bar{q}}$ denotes the $q\bar{q}$ parton luminosity.

Next-to-leading order (NLO) QCD corrections to the $\Delta^{++}\Delta^{--}$ pair production cross-section have recently been calculated [55]. Both at the Tevatron and the LHC, QCD corrections are found to be of moderate size. They increase the LO cross section by about 20–30%. The residual theoretical uncertainties are of the order of 10–15% which is sufficient for experimental searches for these particles at the Tevatron and LHC.

The standard QCD corrections are: virtual gluon splitting, gluon emission and quark emission. They are identical to corrections applied in case of the Drell-Yan process.

The LO cross section is modified as follows [55]

$$\begin{aligned}
\sigma &= \sigma_{LO} + \Delta\sigma_{q\bar{q}} + \Delta\sigma_{q\bar{g}} & (2.31)\\
\Delta\sigma_{q\bar{q}} &= \frac{\alpha_s(\mu R)}{\pi} \int_{\tau_0}^{1} d\tau \sum_q \frac{d\mathcal{L}^{q\bar{q}}}{d\tau} \int_{\tau_0/\tau}^{1} dz \hat{\sigma}_{LO}(Q^2 = \tau z s) w_{q\bar{q}}(z)\\
\Delta\sigma_{q\bar{g}} &= \frac{\alpha_s(\mu R)}{\pi} \int_{\tau_0}^{1} d\tau \sum_q \frac{d\mathcal{L}^{q\bar{g}}}{d\tau} \int_{\tau_0/\tau}^{1} dz \hat{\sigma}_{LO}(Q^2 = \tau z s) w_{q\bar{g}}(z)
\end{aligned}$$

where the coefficient functions can be expressed as [56]

$$w_{q\bar{q}}(z) = -P_{qq}(z)ln\frac{\mu_F^2}{\tau_s} + \frac{4}{3}\{[\frac{\pi^2}{3} - 4]\delta(1-z) + 2(1+z^2)(\frac{ln(1-z)}{1-z})_+\}$$

$$w_{q\bar{g}}(z) \quad = \quad -\frac{1}{2}P_{qg}(z)ln(\frac{\mu_F^2}{(1-z)^2\tau s}) + \frac{1}{8}(1 + 6z - 7z^2) \qquad (2.32)$$

and where μ_F denotes the factorization scale, μ_R the renormalization scale and P_{qq}, P_{qg} the splitting functions [57]

$$P_{qq}(z) \quad = \quad \frac{4}{3}\{\frac{1+z^2}{(1-z)_+} + \frac{3}{2}\delta(1-z)\}$$

$$P_{qg(z)} \quad = \quad \frac{1}{2}\{z^2 + (1-z)^2\}. \qquad (2.33)$$

The numerical results were calculated by Margarete Mühlleitner and Michael Spira using CTEQ6L1 (CTEQ6M) parton densities at next-to-leading order with the strong coupling α_s adjusted accordingly, i.e. $\alpha_s^{LO}(M_Z) = 0.130$, $\alpha_s^{NLO}(M_Z) = 0.118$. The electroweak quantum numbers of the doubly-charged Higgs boson Δ^{--} have been chosen to be isospin $I_{3\Delta} = -1$ and charge $Q_\Delta = -2$.

The NLO cross section at the Tevatron for the left- and right-handed states, and the ratio between the NLO and LO cross-section (K-factor) as a function of $M(\Delta^{\pm\pm})$ are shown in Figure 2.7 .

The renormalization and factorization scale has been chosen as $\mu_F^2 = \mu_R^2 = Q^2$ which is the natural scale choice for Drell-Yan like processes.

For comparison, Figures 2.8 and 2.9 show the cross section and K-factor $(K = \sigma_{NLO}/\sigma_{LO})$ as function of doubly-charged Higgs mass. The curve for the Tevatron is truncated at $M_\Delta = 500$ GeV/c^2, since the cross section gets too small above and it thus phenomenologically irrelevant.

The QCD corrections increase the LO cross section by 20-30% which can be inferred from Figure 2.9. The residual renormalization and factorization scale dependence at NLO amounts to about 5-10% and it serves as an estimate of

the theoretical systematical uncertainty in this analysis. This uncertainty is comparable to NNLO corrections. The uncertainties of the parton densities have to be added. This why the final theoretical uncertainty on the NLO cross section amounts to 10–15% [55].
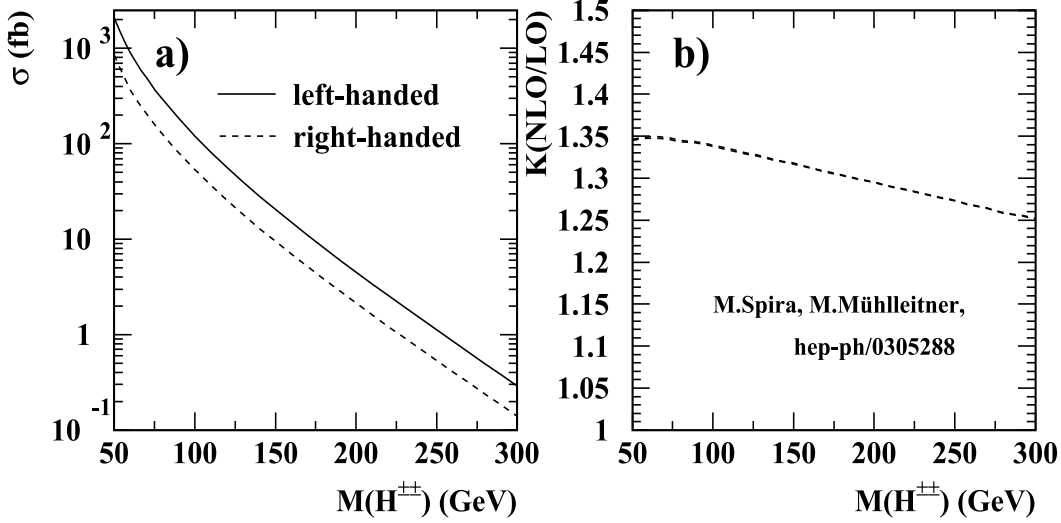
Figure 2.7: Tevatron: (a) NLO cross-sections and (b) ratio of the NLO to LO cross-sections as a function of the mass of the doubly-charged Higgs boson, $M(\Delta^{\pm\pm})$ [55].

The pair production cross-section for left-handed doubly-charged Higgs bosons in the mass range $100 < M(\Delta^{\pm\pm}) < 200$ GeV/c^2 is about a factor two larger than for the right-handed states due to different coupling to the intermediate Z boson.

The search for doubly-charged Higgs boson decaying into muons via the process $q\bar{q} \rightarrow \gamma^*/Z \rightarrow \Delta^{++}\Delta^{--} \rightarrow \mu^+\mu^+\mu^-\mu^-$ is presented in this thesis. The leading-order diagram is shown in Figure 2.1.

Using dimuon events with muons of opposite charge, which originate mainly

from $Z \to \mu^+\mu^-$ decays, the experimental sensitivity to a possible $\Delta^{\pm\pm}$ signal was studied. A search for doubly-charged Higgs production in muon final states is then performed by selection events that contain like-charged muon pairs and one third muon.
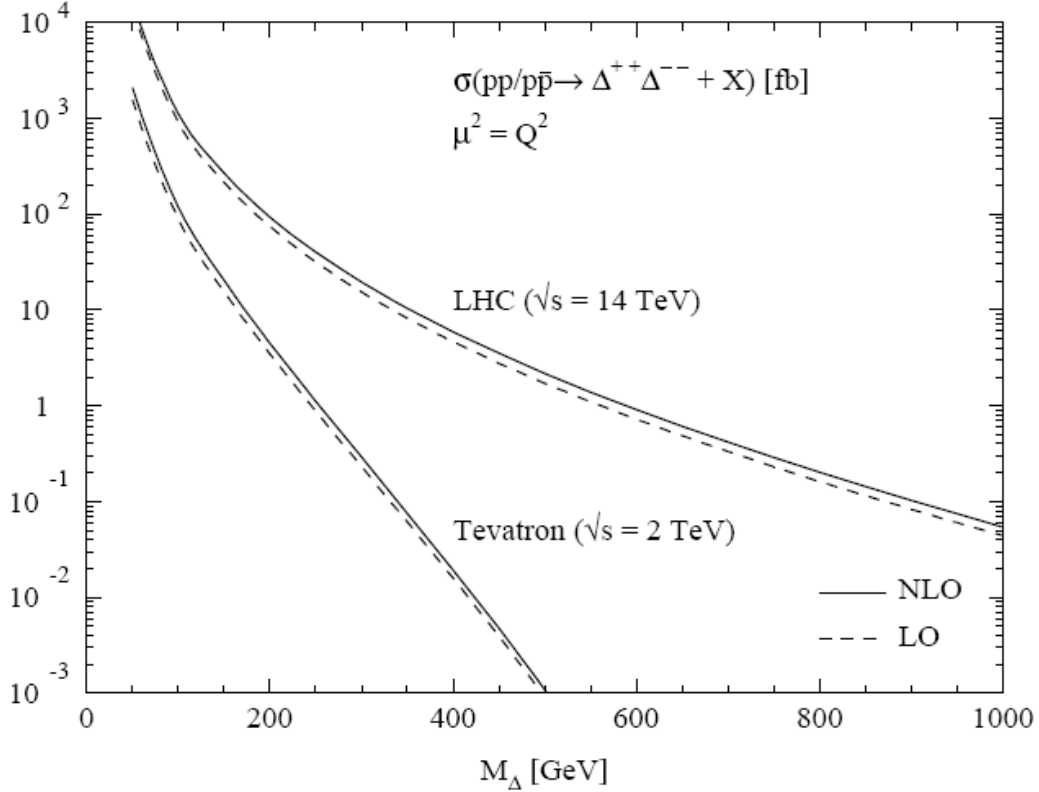
Figure 2.8: Production cross sections of doubly-charged Higgs pair production at the Tevatron and the LHC as a function of its mass [55].

A previous search by the D0 collaboration in the $\mu\mu$ channel has excluded H_L^{++} below a mass of 118 GeV/c^2 and $H_R^{\pm\pm}$ bellow a mass of 98.2 GeV/c^2 [92]. With 240 pb^{-1} of $p\bar{p}$ collision data collected by the CDF II experiment a search for doubly-charged Higgs boson by the CDF collaboration in $\mu\mu$ channel
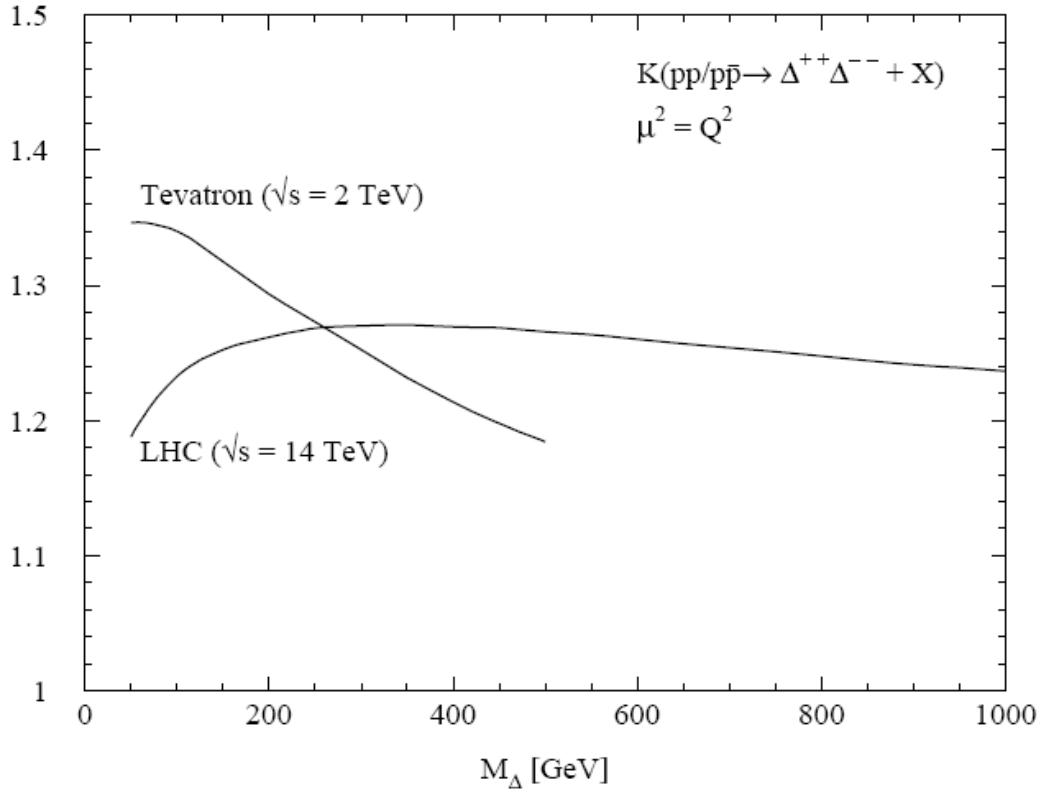
Figure 2.9: K-factors of doubly-charged Higgs pair production at the Tevatron and the LHC as a function of its mass [55].

has excluded $H_L^{\pm\pm}$ below a mass of 136 GeV/c^2 and $H_R^{\pm\pm}$ below a mass of 113 GeV/c^2 [93]. In this analysis we present a search for doubly-charged Higgs bosons in the $\mu\mu$ channel using 1058.12 pb^{-1} of data obtained by the D0 RunIIa experiment.

Chapter 3

Experimental apparatus

The Tevatron is a synchrotron accelerator that collides protons with antiprotons which is located 40 miles west of Chicago at the Fermi National Accelerator Laboratory (FNAL). Collisions occur every 396 nsec at a center of mass energy of s = 1.96 TeV, thus making the Tevatron the highest energy collider in the world until the Large Hadron Collider begins operating at CERN. There are the two interaction regions: D0, where the detector of the same name is located, and B0 where the Collider Detector at Fermilab (CDF) is housed. A brief review of the complex and the D0 detector is presented here.

3.1   The Tevatron Accelerator

Figure 3.1 shows a schematic view of the Fermilab accelerator complex. The proton beam originates as a pulsed 18 KeV negative hydrogen ion beam from a magnetron surface-plasma source. A schematic of a basic magnetron source is shown in Figure 3.2. It consists of a cathode surrounded by an anode with a small gap, typically 1 mm, with a magnetic field passing through the

31
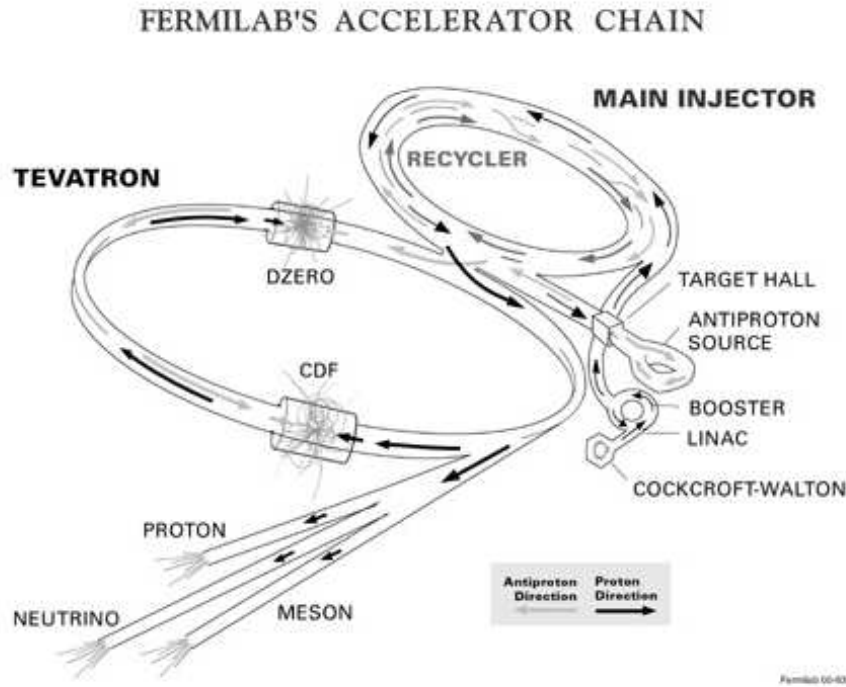
Figure 3.1: The Tevatron accelerator complex

apparatus. Hydrogen gas is added to a pressure of a few hundred millitorr and a dense plasma is produced while electrons are confined to spiral in the anode-cathode gap. Energetic particles strike the cathode and sputter off hydrogen atoms which have been absorbed on the surface. A Cesium vapor coating the cathode surface raises the probability that a hydrogen atom will remove the necessary electrons. After the H^- are formed they are extracted through the anode aperture and accelerated through the extraction plate.

The hydrogen ions are then accelerated through a Cockroft-Walton generator to an energy of 750 KeV and injected into the Linac, a long line of radio
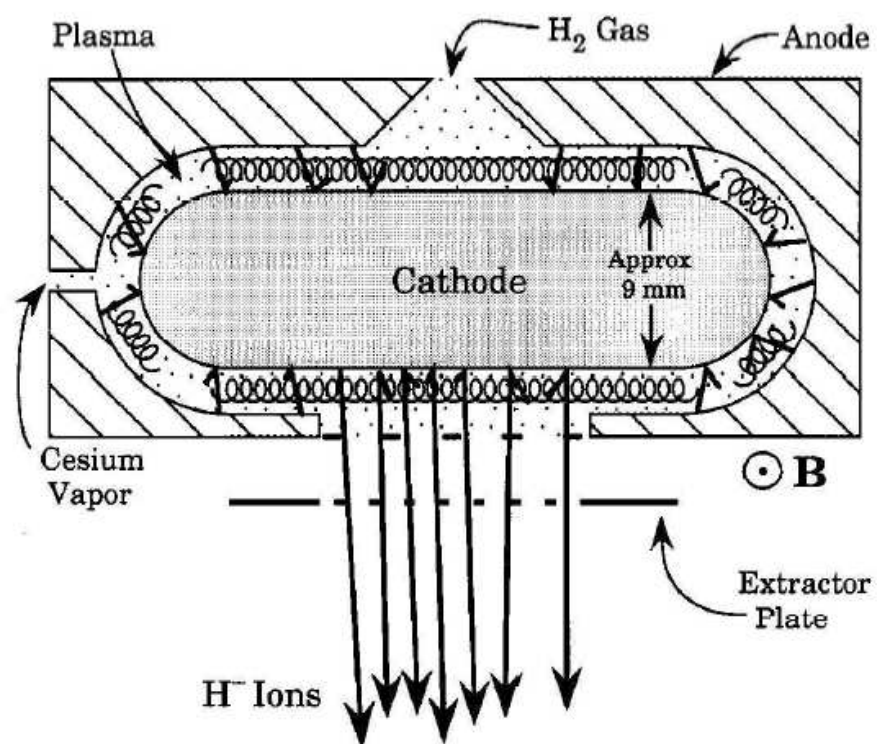
Figure 3.2: A simple magnetron source

frequency (RF) cavities consisting of drift tubes separated by gaps. A particle traveling down the Linac experiences an accelerating field while in the gap between the drift tubes and is shielded from the decelerating field within the drift tube. The hydrogen ions are thus bunched together in the Linac, accelerated to 400 MeV and injected into the Booster, a synchrotron accelerator that accelerates the protons to 8.9 GeV in 33 msec. The Booster uses a charge-exchange injection system in which negative hydrogen ions are brought into a parallel path with protons circulating in a closed orbit in a straight section. The two beams are then merged and passed through a carbon foil which strips the electrons from the H^-'s. The original proton beam is then restored into a closed orbit while unstripped ions are passed to a beam dump.

The proton bunches are then transferred to the Main Injector, a larger synchrotron accelerator that operates in two modes. In the first mode the protons are accelerated to 120 GeV and sent to the $\bar{p}$ production target. In the second mode the protons are accelerated to 150 GeV and are injected into the Tevatron. Antiprotons are created by firing protons onto a nickel target and then focusing the secondaries produced through a lithium lens. These antiprotons are then sent to the Debuncher where their momentum spread is reduced and the transverse profile of the beam is reduced via stochastic cooling. They are then stored in the Accumulator ring until they are needed for a period of collisions, referred to as a "store". The collection of antiprotons in the Accumulator is referred to as the "stack". Because the stacking rate in the Accumulator decreases as the stack size increases, the stack is transferred either to the Main Injector for acceleration or to the Recycler Ring for further storage and cooling. Transfers of stacks to the Recycler enable the Accumulator to stack at a faster rate and thereby increase the number of antiprotons available

for collisons. Antiprotons in the Recycler, referred to as the "stash", are stored until they are needed for a store in which case they are transferred to the Main Injector for further acceleration.

The proton or antiprotons beams are then injected into the Tevatron ring where they are accelerated to 980 MeV and steered by superconducting magnets. Each beam has 36 bunches distributed in three groups of 12 called superbunches. The relative position of the bunches is marked by time periods of 132 ns called ticks, of which there are 159 in the ring. Within a superbunch, the bunch spacing is three ticks (396 ns, which corresponds to about 120 m). The tick and turn structure of the Tevatron beams is shown in Figure 3.3. The p and $\bar{p}$ beams are kept in helical orbits everywhere except the two interaction regions: D0 and CDF. At these two locations, quadrupole magnets squeeze the beams into a cross-sectional area of $\sigma_a \approx 5 \times 10^{-5}$ cm^2 such that the beams collide in the geometrical center of each detector.

3.2   The D0 detector

D0 RunII detector is a large, multipurpose detector for studying $p\bar{p}$ collisions which has been operating at the Fermilab Tevatron since March 2001. The design was optimized for the study of high-p_T physics and high mass states, and stresses the identification and measurement of electrons and muons, the measurement of the direction and total energy of high-p_T jets, and the determination of missing transverse energy. Emphasis is also placed on identifying and tracking individual particles within jets.

Detectors for colliding beam experiments are composed of several different
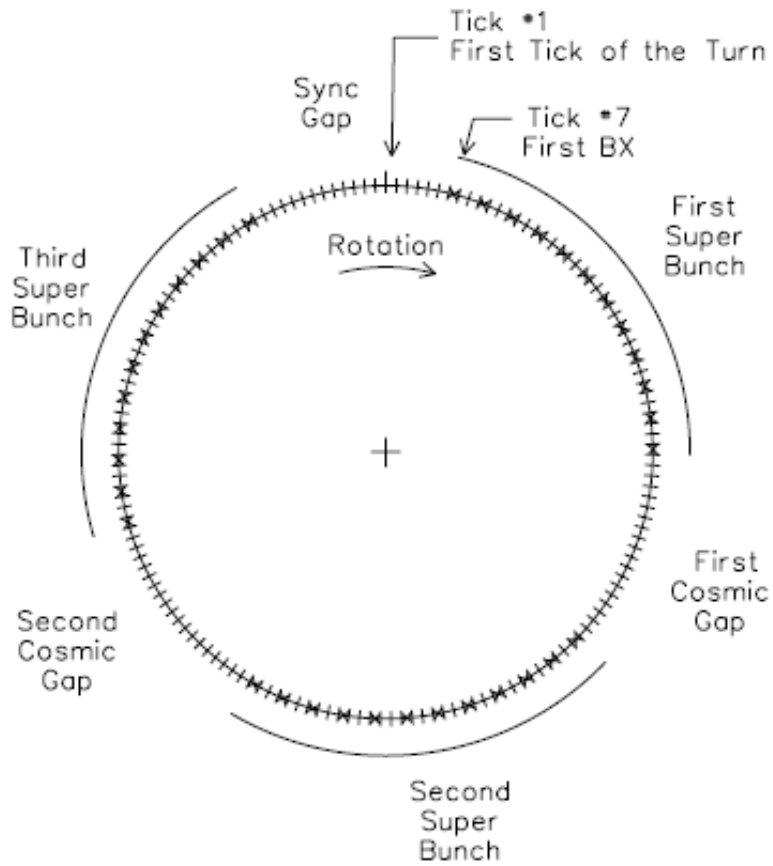
Figure 3.3: The Tevatron beam structure showing 36 bunches distributed in 3 superbunches.

particle-detection devices. They all have their specific strengths and weaknesses. The general layout is optimized however, to achieve optimal efficiency of detecting products of high-energy collisions inside the detector. This is naturally dictated by the physics processes governing the interaction of different particle with the material.

The tracking system is the closest to the interaction point. These devices are designed to measure with a high efficiency and a great accuracy the three dimensional trajectories of particles passing through them. The tracking detectors are immersed in a magnetic field. This permits a determination of the momentum of the charged particle using the curvature (its bending radius) in the magnetic field.

The tracking system is surrounded by the calorimetry. Calorimeters are detectors that measure the energy of a particle that is passing through them. An ideal calorimeter should be so thick that it will absorb all the energy of incident particles. The energy of a particle is measured through the energy deposit in the active material of the calorimeter. This is somewhat inconsistent with the tracking detectors. They should contain as little material as possible in order to minimize effects like multiple scattering and energy loss. Both effects alter the precision with which the calorimeter can estimate energy of an incident particle. Additionally, it complicates reconstruction of particle energies because one has to take into account the energy deposit prior to the calorimeter (that is not read out). A calorimeter is typically made thick enough to stop all known particles except for muons and neutrinos.

Muons are identified by the use of the tracking system outside the calorimeter. Any charged particles that penetrate the calorimeter are likely to be muons. Their momentum is measured using the toroidal field created in the
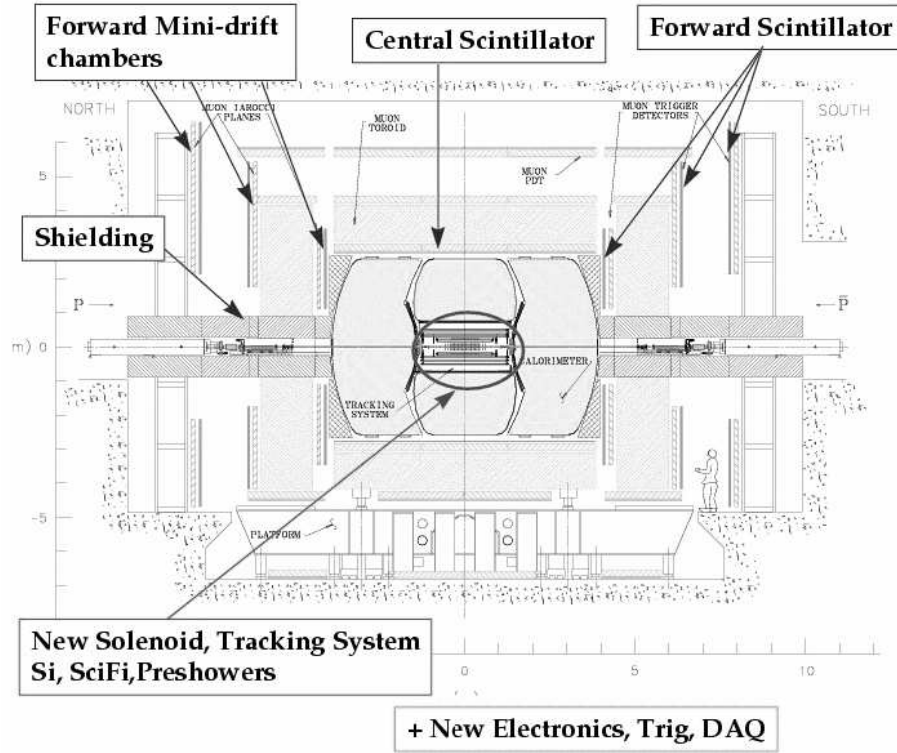
Figure 3.4: Cross sectional view of the Run II D0 detector [55].

muon system. Neutrinos are not detected at all. Their presence is however inferred from an imbalance in the total detected momentum perpendicular to the beam.

The D0 detector is illustrated in Figure 3.4. The D0 detector is about 13 m high × 11 m wide × 17 m long with a total weight of about 5,500 tons. The entire detector assembly rests on rollers so that it can be rolled from the assembly area to the collision hall. The platform provides rack space for detector electronics and other support services.

The electronic noise and grounding is an issue at D0. In order to minimize the electronic noise, most of the clocked devices are kept out of platform. They are moved to the Movable Counting House (MCH), where the analog signals are brought. The MCH contains the digitization electronics, Level 1 trigger, high-voltage power supplies and distribution boxes, etc. The MCH also moves with the detector when rolling in to reduce the length of cables needed to read out the detector. The detector data cables are lead out into the second floor of MCH, into so-called fixed counting house.

The D0 detector was constructed to study high mass and high-p_T phenomena, such as supper-symmetric squarks, gluons and charginos, top physics, the b-sector, properties of the W boson, searches for the Standard Model Higgs boson and beyond. The detector has performed extraordinarily well in Run I. The top discovery and other published physics results are a living reminder of that.

3.2.1   Coordinate System

D0 uses a right-handed coordinate system with the z-axis along the proton direction and the y-axis in the upward direction. The x-axis is therefore in the direction of the center of the Tevatron ring. The angles ϕ and θ are the azimuthal and polar angles, respectively. We use r to denote the perpendicular distance from the z-axis. We define the *pseudorapidity* as,

$$\eta = -\ln\left[\tan\left(\frac{\theta}{2}\right)\right].$$

(3.1)

The pseudorapidity is used to approximate the true rapidity,

$$y = \frac{1}{2} \ln \left(\frac{E + p_z}{E - p_z} \right), \tag{3.2}$$

for finite angles in the limit that $(m/E) \to 0$, which is almost always valid for the relativistic particles arising from interactions at $\sqrt{s} = 1.96$ TeV. We use the term "forward" to describe regions at large $|\eta|$.

3.2.2 Tracking system

The central tracking system consists of the silicon microstrip tracker (SMT) and the central fiber tracker (CFT) surrounded by a 2 T solenoidal magnet. The central tracking system encloses the D0 beryllium beam pipe, which has a wall thickness of 0.508 mm, an outer diameter of 38.1 mm, and is 23.7 m long. Outside of the solenoid is a scintillator-based preshower detector along with other preshower detectors that are mounted on the inner surfaces of the forward calorimeter cryostats. A view of the tracking system is shown in Figure 3.5.

Silicon Microstrip Tracker

The SMT has 792,576 individual strip (6,192 readout chips), with typical pitch of 50–80μm, and a design optimized for tracking and vertexing capability at $|\eta| < 3$. The system has a six-barrel longitudinal structure, each with a set of four layers arranged axially around the beam pipe, and interspersed with 16 radial disks.

The basic philosophy of the D0 silicon tracker is to maintain track and vertex reconstruction over the full η acceptance of D0. This task, however, is complicated by the Tevatron environment. In a machine with a point source
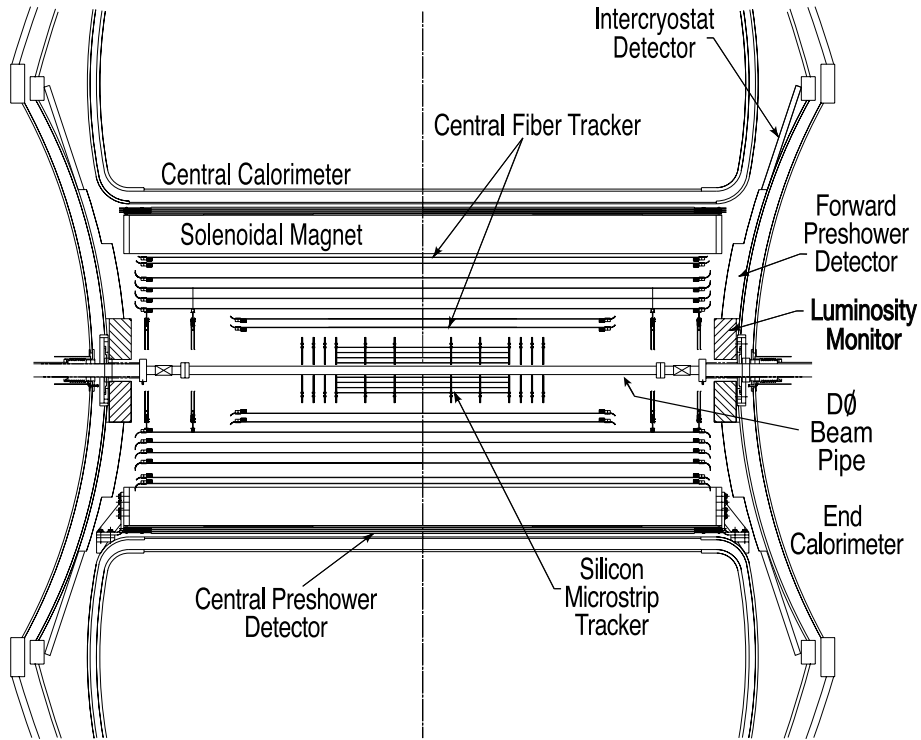
Figure 3.5: Cross sectional view of the D0 tracking system.

luminous region the interaction point could be surrounded by detectors in a roughly spherical geometry. This would allow all tracks to intersect the detector planes at approximately normal incidence and provide optimal resolution.

The design of the SMT is in large part dictated by the long interaction region, $\sigma \approx 25$ cm, which makes it difficult to deploy detectors such that the tracks are generally perpendicular to detector surfaces for all η. This requirement led to a hybrid system, with barrel detectors measuring primarily the $r - \phi$ coordinate and disk detectors which measure $r - z$ as well as $r - \phi$. Thus vertices for high particles are reconstructed in three dimensions by the

disks, and vertices of particles at small values of η are measured in the barrels.

Given all constraints and design considerations, to be discussed in more detail below, the following design was adopted. There are six barrels in the central region. Each barrel has four silicon readout layers, numbered one through four. The four most central barrels employ only double sided silicon. Layers 1 and 3 have axial and 90 stereo readout; layers 2 and 4 have axial and 2002 stereo readout. The outermost two barrels, the barrels at high $|z|$, employ single sided silicon with axial readout only in layers 1 and 3. Layers 2 and 4 have, as in the central four barrels, double sided silicon with axial and 2002 stereo readout. The SMT barrel geometry is shown in Figure 3.7.

Each barrel is capped with a disk of wedge detectors, called the "F-disks". The F-wedges are double sided silicon wafers with trapezoidal shape, with the edges at $\pm 15°$ with respect to the symmetry axis of the wafer. The strips run parallel to one edge, giving an effective stereo angle of $30°$. There are twelve wedges mounted on a disk. To provide further coverage at intermediate $|\eta|$, the central silicon system is completed with a set of three F-disks on each side of the barrel. Each disk is rotated by $7.5°$ with respect to its more central disk.

In the far forward and backward regions two large diameter "H-disks" provide tracking at high $|\eta|$. Each H-wedge consists of two single sided silicon detectors, glued back-to-back. The strips run at $7.5°$ with respect to the symmetry axis of the wafers, giving an effective stereo angle of $15°$. A total of 24 wedges are mounted on one H-disk. Figure 3.6 shows an isometric view of the silicon tracker.

Given the limited radial space available, the four layer silicon detector design was chosen. In this geometry, disks at fixed locations in z provide an additional space point on a track, which give great aid in pattern recognition
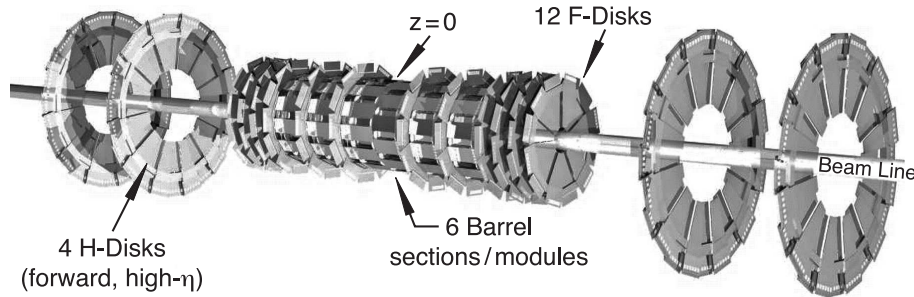
Figure 3.6: Isometric view of the D0 silicon tracker.

and track finding. In such a system the disk separation must be kept small to minimize extrapolation errors. However, each plane of disks also represents a dead region between the barrels which lowers the overall efficiency of the detector. Thus, there is a compromise between vertex resolution at large $|\eta|$ (1/disk spacing) and efficiency at small values of $|\eta|$.

The 12 cm long barrel segments are separated by 8 mm gaps containing F-disks at $|z| = 12.487$ cm, 25.300 cm and 38.113 cm. A set of three more F-disks is located at each end of the central barrel section, at $|z|$=43.113 cm, 48.113 cm and 53.113 cm as shown in Figure 3.8. The disks greatly increase the coverage at high $|\eta|$. Table 3.1 summarizes some of the characteristic of the SMT.

Silicon detectors are $p - n$ junction diodes operated at reverse bias [61]. They are attractive for particle physics because they can be fabricated into small structures leading to very precise position measurements of charged tracks and they have low ionization energy. For example, in silicon one gets an electron-hole pair for every 3.6 eV released by a particle crossing the
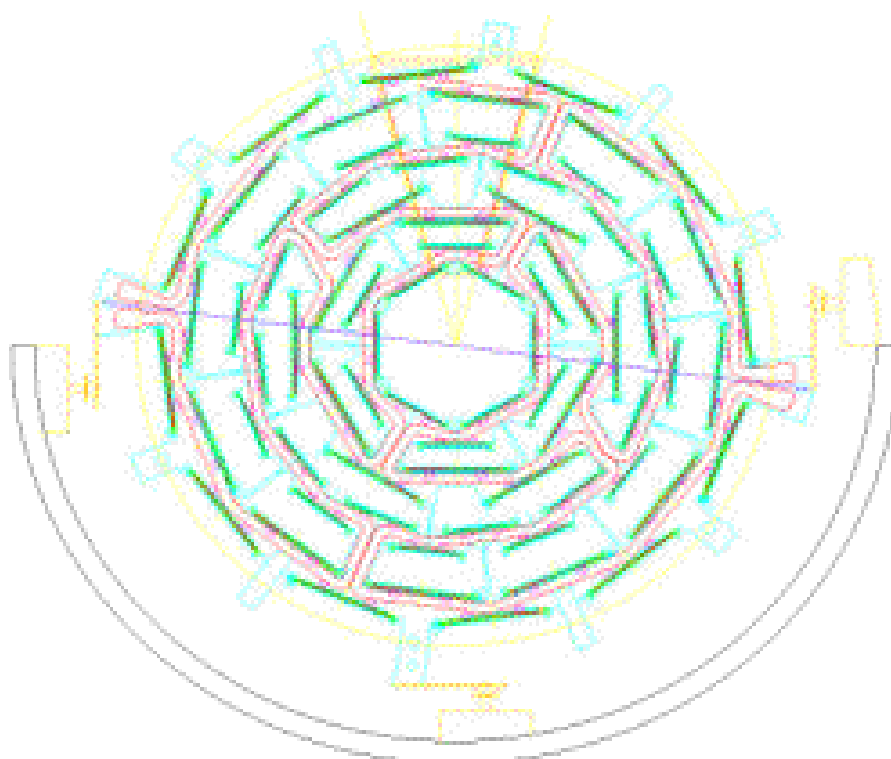
Figure 3.7: SMT barrel geometry
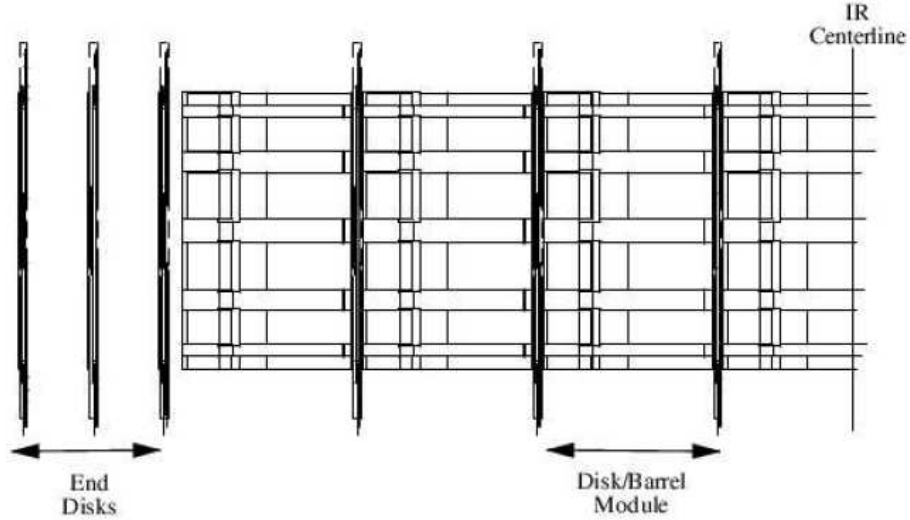
Figure 3.8: Slide view of on half of the central silicon detector.

	Barrels	F-disks	H-disks
Channels	387,072	258,048	147,456
Modules	432	144	96 pairs
Si area	$1.3m^2$	$0.4m^2$	$1.3m^2$
Inner radius	2.7 cm	2.6 cm	9.5 cm
Outer radius	10.5 cm	10.0 cm	26 cm

Table 3.1: SMT numbers (module means ladder or wedge).

medium [62]. This is quite low compared to the 30 eV required to ionize a molecule in a gaseous detector or 300 eV to extract an electron from a plastic scintillator coupled to a photocathode. We now briefly explain the basic principles of the operation of a generic silicon detector. Silicon has four electrons

on its valence shell. p and n materials are obtained by replacing some of the silicon atoms by atoms with five or three valence electrons respectively [62], a process known as doping. Figure 3.9 shows a simple diagram of a silicon-based detector. Finely spaced strips of strongly doped p-type silicon (p^+) are deposited on a lightly doped n-type (n^-) silicon substrate. On the other side, a thin layer of strongly doped n-type (n^+) silicon is deposited. A positive voltage is applied to the n^+ side, depleting the n^- substrate of free electrons and creating an electric field in the n^- substrate. A charged particle that passes through the silicon ionizes and leaves electron and hole pairs. The holes drift to the p^+ strips producing an electric signal. These signals are read by an integrated circuit at the end of the strip thereby enabling the measurement of the position of the particle.

The silicon detectors are read out using the SVXIIe chip [64]. Each chip consists of 128 channels, each including a preamplifier, a 32 cell deep analog pipeline and an 8 bit ADC. These chips are designed to work with double-sided detectors and are mounted on a high density interconnect (HDI). The data passes from the HDI via adaptor cards and interface boards to sequencer boards. Data is sent to the sequencers via optical link fibers. There are a total of 792,576 readout channels in the SMT.

The flexible long tail of the HDI allows the routing of the cable to the outer side of the barrel region. It is through the HDI tail that the control and readout of the SVXIIe chip take place. In addition, the analog and digital chip voltages, as well as high voltage for silicon bias are provided. As an example a double sided $2°$ ladder with 9 readout chips is shown in Figure 3.10.

Figure 3.11 shows a sketch of how the read out of the SMT is set up. The HDIs are connected through 2.5 m long Kapton flex cables to Adaptor Cards
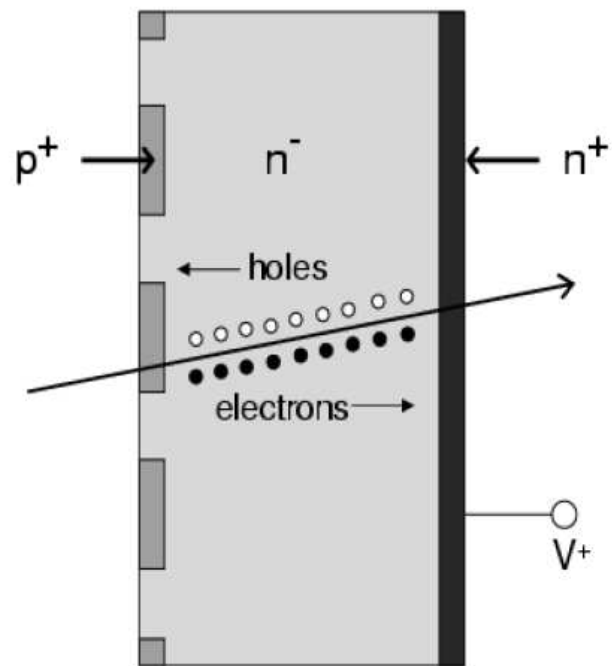
Figure 3.9: A diagram of a generic silicon detector [63].
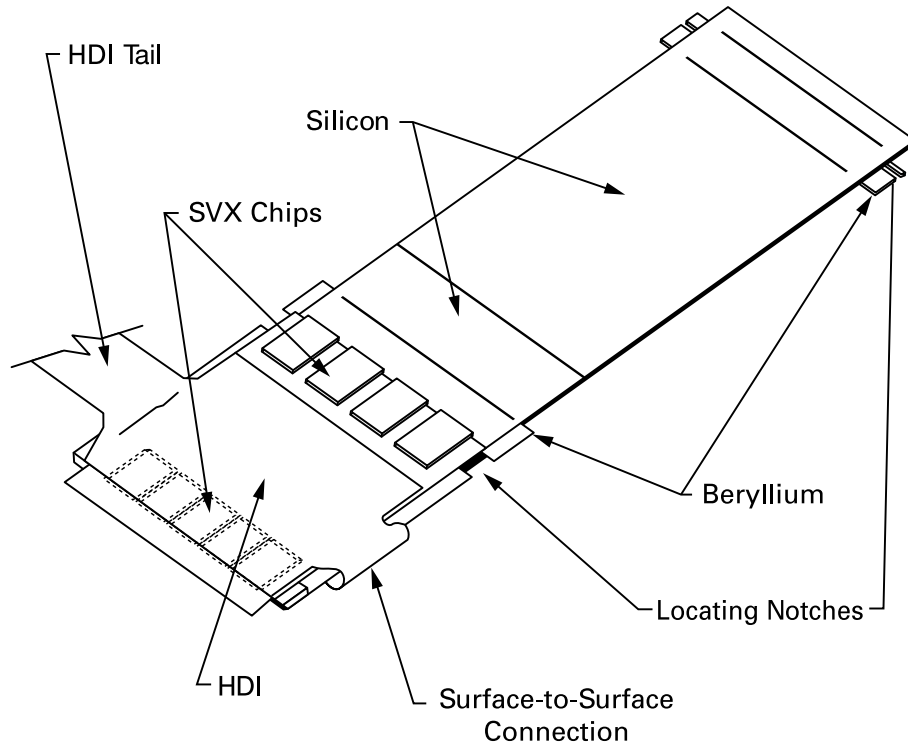
Figure 3.10: A double sided 2° ladder with 9 readout chips.

(ACs) located on the face of the Central Calorimeter. The ACs transfer the signals and power supplies of HDIs to 10 m long high mass cables which connect to Interface Boards (IBs). The IBs supply and monitor power to the SVXIIe chips, distribute bias voltage to the sensors and refresh data and control signals traveling between the HDIs and the Sequencers. The Sequencers control the operation of the chips and convert their data into optical signals carried over 1 Gb/s optical links to VME Readout Buffer (VRB) boards. Data is read out from the chips, transfered in the VRBs through the Sequencers whenever a Level 1 accept is issued and held pending a Level 2 trigger decision.
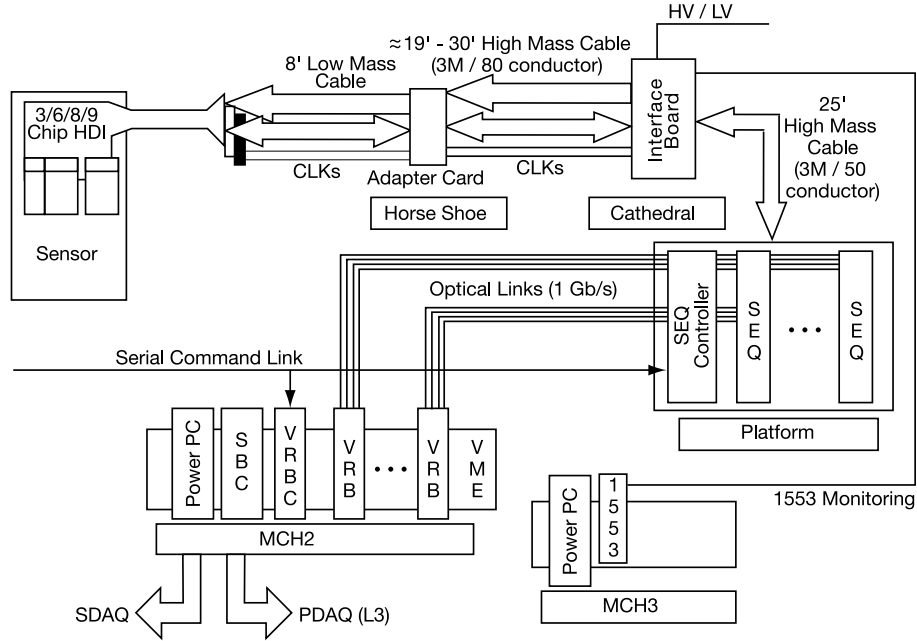
Figure 3.11: SMT read out chain.

The trigger information is received via the SCL (Serial Command Link) by the sequencer crate controller. The SVX sequencer provides timing and control signals for eight chains of SVX chips. These signals are regenerated by interface cards located on the side of the central calorimeter cryostat. The interface cards also control power and bias for the SVX chips, provide interfaces to the monitoring systems, and individual HDI circuit temperature and current trips. Data from the HDI strings are sent from the sequencers to VRB (VME Readout Buffer) located in the moving counting house via optical fibers.

Clock, power, and signal quality and timing are critical to proper operation of the SVXIIe chip. The D0 SMT is read out using low mass kapton flex cables within the detector volume followed by high quality 50 and 80 conductor

"pleated foil" cables on the outside. Both types of cables carry both power and digital signals. Cable runs range from 15–20 meters. A pair of coaxial cables carries the differential clock. The small intermodule gap ($\sim$ 1 mm) is made possible by routing the HDI readout "tail" cables between ladders in the barrel. These are trimmed to length and coupled to a "card edge" style Hirosi connector on the low mass cables. Low mass cables are routed along the half-cylinder and coupled to the 80 conductor pleated foil cables at a ring of adaptor cards located between the calorimeter cryostat (on a so-called "horse shoe").

The details of the design of the silicon tracking detector were mainly driven by requirements with regard to the momentum and vertex resolution, the precision on the r–z measurement and pattern recognition. The first two motivations are discussed below in more detail since they are important for this analysis.

The momentum resolution of the tracker is determined by the strength of the magnetic field, its maximum radius, the accuracy of the measurement of the helix, and the amount of multiple scattering. An overall figure of merit can be defined as the inverse measurement error $(1/\sigma)$ times the field integral $(B \cdot L)$ in the r–ϕ dimension times the lever arm (L), i.e. BL^2/σ. The silicon provides an accurate measurement of the track angle at small radius, but the measurement of the sagitta and outer points in the central rapidity region are performed in the fiber tracker. The silicon serves to anchor the track at the inner radius. The number and detailed location of the silicon layers does not have a major effect on the momentum resolution.

A plot of the momentum resolution as a function of η for a 1 GeV/c p_T track originating at $z = 0$ is shown in Figure 3.12. The solid line shows the resolution for the tracker excluding the H-disks. As $|\eta|$ increases beyond 1.8, tracks begin to miss the last fiber tracker layer and the effective value of BL^2 decreases, rapidly destroying the momentum resolution. Momentum resolution can only be maintained if the detector resolution also improves as $1/L^2$ as $L \to 0$. We have attempted to preserve momentum resolution in the forward direction by adding the large area H-disks, with 10 micron resolution, which cover radii less than 26 cm. These disks do not need to have low mass and can be made at a lower cost compared to the more delicate ladders and F-disks. In the region covered by the H-disks the resolution is comparable to the fiber tracker for radii $r > \sqrt{(0.5\text{m})^2 \times \frac{10\mu\text{m}}{120\mu\text{m}}} = 14$ cm. The effect of the silicon vertex detector on the resolution including the H-disks is shown in the dashed line in Figure 3.12.

Vertex resolution considerations can be understood by considering a simple two layer silicon system with identical resolution at the inner and outer radii, r1 and r2. The impact parameter resolution is given by

$$\sigma = \sigma_{meas} \left(\frac{\sqrt{1 + (r_1/r_2)^2}}{1 - (r_1/r_2)} \right) \tag{3.3}$$

A similar formula holds for disks where r1 and r2 are the radii of the first and last hits on a track passing through several disks. We see that the impact parameter resolution is dependent on the ratio of inner to outer radii of the detector. The cost depends strongly on the outer radius.

Given the above considerations we have decided on a compact system with the inner ladders as close to the beam pipe as is mechanically comfortable and

with an outer radius which is consistent with deploying four layers of detectors. The size of the beam is less than 50μm.

Vertex resolution is also acted by the detector resolution. This is primarily a function of the detector strip pitch, which is constrained by existing interconnect and amplifier technology. Our strip readout pitch is chosen to be 50μm.

Naively the resolution is the pitch/$\sqrt{12}$. In a system where pulse height information is available the resolution is improved by the sharing of charge among two or more readout strips. These charge sharing effects can reduce the resolution from 14μm (i.e. 50μm/$\sqrt{12}$) to 5–10μm, depending on the amount of sharing. The effective strip pitch can also be reduced by intermediate strips at smaller pitch (25μm) which couple capacitively to the instrumented strips.

Disks are used to provide full three dimensional vertex reconstruction. The disk design, with $\pm15°$ stereo double-sided detectors, was chosen after careful analysis of the trade between resolution and mechanical complexity.

Central Fiber Tracker

The Central Fiber Tracker (CFT) consists of scintillating fibers mounted on eight concentric cylinders. The fibers are constructed in ribbons each 128 fibers wide composed of two singlet layers. These singlet layers are formed into the 'doublet' layers which form the ribbon by placing the fiber of one of the singlet layers in the space between the fibers of the other singlet layer. Eight axial layers are aligned along the beam axis. Another eight stereo layers are divided into two groups of four layers: U and V stereo fibers make a $3°$ angle with the beam axis.

Tracking System Pt Resolution (1 GeV/c Pt track)

2D Impact Parameter Resolution
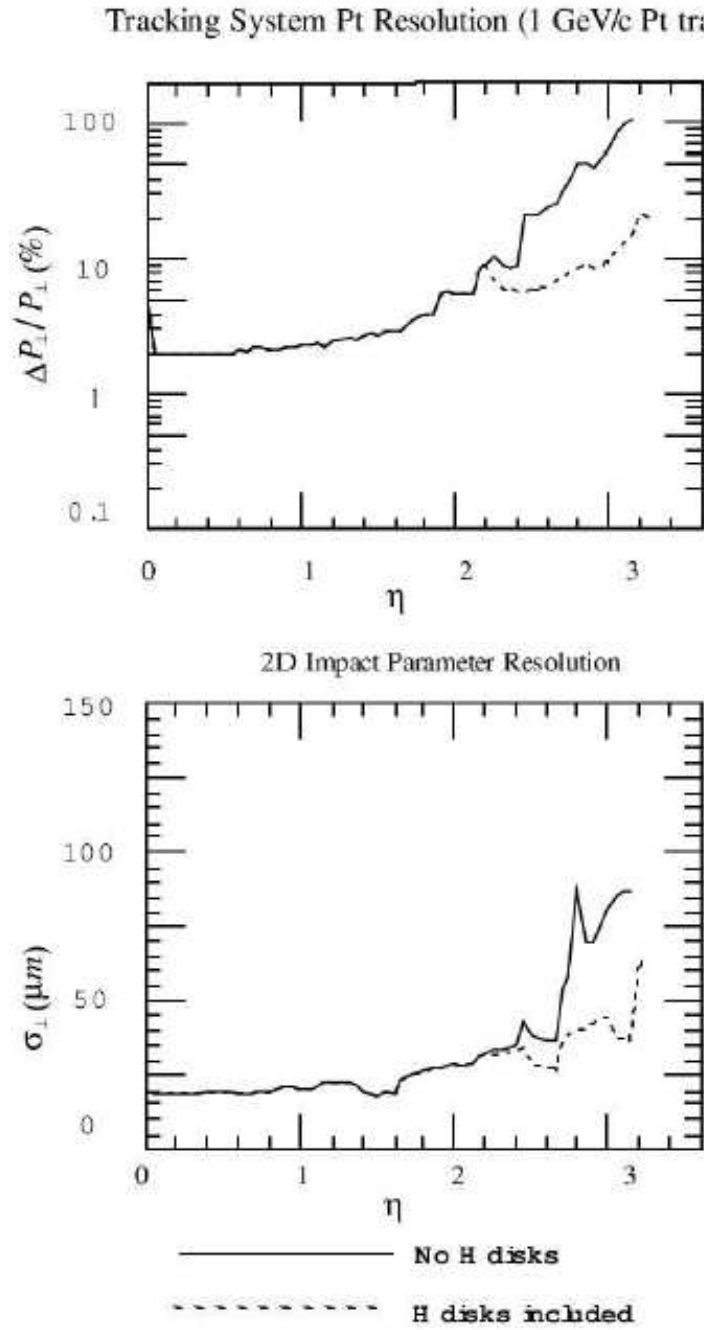
Figure 3.12: Momentum resolution and impact parameter resolution versus pseudo-rapidity.

The light from the fibers is converted into electrical pulses by visible light photon counters (VLPCs). These small silicon devices which have an array of eight photo sensitive areas, each 1 mm in diameter on their surface. They operate at temperatures from 6 to 15 Kelvin, which enables them to achieve a quantum efficiency (Q.E.) value well over 80% and a gain from 20,000 to 50,000 photo electrons.

The detector is divided into 80 sectors in ϕ. Each pie shaped slice have 896 fibers and the entire detector has 71,680 channels. The axial fibers, which are half of all fibers, are used to form a fast Level 1 hardware trigger. All CFT fibers are read out on a Level 1 trigger accept and are used for the Level 2 trigger.

Figure 3.13 shows the design of the Central Fiber Tracker.

The baseline design of the CFT calls for scintillating fibers completely covering eight concentric support cylinders occupying the radial space of 20 to 50 cm. A fiber doublet layer oriented with the fibers in the axial direction is mounted on each of the eight support cylinders. An additional doublet layer oriented in either the u or v stereo angle of approximately 36 is mounted on successive cylinders. The orientation is then: xu-xv-xu-xv-xu-xv-xu-xv. The diameter of scintillating fibers is 835 microns, 775 microns is the active volume diameter. The length of fibers ranges from 166 to 252 cm. Each scintillating fiber is mated, through an optical connector, to a clear fiber waveguide which pipes the scintillation light to a VLPC. The clear fiber waveguides vary in length between approximately 8 to 12 meters.

The details of the central fiber tracker design are given in Table 3.2.

The small fiber diameter, only 835 microns, gives the fiber tracker an inherent doublet layer resolution on the order of 100 microns, which combined
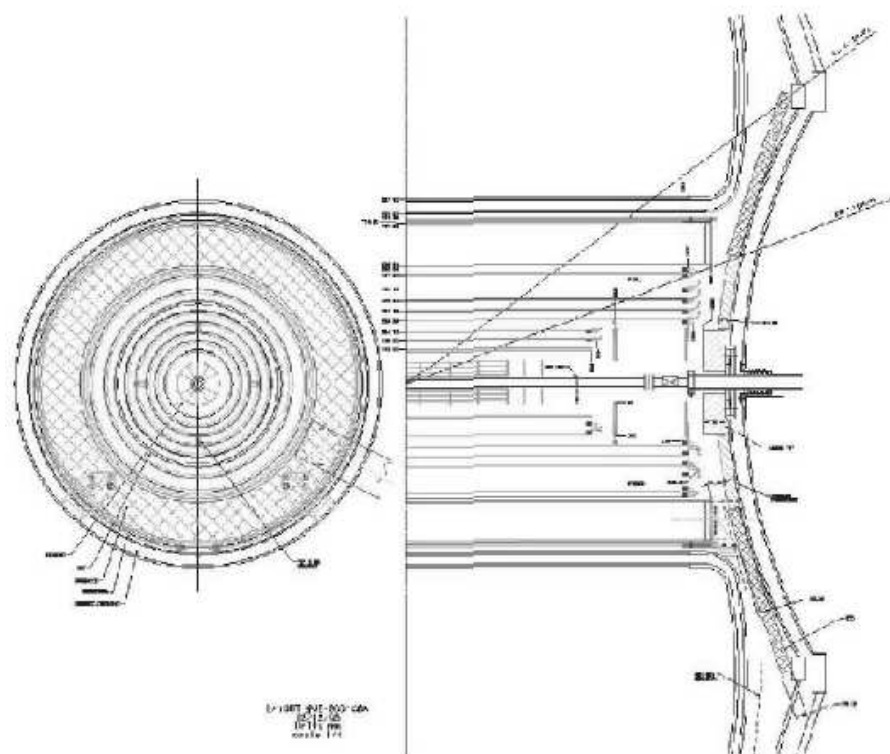
Figure 3.13: Design of the Central Fiber Tracker.

with the silicon tracker in the axial view gives the D0 good momentum resolution for charged particles. In order to preserve this resolution capability, the location of all individual fibers must be known to an accuracy better than 50 microns in the (r, ϕ) plane.

The most important factor for the high-pT tracking is the momentum resolution. It is dominated by multiple scattering of charged particles. To minimize this effect, the material budget of the CFT is kept at its minimum. On the other hand, it is necessary to preserve the rigidity of the system and roundness of the cylinders, to position precisely scintillating fibers.

The small fiber diameter and a large channel count give the tracker sufficient granularity both to find tracks and to trigger in the complex D0 Run II environment. A high doublet layer cluster/hit efficiency is essential to the CFT performance. The mean number of detected photoelectrons per fiber must exceed 2.5 for a minimum ionizing particle. Indeed, this number is a product of of the intrinsic photo yield of the scintillator, the light transmission properties of the fiber and all connectors, and the Q.E. of the VLPC.

Only the fibers themselves are susceptible to any radiation damage. It was indicated in earlier studies that no more than 30% reduction in light yield is expected for the innermost fiber cylinder. Other layers are going to be damaged correspondingly less.

Due to the fiber tracker's fast response time, the total time of the collection of signals from the central fiber tracker from one interaction is considerably shorter than the 396 ns bunch spacing in Run II. This enables the fiber tracker to participate in the D0 Level 1 trigger without contributing any dead time. The trigger is implemented using field programmable gate arrays, FPGA's. First, the signals from singlet axial layers are combined into hits. Coinci-

Layer	Radius (cm)	no. of fibers per sector	no. of fibers per layer	no. of fibers ribbons	fiber pitch (μm)	active length (m)
A	19.99	16	1,280	10.0	979.3	1.66
AU	20.15	16	1,280	10.0	987.2	1.66
B	24.90	20	1,600	12.5	975.8	1.66
BV	25.60	20	1,600	12.5	982.1	1.66
C	29.80	24	1,920	15.0	973.4	2.52
CU	29.97	24	1,920	15.0	978.6	2.52
D	34.71	28	2,240	17.5	971.7	2.52
DV	34.87	28	2,240	17.5	976.2	2.52
E	39.62	32	2,560	20.0	970.4	2.52
EU	39.78	32	2,560	20.0	974.4	2.52
F	44.53	36	2,880	22.5	969.5	2.52
FV	44.69	36	2,880	22.5	972.9	2.52
G	49.43	40	3,200	25.0	968.7	2.52
GU	49.59	40	3,200	25.0	971.8	2.52
H	51.43	44	3,520	27.5	916.1	2.52
HV	51.59	44	3,200	27.5	919.0	2.52

Table 3.2: Design parameters of the Central Fiber Tracker.

dence between eight hits form tracks. The tracks are combined with central
preshower clusters to form an electron trigger, and with muon detectors to
form a muon trigger. However, in order to perform this operation in the 4 μs
time allowed for Level 1 processing, the tracker has to be divided into 80 equal
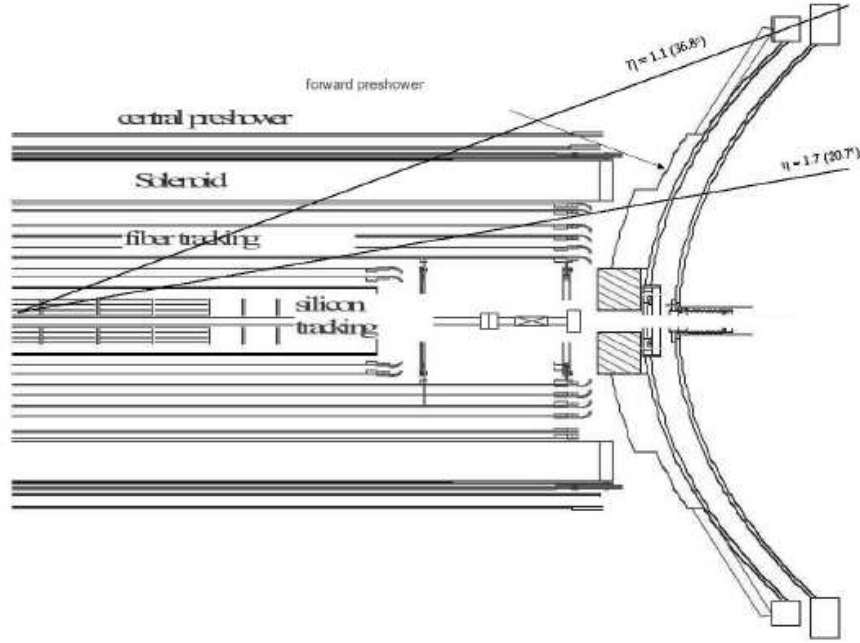
Figure 3.14: Overlap region of the Central Fiber Tracker, $|\eta| > 1.63$.

azimuthal sectors for parallel processing.

As it can be observed in Table 3.2, the first two cylinders are shorter than the remaining six cylinders by about 86 cm, to allow for the CFT support structure. Additionally, the region above $|\eta| > 1.63$ is called CFT overlap. Tracks that originate in the geometrical center of the D0 detector, will cross fewer CFT layers with $|\eta|$ increasing, and as a result, the track fit is going to be worse and worse. The momentum resolution degrades in this region significantly, this can be observed in Figures 3.12 and 3.16. This is particularly important for high-p_T tracks and especially for the curvature q/p_T measure-

ment.

Figure 3.14 shows the overlap region of the Central Fiber Tracker. Tracks crossing the CFT overlap region contribute more frequently to the like-sign muon background through charge mis-identification of one of the muon tracks than tracks measured in the central region of the tracker, i.e. $|\eta| < 1.6$.

The CFT readout electronics are contained on three sets of printed circuit boards which are located at three different places: (a) VRB boards, (b) Port Card Board and (c) Stereo/Trigger Boards. The front end boards digitize the signals and form the trigger tracks. These boards are mounted directly on the VLPC cassettes and come in two varieties, stereo and trigger boards. The Port Card Boards read out the digitized values from the SVX chains and transmit them via fast optical link to the third set of boards, the VME Readout Buffers (VRB). The Port Card Boards are located in the center platform of the detector in the collision hall and the VRBs are located in the moving counting house. Both the Port Card Boards and VRBs are identical to boards used by the silicon tracker electronics. The front end boards receive the analog electrical signals from the VLPC cassettes split them and store one part of the signal in a 32 deep pipeline buffer. On receipt of a Level 1 accept one of the stored events is digitized using the SVXIIe chip and transferred over a fast serial link to the moving counting house where it is available to the DAQ system. On the trigger boards the other part of the analog signal is discriminated using the SIFT-IIb chip and the discriminated outputs are used to form a pre Level 1 axial track list. This list is transmitted to other detector parts for use in Level 1 triggers and is also pipelined for transmission to the Level 2/3 on a Level 1 accept.

The VLPC cassette contains 1,024 channels of VLPC readout and is divided into 8 modules of 128 channels each which are interchangeable and repairable. Figure 3.15 shows the full cassette with readout boards attached. Since the VLPCs operate at cryogenic temperatures, a liquid Helium cryosystem is required. The VLPCs share the Helium refrigerator with the solenoid magnet and the VLPC cassette cryostats operate off separate control dewar. Two cryostats, each accommodating up to 51 VLPC cassettes, house the entire VLPC system. Two cryogens are used in the system. Liquid Helium from the control dewar allows for VLPC operation at about 6 K and liquid Nitrogen cools an intermediate heat intercept in the VLPC cassette in order to reduce the heat load to the liquid Helium. The cassette cold end sits in a stagnant gaseous Helium volume. Conduction through the gas cools the VLPCs.

Each VLPC cassette holds two front end boards which are slightly different versions of the same board. The board mounted on the right side of the cassette when viewed from the front is called the Right Hand Board (RHB) and the one on the left the Left Hand Board (LHB). Each front end board supports 512 channels of signal from the cassette. The RHB interfaces to the cryogenic power and control systems for each cassette. Each front end board interfaces to the bias voltage supply and return for the VLPCs.

The CFT is divided into eighty equal wedges in azimuth known as sectors. The channels from each sector are input into two front end boards. The channels from the stereo fibers are input into the stereo boards. The channels from the axial fibers are input into the trigger boards which also contain the logic which forms the Level 1 axial trigger tracks. While each board supports 512 input channels the CFT does not use them all, the Central Preshower detector (CPS) uses the rest.

In the analog signal line from VLPC, after the coupling capacitor, is placed the SIFT chips. It was developed for a fast logical output needed for Level 1 trigger. Each SIFT chip has 16 input channels and a common threshold. The chip first amplifies the signal and then buffers it. It outputs a 3.3 V single ended output for those channels above threshold. The SIFT chip outputs an analog signal to the SVXIIe for digitization. The SVXIIe chip functionality is described in [65]. It was designed for the silicon tracker readout but is well suited to the fiber tracker readout as well. The signal amplitude and shape as well as the effective detector capacitance out of the VLPC or SIFT within range of the SVXIIe chip. Detailed information on the silicon tracker read out system can be found in several places [66, 91] and does not have to be repeated here.

The expected transverse momentum resolution for the D0 tracking system is shown in Figure 3.16.

The calculation was performed with the following parameters: (a) the resolution of the scintillating fiber doublet is 100 microns, (b) the resolution of the silicon barrels is 10 microns, (c) the thickness of the barrels supporting the scintillating fibers is $0.086g/cm^2$ for barrels 3 and 4 and $0.065g/cm^2$ for all other barrels, (d) the radial distribution of the non-active material in the silicon detectors is taken into account, (e) and the interaction vertex is known with a precision of 35 microns.

The transverse momentum resolution at pseudorapidity $|\eta| = 0$ is parametrized as

$$\frac{\sigma_{p_T}}{p_T} = \sqrt{0.015^2 + (0.0014 \cdot p_T)^2} \tag{3.4}$$
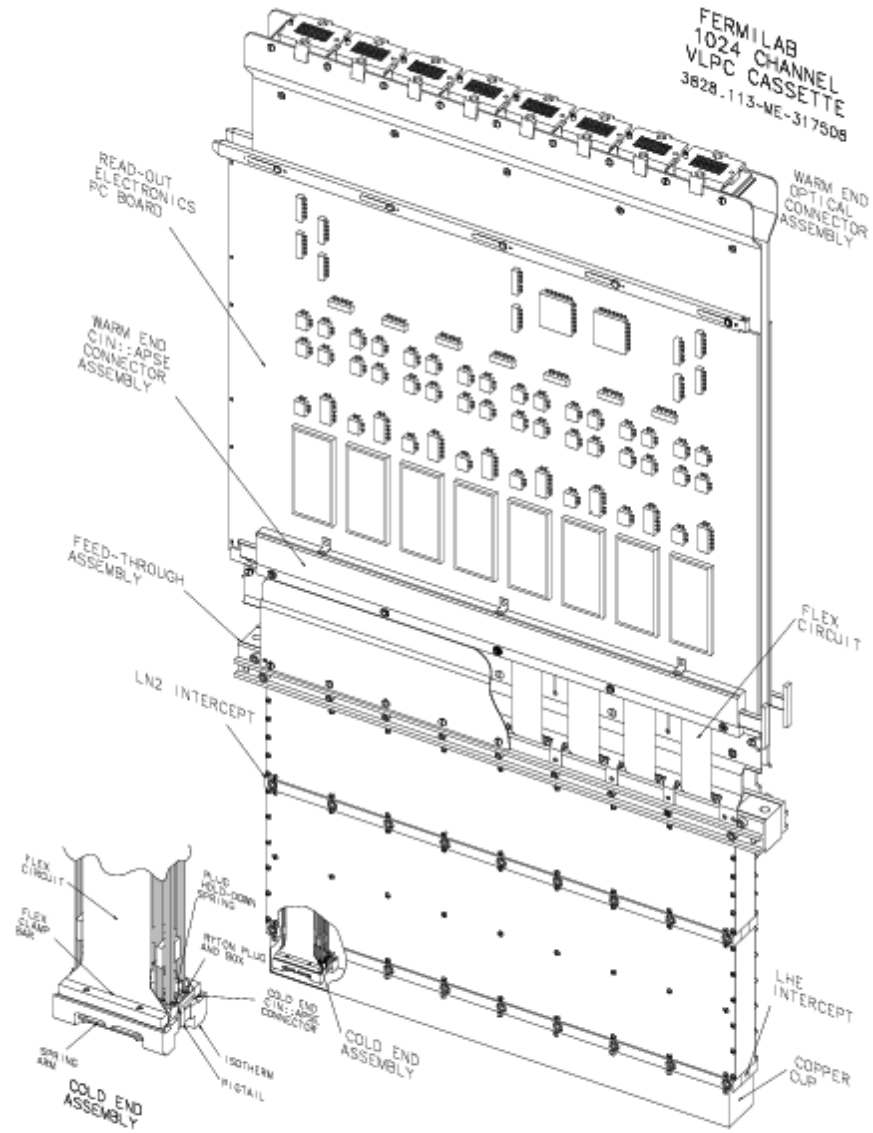
Figure 3.15: The VLPC cassette with readout electronics board attached.
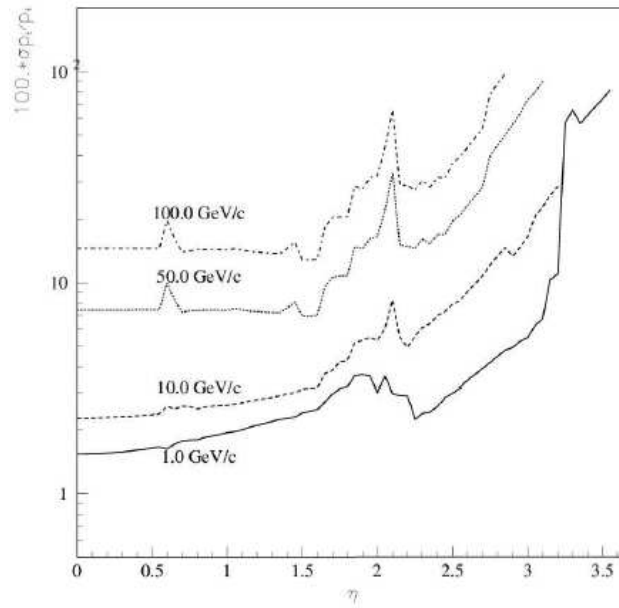
Figure 3.16: Momentum resolution as a function of pseudo-rapidity, assuming 35 micron primary vertex resolution.

Preshower Detectors

Central and forward preshower detectors located just outside of the superconducting coil (in front of the calorimetry) are constructed of several layers of extruded triangular scintillator strips that are read out using wavelengthshifting fibers and VLPCs.

3.2.3   Calorimetry

Calorimeters are used to determine the energies of particles, both charged as well as neutral, by total absorption in the calorimeter medium. In fact, the

calorimeter is a block of matter which intercepts the primary particles and due to its size causes them to interact and deposit all their energy inside the calorimeter volume. The deposited energy is transformed into the subsequent cascade of secondary particles, a so called shower. Such a cascade of secondary particles is a flow of low-energy particles. Most of the incident energy is unfortunately dissipated and appears in the form of heat. A rather small fraction of the deposited energy is detectable in the form of a signal.

Calorimeters or many attractive capabilities:

- they are sensitive to charged and neutral particles.

- the energy degradation through the shower development is a statistical process. The average number of secondary particles $< N >$ is therefore proportional to the energy of an incident particle. This significant property causes that the uncertainty in the energy measurement is governed by statistical fluctuations of N and hence the energy resolution σ/E improves as $1/\sqrt{N} \sim 1/\sqrt{E}$.

- the required length of the calorimeter for total absorption increases logarithmically with particle energy E.

- thanks to the detector segmentation, the shower development allows a precise measurement

- different response to electron and hadrons can be used for particle identification

- their fast response allows them to operate with fast trigger techniques and rapid online event selection.

Calorimeters can be logically split into two groups in view of their different purposes

- electromagnetic calorimeters:

  They are designed to measure the energy of photons and electrons. Photons interact predominantly via pair production in the vicinity of a nucleus. Electrons loose their energy mainly through Bremsstrahlung which is an interaction with a Coulomb field of an atom. Photons of high energies are produced in Bremsstrahlung. Indeed, daughter particles, again photons, electrons and positrons, might undergo interactions themselves. An electromagnetic shower is started that way. It develops until the energy of particles lowers to the level of critical energy (energy at which the showering process stops). Figure 3.17 depicts the development of such a shower.

- hadronic calorimeters:

  Their purpose is to measure energy of the hadronic shower, to identify jets, estimated missing transverse energy E_T^{miss} and perform measurement of low-energy muons.

  The jets are the natural objects at hadron-collider experiments because of the high c.m.s. energy. The individual particles can be hardly seen in the calorimeter. Only the energy flows might be measured in some angular *tower* of the calorimeter. Quantum Chromodynamics can reliably calculate only the energy flow of partons in a definite angular cone. This is not the disadvantage however. Quarks and gluons coming from the reaction convert into observable hadrons after the collision. This process is called hadronization and it is not possible to describe it in detail
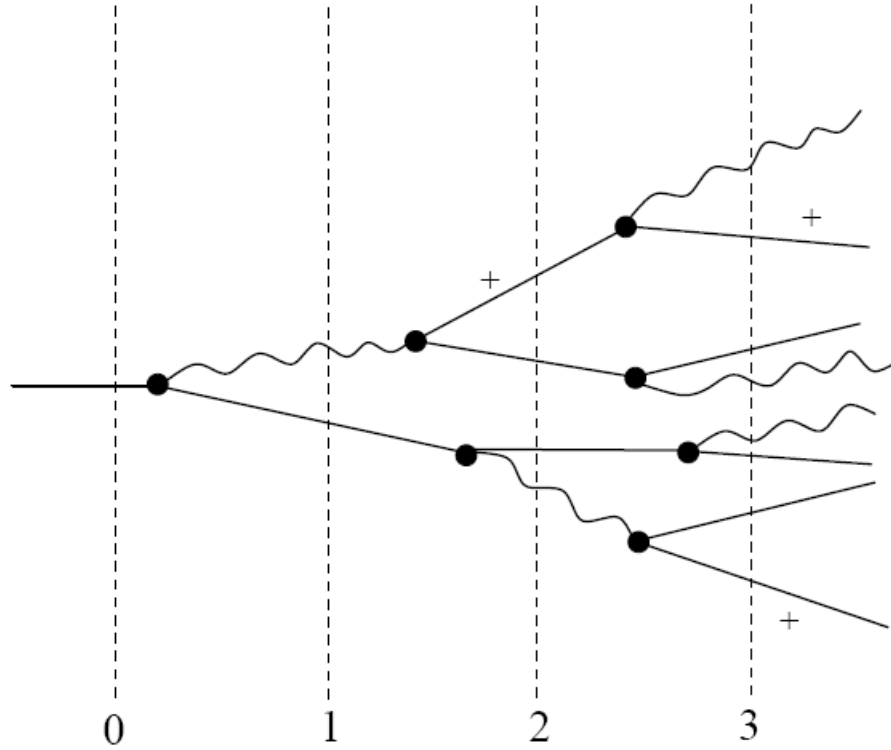
Figure 3.17: Diagram of the development of an electromagnetic shower in a calorimeter. Solid lines (with +) indicate electrons (positrons) and wavy lines indicate photons. The numbers at the bottom show the distance measured in radiation lengths with the absorber beginning at 0.

theoretically. There are several models which are invented to describe these collisions. Their fundamental assumption is that the energy flow calculated on the level of partons is almost equal to the energy flow of measured hadrons. This significant property gives *jets* physical sense. Jets are angularly collimated streams of hadrons which are interpreted as "traces" of original quarks or gluons. The jet energy is estimated by measuring the energy deposited in a cone of opening angle ΔR around the jet axis (average direction):

$$\Delta R = \sqrt{\Delta^2 \eta + \Delta^2 \phi} \tag{3.5}$$

This equation makes the backbone of the "jet finding algorithm". There are also several intrinsic limitations for jet calorimetry (especially for missing E_T^{miss} and jet energy measurement), such as fragmentation effects (they depend on the nature of jets), magnetic field sweeping of charged particles (the opening of the cone and low momentum fragments), gluon radiation and energy losses to non-interacting particles, such as neutrinos or even muons (they are minimum-ionizing particles).

Due to the high luminosity, a special attention must be paid to the pileup energy from minimum-bias events which also becomes important. Minimum-bias events are soft-scattering events which are superimposed during the same crossing and which are dependent on the luminosity. There are on average 0.7 minimum bias events at current luminosity $(10^{32} \mathrm{cm}^{-2}\mathrm{s}^{-1})$.

The development of hadronic showers in matter is very complicated, this is why an analytical treatment is unfortunately not available.

Hadron production is sensitive to the energy carried by the incident particle and to the type of a projectile. In average the multiplicity increases very slowly with the mass number of the target material. About half of the energy is carried by leading particles. One third of the pions, that are produced by the collision in the calorimeter medium, are the neutral pions. Their energy is dissipated in the form of electromagnetic showers because of their electromagnetic decay into two gammas. They will therefore propagate without further nuclear interactions. The average fraction is [75].

$$\langle f_{\pi^0} \rangle = 0.11 \cdot \ln E[\text{GeV/c}^2] \tag{3.6}$$

in the energy range of several hundred GeV/c^2. The size of the π^0 component is determined by the production in the first interaction.

A fraction of the total energy is dissipated in ionizations by electrons and charged hadrons. This energy fluctuates from event to event. Therefore this is the most important and the largest contribution to the energy resolution. Another problem is that the largest fraction of energy is not seen. The energy which is going either in breaking nuclei (binding energy) or in low energy neutrons is invisible.

Many of the low energy particles (gammas, protons of few MeV) which are produced in deexcitations of nuclei are badly sampled because of saturation effects in the active matter. A large fraction of the nuclear excitation goes into fast protons and neutrons. Finally, muons and neutrinos emitted in the decay of pions escape from the calorimeter. These muons and neutrinos are direct products of the charged pion decay. As it

has pointed out earlier, neutrinos will remain undetected. They will not leave any trace in the detector. Muons however, are minimum ionizing particles, which means that muons are particles that find themselves in the minimum of the ionization loss curve $\frac{1}{\rho}\frac{dE}{dx}$, and hence their energy losses are about 2 MeV/g·cm^{-2} and they are nearly independent of muon transverse momentum. This is why an average muon energy loss in the D0 calorimeter can be approximated by about 2.3 GeV/c^2.

There are two important interaction phases during the hadronic shower development [75]:

– *High-energy cascade phase*:

Secondary particles are produced due to high energy of incident hadrons which are taking part in the interactions with the nucleus of the active material. Most of the secondary particles are naturally pions. Protons, neutrons, heavy fragments and other heavy particles can be also produced if the incident energy is big enough to fulfill the kinematical conditions allowing their production. The secondary particles have rather high energies after their creation and hence they can later interact too.

– *Nuclear deexcitation phase*:

The excited nucleus decreases its energy by emission of slow neutrons and by γ-transitions. The energy spent breaking up nuclei will not be visible. This is quantified by the e/π ratio, i.e. ratio of the calorimeter responses to electrons and pions. Uranium is used to correct this ratio, its nuclei can be easily broken up by slow neutrons, which will in result, produce particles that can be detected

and this additional energy will compensate for energy losses due to slow neutrons and γ-transitions.

The nuclear deexcitation and pion, muon decays will act the shower composition, which has a very different response. The hadronic shower has a characteristic longitudinal and transverse profile. The longitudinal distribution is scaled in units of absorption length λ_{abs}, which has the meaning of the mean distance between two inelastic collisions of hadrons with nuclei [76, 77]. The transverse distribution depends on the longitudinal depth. The core of a shower is rather narrow, it is increasing with the shower depth. The collimated core, which consists of high-energy particles, is surrounded by lower-energy particles. The main part of them extends away from the shower axis, the 95 % containment is required in a cylinder of radius $R \sim 1\lambda_{abs}$ [78].

There are many approaches in calorimeter construction. In principal, two are the most distinct ones: homogeneous calorimeters where the absorber is also an active material (lead glass, NaI or BGO), or the sampling calorimeters. This approach interleaves layers of a dense, inert absorber with layers of a material which is sensitive to particles passing through it, such as liquid Argon, scintillators, etc. Most of the energy is deposited in the passive material and only a small fraction of the incident energy is read out from the active medium.

Calorimeter geometry

The D0 calorimeter is a sampling calorimeter. The depleted uranium, with copper and stainless steel in the outer regions, is used as a primary absorber.

The liquid argon (LAr) is used as the ionization medium. The electron recombination is very low for inert gases, this is why the signal to noise ratio is going to be rather high. The calorimeter is rather compact because of the high density of uranium.

The calorimeter is divided into a large number of modules. Each of them consists of a stack of interleaved absorber plates and signal boards. A schematic view of one calorimeter cell is shown in Figure 3.18. The absorber plates are separated from signal boards by liquid argon gap of 2.3 mm. The signal board consists of a copper pad sandwiched between two 0.5 mm thick pieces of G10. The outer surfaces of these boards are coated with a resistive epoxy coating. The absorber plates are grounded. The positive voltage of 2.0–2.5 kV is applied to the resistive coatings. Charged particles from e.m. or hadronic shower cross the LAr gap and leave a trail of ionization. The ionization electrons drift towards the signal board where they are collected. The drift time is approximately 450 ns. They induce a signal on the copper pad via capacitive coupling. The readout pads are subdivided into smaller cells so that the transverse position of showers can be measured. The corresponding cells in adjacent signal boards are ganged together in depth to form readout cells.

Figure 3.19 shows the D0 calorimeter design. The calorimeter is placed in the cryostat because of the liquid argon used as a sensitive medium. The calorimeter is divided into three major assemblies, each sits in its own cryostat. This way is secured access to the tracking system. There is a central calorimeter (CC) and two end-cap calorimeters (EC). The central calorimeter provides coverage up to pseudorapidity of about 1.2. It is roughly toroidal, and it consists of three concentric layers of modules. The inner layer has 32 electro-magnetic (EM) modules. They are thick enough to contain most e.m.
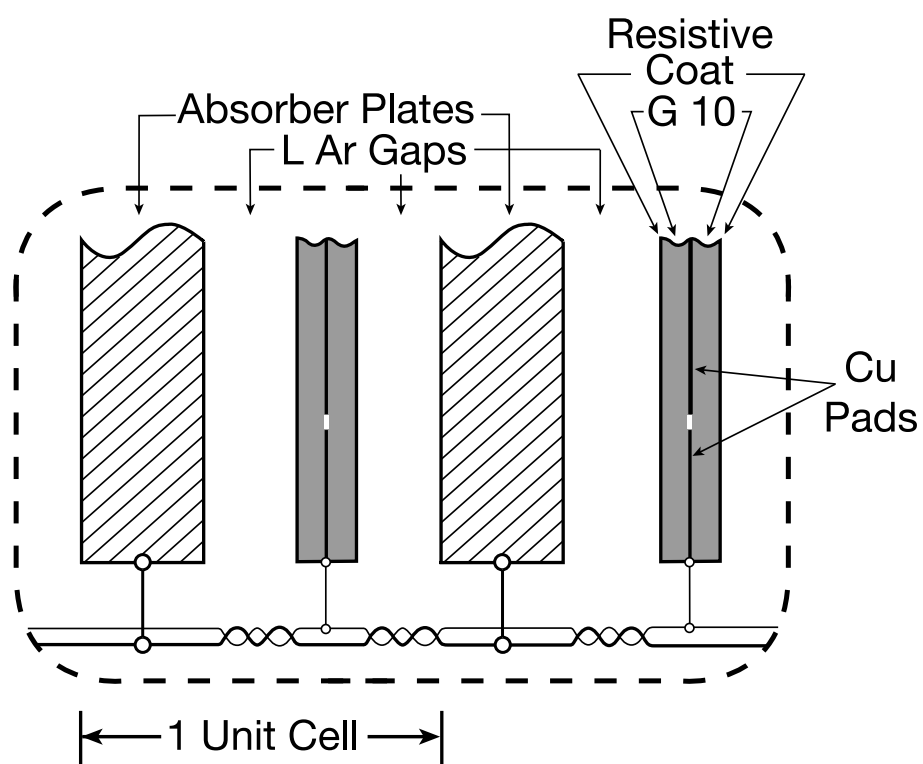
Figure 3.18: A schematic view of a calorimeter cell.
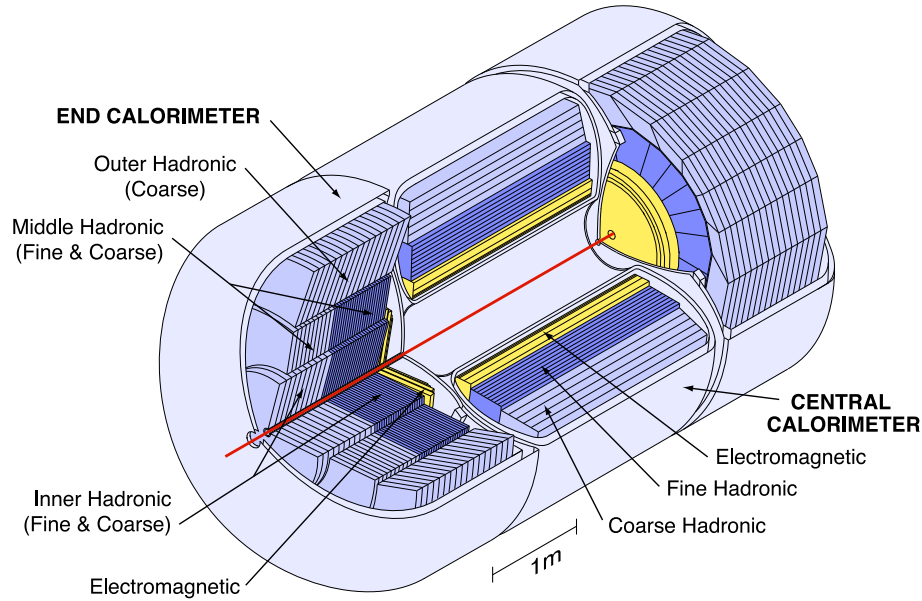
Figure 3.19: The D0 calorimeter [79].

showers. It is approximately 20.5 radiation length, where one radiation length is a distance on which energy of a particle degrades down to $1/e$ of the incident energy in a given medium. The middle layer consists of 16 fine hadronic (FH) modules, which measure showers due to hadronic particles (96 radiation lengths). The final layer consists of 16 coarse hadronic (CH) modules, which measure any leakage of energy out of the back of the calorimeter into the muon system, so called punch through. The parameters of the CC modules are given in [58, 79].

The two end-caps provide additional coverage on each side of the CC from a pseudorapidity of about 1.3 out to about 4. End-caps are composed of three concentric layers of modules, they are divided into e.m., fine and coarse hadronic types. The center of the EC consists of a disk-shaped e.m. module,
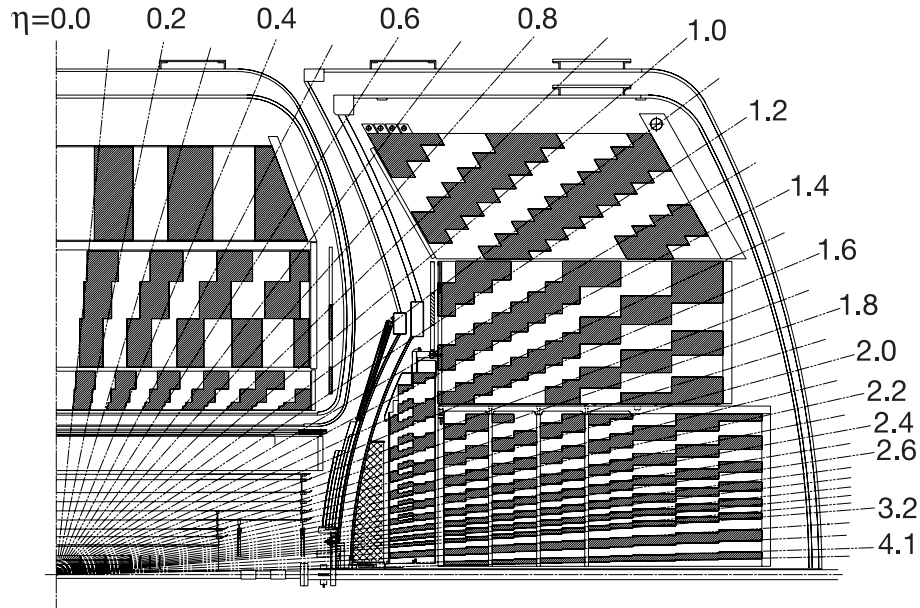
Figure 3.20: Side view of the calorimeters [79].

back to it, there are cylindrical fine and coarse inner hadronic modules. The fine and coarse middle hadronic modules are arranged in a ring around the central core. Finally, the last ring is built out of coarse outer hadronic modules.

The area in (η, ϕ) plane is covered by readout cell of size 0.1×0.1. In the third layer of EM modules, where a shower deposits most of its energy, cells have areas of 0.05×0.05. In addition, cells with $|\eta| > 3.2$ have a ϕ size of 0.2 and are somewhat larger in η as well. The calorimeter segmentation is shown in Figure 3.20.

In a transition region between CC and EC ($0.8 < |\eta| < 1.4$), there is a relatively large amount of uninstrumented material. This space is left out be-

cause of cryostat walls and the support structures for the calorimeter modules. There are two devices used in this region: (a) massless gaps (MG) and (b) the intercryostat detector (ICD). The MG are rings of two signal boards mounted on the end plates of the CCFH, ECMH and ECOH modules. The ICD is a ring of scintillation counters mounted on the exterior of the EC cryostats. Both devices have a segmentation of 0.1×0.1.

Calorimeter readout

The signals induced on the readout pads are pulses with widths of the order of 450 ns [79]. Signals are led out through four ports in the cryostats to charge sensitive preamplifiers mounted on top of the cryostats. The signal is then passed to the base line subtractor (BLS) boards located on the platform below the detector. The BLS modules perform analog shaping and split the signal into two paths. One is used for trigger purposes. Signals from all EM and fine hadronic cells within a 0.2×0.2 tower are summed. These signals form the input to the Level 1 calorimeter trigger.

The other path is used for the data readout. The incoming signal is sampled just before the beam crossing and again about 300 ns later. The difference between these two samples is a DC voltage which is proportional to the collected charge. The difference is then sent to the ADCs where, if the event is accepted by the Level 1 trigger, the signals are digitized and sent to the Level 2 trigger.
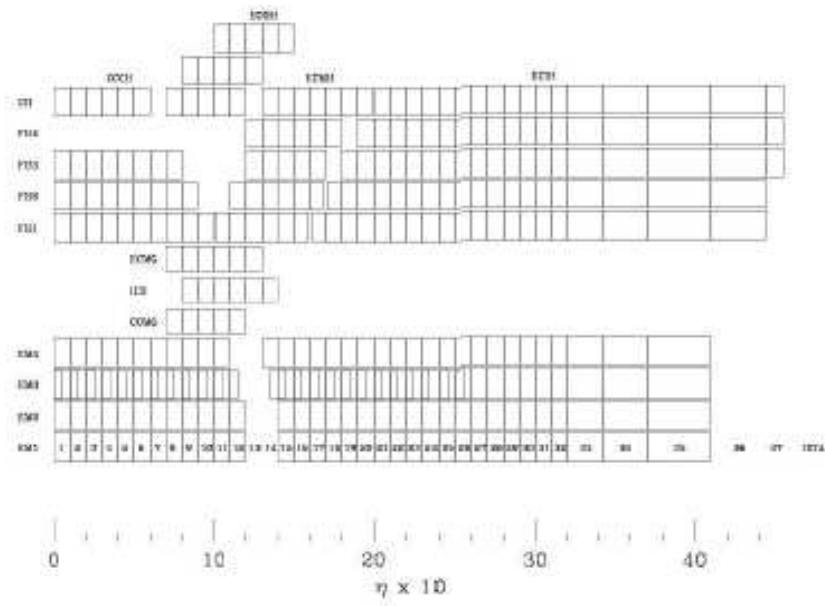
Figure 3.21: Layout of calorimeter channels in depth and $|\eta|$.

3.2.4   Muon system

The Run II D0 muon system [80] will enable D0 to trigger, identify and measure muons in the new high rate environment [81]. The luminosity in Run II has increased up to $2 \times 10^{-32} \text{cm}^2\text{s}^{-1}$ and the beam spacing changes from 2.5 μs to 396 ns. This change indeed requires a corresponding upgrade of the D0 detector [82, 83]. The central muon system has been supplemented with additional scintillator layers for triggering, cosmic ray rejection, and low momentum muon measurements. New shielding has been added to decrease background rates. The muon trigger has been redone to accommodate the high trigger rate and increased number of interactions per beam crossing. The upgraded central tracking system consisting of the Central Fiber Tracker and the Silicon Microstrip Tracker improves the momentum measurements of muons as well as other charged particles.

The D0 Run II muon detector is composed of three main components: scintillators for triggering and cosmic rejection, a toroidal magnet to allow for an independent muon momentum measurement, and drift tubes to measure hit positions. The forward muon tracking system, new for Run II, uses planes of mini-drift tubes and extends muon detection to $|\eta| = 2.0$. Scintillation counters are used for triggering and for cosmic muon and accelerator backgrounds rejection. Toroidal magnets and special shielding complete the muon system. All subsystems interact with three levels of triggers. Level 1 generates trigger information synchronously with the beam crossing, Level 2 operates asynchronously with a maximum decision time of 0.1 ms. All three muon detector subsystems use a common readout system based on a 16-bit fixed point digital signal processor, which buffers the data from the front-end, re-formats the data if accepted by Level 2 and sends it to the Level 3 trigger system,
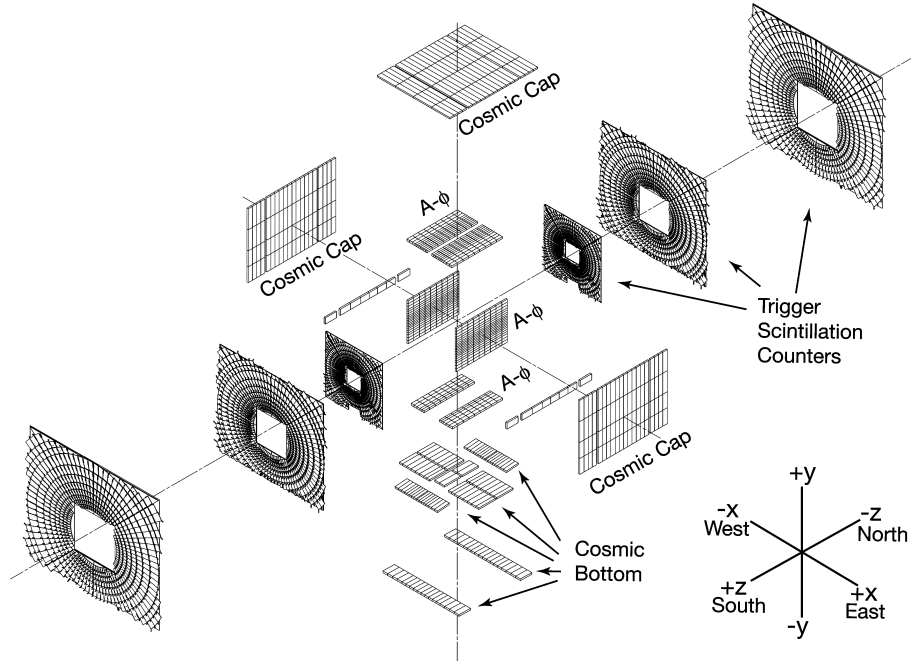
Figure 3.22: Exploded view of the muon scintillation detectors..

which is a farm of Linux workstations running software trigger filters. Muon triggers accepted by Level 3 are written to tape for offline reconstruction.

Geographically, the muon system can be divided between Central Muon Detectors and Forward Muon System. Figure 3.22 and Figure 3.23 show the layout of the muons system scintillators and drift tubes in both the central and forward regions.

Central Muon Detectors

The central muon tracking system, with pseudorapidity coverage $|\eta| \leq 1.0$, consists of 94 proportional drift tube chambers built for Run I [84]. The A
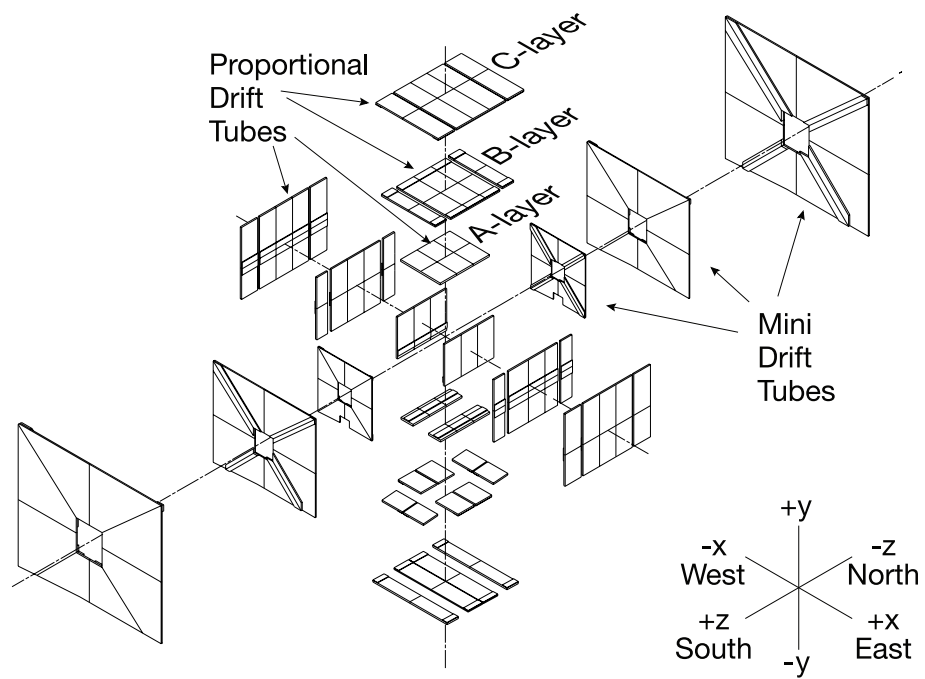
Figure 3.23: Exploded view of the muon wire chambers.

layer is between the calorimeter cryostat and the 2 T muon toroid magnet. The A layer chambers on the top and sides have 4 decks to help in rejecting backgrounds, while those on the bottom only have 3 decks due to space constraints. The B and C layers outside the toroid have three decks each. The chambers are rectangular aluminum tubes with 5.7 cm by 10 cm cells. The drift distance resolution is about 1 mm. The momentum resolution from the PDTs is about 30% for muons with pT = 100 GeV/c, where p_T is the momentum transverse to the beam direction. But when the muon track is matched with tracks from the D0 central tracking system, the resolution is improved for all central muons. For muons with $p_T = 100$ GeV/c, the resolution using central tracking is about 15%.

Layers of scintillator, called the Cosmic Cap, on the top and upper sides of the central muon detector were used in Run I to help reject cosmic rays. Coverage was completed for Run II when Cosmic Bottom counters were added. There are 240 counters in the cap and 132 in the bottom. A new layer of scintillators, called the Aϕ counters, was added between the A layer and the calorimeter [85]. These counters have ϕ segmentation of 4.5 degrees. The Aϕ counters are used for muon triggering, rejection of out-of-time scattered particles and identifying low-p_T muons.

Forward Muon System

The Forward Angle Muon Detection System, which consists of mini-drift tubes (MDTs) and pixel scintillators, is entirely new for Run II. The Run I forward toroids are used, and new shielding has been added. The MDT system covers the region $1.0 \leq |\eta| \leq 2.0$ [86]. The mini-drift tubes have 8 cells of 1 cm

$\times$ 1 cm cross section, and are made of aluminum extruded combs and plastic sleeves. The A layer chambers are in front of the forward toroid magnet and the B and C layers are behind it. The layers are divided into octants. The length of each tube depends on its position in the octant. As in the central region, the MDT A-Layer has four decks of drift tubes and the B and C Layers have three decks each. The coordinate resolution is 0.7 mm/deck. The momentum resolution is 20% for low momentum tracks.

The Muon Forward Scintillator Pixel system covers the same η region [87]. The ϕ segmentation of 4.5 degrees matches the segmentation of the Central Fiber Tracker. The η segmentation is 0.1. The typical size is 20 cm $\times$ 30 cm. The counters are made out of Bicron 404A scintillator. Kumarin WLS bars are used for light collection into PMTs. The scintillators are used for triggering and track reconstruction.

A shielding assembly consisting of iron, polyethylene, and lead is located on either side of the beamline. This shielding prevents particles arising from the interaction of beam remnants with the beam pipe, the forward calorimeter, and the accelerators low-beta quadrupole magnets from traversing the MDTs. The innermost layer of iron absorbs electromagnetic and hadronic showers. Because iron is transparent to slow neutrons, the layer of polyethylene is placed outside the iron to absorb these neutrons. Neutron capture in polyethylene cause emission of gamma rays which are then absorbed by the outside layer of lead.

3.2.5   Triggers and electronics

The D0 Run II Muon Trigger System consists of 3 levels [88]. Level 1 is a pipelined hardware stage. It processes information from individual subdetec-

tors in Field Programmable Gate Arrays (FPGA) with a decision time of 4.2 μs. The decision is based on preliminary information from tracking, calorimetry, and muon systems. The trigger accept rate, which is an output from Level 1, and input to Level 2, is 10 kHz. The second stage, Level 2 or L2, utilizes hardware with embedded microprocessors to construct trigger decisions using individual physics objects as well as correlations between objects at a rate of 1 kHz. It refines Level 1 information and adds more information if available with preprocessors for each subdetector. A global processor combines information from the subdetectors. Level 2 has a maximum decision time of 100μs. A block diagram of the L1 and L2 system data flow is shown in Figure 3.24.

Level 3 has two stages: a custom-built data acquisition system and a Linux farm of processors which makes the final trigger decisions. The farm does partial online event reconstruction and uses filters to accept or reject events. The decision time depends on the number of farm nodes, and is about 50 ms for the beginning of the run. The sustained trigger rate out of Level 3 is 20 Hz, with an output event size of 250 kB.

Overall coordination and run control for the entire trigger system is provided by a program called COOR running on an online host machine. The trigger system also supports prescaling of trigger conditions at all three levels of processing. Prescaled triggers are accepted by the system only a fraction of the time when their trigger condition is satisfied. For example, if a certain trigger has an L1 prescale of 2 only $\frac{1}{2}$ of the events that satisfy the trigger condition will be accepted. Triggers are prescaled depending the instantaneous luminosity, allowing data to keep flowing even during high luminosity beam conditions.

To be able to keep up with an increased input data rate, the front-end
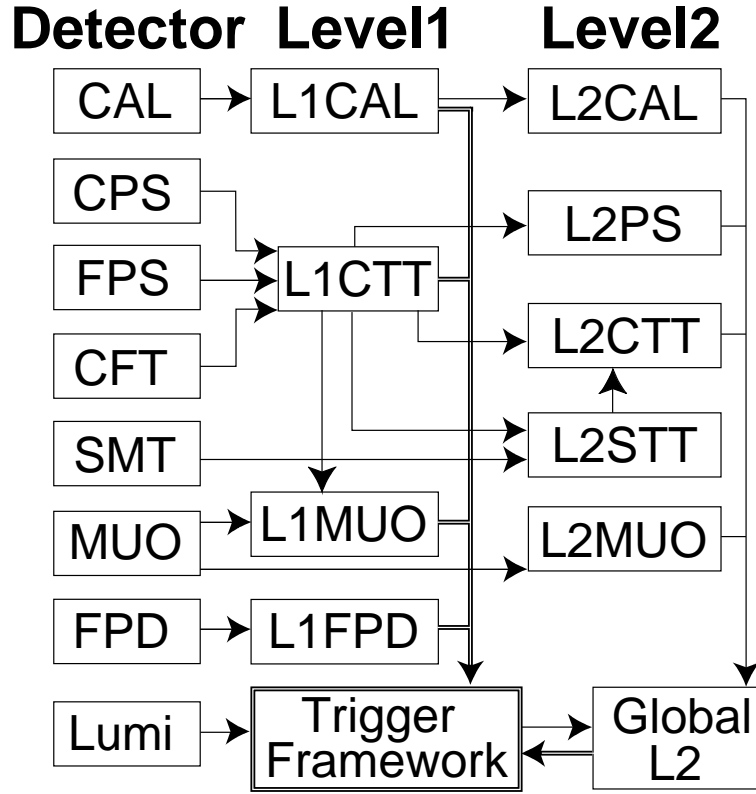
Figure 3.24: Block diagram of the D0 L1 and L2 trigger systems. The arrows show the flow of trigger-related data.

electronics of all the muon subsystems was upgraded. Digital signal processors (DSPs) are used to buffer and reformat the data [89]. The DSPs make muon stubs from hits and buffer the Level 1 accepted data from the frontend readout, while a Level 2 decision is pending. If the trigger is accepted by Level 2, the DSPs reformat the data and send it to the Level 3 trigger system.

The muon trigger has three levels, plus one extra trigger level between Level 1 and Level 2 called SLICs (Second Level Input Computers) [90]. Level

1 triggers uses wire positions, scintillator hits in the A, B and C layers and central, north and south octants to define and/or trigger terms. The SLICs use 80 DSPs to find muon stubs in from nearby hits in a single layer. Level quality values are calculated for all muon candidates. Level 3 uses muon hits, makes muon segments and combines them into muon tracks which are matched with central tracks and calorimeter information. Events passing the trigger requirements are written to tape.

3.2.6 Luminosity counters and Forward Proton Detector

Luminosity is measured using plastic scintillator arrays located in front of the EC cryostats, covering $2.7 < |\eta| < 4.4$. A forward-proton detector, situated in the Tevatron tunnel on either side of the interaction region, consists of a total of 18 Roman pots used for measuring high-momentum charged-particle trajectories close to the incident beam directions.

Chapter 4

Data sample

The events are read out from the D0 detector in the form of a 'raw data' event.
It is given as set of quantities such as digitized counts in a calorimeter cell,
ADC counts for the silicon or central fiber tracker, and so on.

In order to obtain variables interesting from the physics point of view such
as kinematical parameters of physics objects, the event has to be reconstructed.
It means that all digitized counts have to be turned into description of objects
as leptons and jets. This process is carried out by a set of computer pro-
grams (packages) called d0reco. Reconstruction is the first step in the D0 data
processing chain (after recording). The D0 reconstruction program (d0reco)
converts raw data into reconstructed data (dsts and thumbnails). Thumbnails
have the format of reconstructed data, where the original Data Summary Tape
(DST), which contains a full information about the event in all phases of re-
construction process, raw data including, is compressed into thumbnail format
by dropping information that is not needed from physics analysis perspective,
e.g. all hit or cluster information in the tracking system. This is economic from
the point of view of a disk space, however, some information that is useful or

needed for a detailed understanding of some effects is lost that way.

The reconstruction step is done on a reconstruction farm. Reconstruction is the most costly step in the data processing chain in terms of cpu time. In the case of data, this step can only be done easily at Fermilab due to the requirement of having fast access to large calibration databases. The reconstruction program consists of following consecutive steps.

- Hit finding - raw data is unpacked and converted into 'hits'.

- Clustering and tracking - hits that are close to each other are formed into objects called clusters. Tracking part of the code builds clusters into 'tracks', this part is called track finding and track fitting. In the calorimeter, clusters are grouped together into jets.

- Vertexing - vertexing code combines tracks and finds their common crossing - a vertex. Primary vertices and secondary vertices are found.

- Particle identification - information from all parts of the detector is combined to produce collections (lists) of objects which are candidates for tracks, electrons, photons, jets or muons. At this level, criteria to build all these objects are very loose so that no potentially interesting objects are lost at this stage.

In this analysis Common Analysis Format (CAF) based on the tmb_tree was used as data format. The CAF is an object-oriented and ROOT based data format using TTree as its basic storage mechanism. In CAF there are reconstructed objects, trigger information, object ID information and detector data information.

The pre-selection cuts are supposed to select a set of data that is particularly interesting for a given analysis. When performing an analysis, the researcher typically decides for much tighter selection criteria defining his/her data set. All the cuts, reconstruction, pre-selection, selection and analysis cuts, are described in detail in what follows.

4.1   General strategy

First of all, in this chapter, general strategy to search for doubly-charged Higgs boson will be presented. From the fact that H$^{\pm\pm}$ bosons are typically boosted, the angle of two muons from H$^{\pm\pm}$ bosons is therefore smaller and the p_T of muons from H$^{\pm\pm}$ bosons decays is higher than the one of muons from Z decays. Two like-sign muons pairs are expected as the final states. In this analysis to search these pairs the following strategy has been considered.

- A pair of the like-sign isolated muons with small opening angle and a third muon defined in Section 4.3 are required as the final states. The third muon requirement increased the sensitivity for the Higgs bosons search.

- Z $\to \mu\mu$, QCD and di-bosons ($ZZ/WZ/WW$) are considered as the main backgrounds. All backgrounds except QCD contribution are simulated with Monte Carlo method. The QCD background is obtained from non-isolated data sample.

4.2   Data set definition

This analysis is based on the RunIIa data set collected with the D0 Detector at the Fermilab Tevatron Collider from April 19, 2002 to February 22, 2005 corresponding to the run range 160582-215670. This data set consists of skimmed refixed data and re-skimmed unfixed data [94]. The first data set is reconstructed with the p17.09.03 version of d0reco. The latter data set includes non-cable-swap and cable-swap data. Cable-swap data taken near the end of RunIIa has been re-reconstructed with the d0reco p17.09.06 version.

The selection uses 2MUhighpt data set. This skim requires two loose muon with transverse momentum (p_T) greater than 10 GeV/c. The transverse momentum of the muon is measured using central tracking system, if the central was found, or by the muon system in case no central track was matched to the track reconstructed in the muon system. This skim is intentionally very loose. Users are expected to apply further cuts which can be tailored to suit the particular analysis being carried out.

CAF trees that have been used in this analysis have been produced in the p18.05.00 release. All LBNs and runs with bad CFT, SMT, CAL and MUO quality are rejected [95] using the data quality package (dq-defs package, tag v2006-10-10) [95]. This package is provided by the D0 Data Quality Group. Also, duplicate events are removed using the Processor FindDuplicateEvents.

The total integrated luminosity calculated using lm_tools is 1058.12 pb^{-1}. The integrated luminosities for the data samples are shown in Table 4.1. The events are required to pass the ORing of di-muon and single-muon triggers. The triggers used and the corresponding run ranges are listed in Table 4.2 and Table 4.3, according to the trigger versions.

Table 4.1: luminosity for the di-muon sample using lm_tools

Sample	Trigger	delivered	recorded	recorded (good)
v8.0-v9.0	2MU_A_L2M0	42.58	31.81	26.64
v9.0-v10.0	2MU_A_L2ETAPHI	47.89	41.76	24.75
v10.0-v11.0	2MU_A_L2ETAPHI	21.43	19.35	10.75
v11.0-v12.0	2MU_A_L2ETAPHI	79.27	74.34	65.24
v12.0-v13.0	2MU_A_L2M0_TRK5	273.91	252.10	228.97
v13.0-v13.3	DMU1_TK5	81.84	73.37	53.69
v13.3-v14.0	DMU1_TK8	381.22	343.78	314.67
v14.0-v14.6	DMU1_2LM6	180.08	168.51	142.26
v14.6-v15.0	DMUA_2LM6	236.96	220.61	181.15

4.3   Event selection

The $H^{++}H^{--}$ signal would be observed as a bump in the like-sign di-lepton mass distribution. Therefore, the event selection requires that there are two like-sign muons with an additional muon as a final state. However, as it has been well known in the past analysis, mis-measured or poorly measured tracks can lead to like-sign lepton pairs, frequently they have smaller number of hits and/or are of high p_T. Therefore, the two muons that enter to the construction of a di-muon invariant mass and $\Delta\phi$ between the muons are required to have good quality tracks. If a third muon is present and also passes the tight track quality criteria, all muon pairs are considered to select events. For this case the event if there is a like-sign muon pair with small opening angle is

Table 4.2: Trigger selection for di-muon triggers

Sample	run range	trigger selection
v8 - v10	160582-174802	2MU_A_L2M0
v11	174845-178721	2MU_A_L2M0 2MU_A_L2ETAPHI
		2MU_A_L2M0_TRK10 2MU_A_L2M0_L3L15
v12	178722-194566	2MU_A_L2M0 2MU_A_L2ETAPHI 2MU_A_2L2M
		2MU_A_L2M0_TRK5 2MU_A_L2M0_L3L6 2MU_A_L2M0_2L3M0
v13	194567-202024	DMU1_TK5 DMU1_LM6
v13.30	202025-208500	DMU1_TK8 DMU1_LM5_TK5 DMU1_LM15
v14	207217-215670	DMU1_2LM6 DMU1_LM6_TK12 DMU1_TK8_TLM8
		DMUA_2LM6 DMUA_LM6_TK12 DMUA_TK8_TLM8

Table 4.3: Trigger selection for single-muon triggers

Sample	run range	trigger selection
v8 - v10	160582-174802	MU_W_L2M5_TRK10 MU_W_L2M0_TRK3
		MU_W_L2M0_TRK10 MUW_W_L2M5_TRK10
v11	174845-178721	MUW_A_L2M3_TRK10 MUW_W_L2M3_TRK10
		MU_W_L2M3_TRK10
v12	178722-194566	MUW_W_L2M3_TRK10 MU_W_L2M3_TRK10
		MU_A_L2M3_TRK10
v13	194567-202024	MUH1_TK12 MUH1_LM15 MUH1_TK10 MUH1_TK12_TLM12
		MUH2_LM3_TK12 MUH2_LM15 MUH2_LM6_TK12
		MUH3_LM3_TK10 MUH3_LM15 MUH3_LM6_TK12
		MUH4_TK10 MUH4_LM15
		MUH5_LM15
		MUH6_TK10 MUH6_LM15 MUH6_TK12_TLM12
		MUH7_TK10 MUH7_LM15 MUH7_TK12
v13.30	202025-208500	MUH1_LM15 MUH1_TK12_TLM12 MUH1_TK10H
		MUH2_LM10_TK12 MUH2_LM4_ITK10
		MUH3_LM10_TK12 MUH3_LM4_ITK10
		MUH5_LM15
		MUH6_TK12_TLM12 MUH6_LM15
		MUH7_TK12 MUH7_LM15
v14	207217-215670	MUH1_TK12_TLM12 MUH1_ILM15 MUH1_ITLM10
		MUH8_TK12_TLM12 MUH8_ILM15 MUH8_ITLM10

finally selected. In the previous version of the analysis, there were not enough candidates remaining after requiring a like-sign muon pair, so the requirement of a third muon was not made. In this analysis, a third muon is required and it is found to enhance the signal significance.

S1 The di-muon triggers and single muon triggers are required to have fired in the data sample. The list of triggers that are used in this analysis is shown in Table 4.2 and Table 4.3.

Muons in D0 can be identified through three independent detector subsystems. The 3 layer muon detector system with its toroid magnet covers more than 90% of the angular acceptance up to a pseudo-rapidity $|\eta| = 2$. It provides unambiguous muon identification with a momentum measurement. A muon identified on the basis of the information provided by the muon detector is called a "local muon".

The central tracking system which consists of the Silicon Micro-strip Tracker (SMT) and the Central Fiber Tracker (CFT) provides accurate momentum resolution and is highly efficient at finding tracks in the whole angular acceptance of the muon detector. A local muon that is successfully matched with a central track is called a "central track-matched muon".

A third independent muon confirmation can be obtained by looking for a MIP signature in the calorimeter. The capability to identify muons using the calorimeter is called "Muon Tracking in the Calorimeter" or "MTC" and is still in development. The current MTC algorithm has a typical efficiency of about 50%, far less efficent than the other muon

signatures.

In this analysis the certified Muon Identification (Muon ID) definitions to be used with the p17 data arising from version of the D0 event reconstruction software and passed through the p18 version of d0correct.

Muon ID version 1 with muon quality "Medium" within the MuonSelector of release p18.08.00 has been used. The momentum is taken from the measurement in the central tracker which consists of the Central Fiber Tracker (CFT) and the Silicon Microstrip Tracker (SMT). Presence of at least two offline muons which pass the following selections is required.

- transverse momentum $p_T > 15$ GeV

- pseudorapidity $|\eta| < 2.0$.

- medium muon quality

- matched to a central track with the number of hits in the CFT layers ≥ 5 and the number of hits in the SMT layers ≥ 2. This hit requirement reduces the charge flip probability [100] as well as background from badly reconstructed tracks.

- cosmic veto using timing cut [101].

- invariant mass > 30 GeV

S2 In order to remove the QCD background coming mainly from muons originating from semi-leptonic b decays, isolation criteria based on the calorimeter and tracking information are applied The isolation criteria are defined as follows. The sum of the transverse energies of the cells in a annular ring around the muon direction is required to be

$$\sum_{cell,i} E_T^i < 2.5 \text{ GeV, for } 0.1 < R < 0.4 \tag{4.1}$$

where $R = \sqrt{\Delta\phi^2 + \Delta\eta^2}$. A similar condition is defined for the total transverse momentum of all tracks excluding the one matched to the muon in a cone of radius 0.5 centered around the muon,

$$\sum_{tracks,i} p_T^i < 2.5 \text{ GeV, for } R < 0.5 \tag{4.2}$$

S3 To reject background from $Z \rightarrow \mu^+\mu^-$ and QCD events, the angle $\Delta\phi$ between the two muons is required to be less than 2.5, since two muons from Z decays are mostly back-to-back. If there are more than 2 muons satisfying S1 and S2 in an event, all possible pairings are considered and if at least one pair satisfies $\Delta\phi < 2.5$, then the event is selected. This requirement rejects, in addition to $Z \rightarrow \mu^+\mu^-$ events, some of the remaining muons from the semi-leptonic decays of b quarks in jets that were not removed by the isolation requirement S2.

S4 Require the two muons which fulfilled S1, S2 and S3 in the event to be of like-sign charge. This requirement is also used for instrumental background calculations.

S5 Require a third muon. The momentum is corrected using the position of the primary vertex when there is no SMT hit, this only pertains to the third muon which is not required to have CFT and SMT hits. The third muon is considered for the previous selections only when it has good quality track. The third muon should satisfy the following selections:

- transverse momentum $p_T > 15$ GeV

- pseudorapidity $|\eta| < 2.0$

- medium muon quality

- matched to a central track without requirements on the number of SMT and CFT hits.

- cosmic veto using timing cut

- Isolation requirement (S2)

A third muon can, therefore, enter in two different cases:

- if the SMT/CFT hit requirements are fulfilled, the third muon is considered in the requirement on the invariant mass, the opening angle (S3) and the like-sign (S4).

- if the SMT/CFT hit requirements are not fulfilled, the muon is not considered for requirement on the invariant mass, the opening angle (S3) and the like-sign (S4).

In case of three like-sign muons passing the selection criteria S1, S2 and S3, the two muons with the highest p_T are referenced in the following as "the muon pair".

4.4 Muons from Cosmic

Cosmic muons can have a very high transverse momentum, this is why their invariant mass can be also rather high. Due to their high p_T, a charge flip on one of the tracks matched to a local muon might occur and such an event is then considered to be a like-sign event. The charge flip happens more likely

for high-p_T tracks because the curvature (q/p_T) is small and any effect due to spatial resolution or misalignment is going to increase probability for the track to flip a charge. The charge of a track is derived directly from the sign of a track curvature. Therefore, any contamination of data with cosmic muons has to be avoided.

Muons from cosmic rays passing through the detector can be reconstructed as back to back, opposite charge muons. In the case that the muon is only reconstructed entering or leaving the detector a cosmic muon can appear as a single muon event. To reject cosmic muons, cuts on muon scintillator hit time, track dca, and acolinearity between central tracks can be used.

In this analysis the cosmic muon is removed on the level of preselection by using only timing cuts. The method to remove the cosmic muon with timing cuts, dca cuts and acolinearity are described in what follows respectively.

Timing Cuts

As the arrival of cosmic muons is uncorrelated with a $p\bar{p}$ collision, they typically produce 'out of time' hits. Muons from collisions produce hit times close to zero, so cosmic muons can be rejected by (when information available):

- -10 ns < A-layer time < 10 ns

- -10 ns < B-layer time < 10 ns

- -10 ns < C-layer time < 10 ns

These cuts are implemented in the isCosmic() flag in MuoCandidate.

Cuts on scintillator times alone do not reject all cosmic muons - the scintillator trigger gates to preferentially select cosmic muons which have hit times

close to zero, reducing the effectiveness of this cut.

However, in the case of di-muon events, a cut on the time difference between the A-layer hits on each muon (Δt_A) is very effective against cosmic muons. Typically, it takes a cosmic muon around 20 ns to cross the distance between the A-layer on one side of the detector and the A-layer on the other side (around 6 m), so requiring $\Delta t_A < 12$ ns rejects most of these.

dca Cuts

When a muon is matched to a central track, a cut on the track dca is very effective against cosmic muons, as they are not constrained pass through the beam position in x-y.

In the case of fairly 'empty' events (such as Z$\rightarrow \mu\mu$ or W$\rightarrow \mu\nu$), using the track dca to the beam spot is necessary. For higher occupancy events (e.g. muon plus jets), the primary vertex is in principle more reliable and could be used. But as the tracking efficiencies have been measured in a Z$\rightarrow \mu\mu$ sample, it is recommended to use the beam position in any case.

When using the primary vertex, requiring a match between the vertex and the muon track in z of around 3 cm is also an effective cut.

The timing cuts with a cut of dca < 0.2 cm is implemented in the isCosmicTight() flag in MuoCandidate. Unfortunately in p17 version, this dca is computed relative to (0,0), so that the CosmicTight flag is sensitive to the beam displacement. So it should be considered that this flag is bugged and it is recommended not to use it.

Acolinearity Cuts

Acolinearity (really, this is pseudo-acolinearity), which can be used in di-muon events, where both muons are track-matched. Acolinearity between the two muon tracks is defined as:

$$A = \pi - |\Delta\phi| + |\sum \theta - \pi|, \tag{4.3}$$

where $\Delta\phi$ and $\sum \theta$ are the angles between the two tracks. Cosmic muons pass straight through the detector, producing back to back tracks with small acolinearity. Requiring $A > 0.05$ rejects most cosmic muons.

However, this method is more likely to also reject signal events in which another track happens to be back to back with the muon, and should be studied before use.

Chapter 5

Monte Carlo samples

This chapter will present the generation of the signal Monte Carlo sample as well as of the expected physics backgrounds that contribute to the data sample. The backgrounds that give 2 like-sign muons and additional muon as final state should be considered as the expected physics backgrounds. The dominant backgrounds in the four muon mode arise from electroweak processes where real high-p_T muons are created from W and Z decays along with either fake muons or muons from heavy flavor decays (semi-leptonic b decays, for instance, where the same-charged muons come from B-hadron mixing). The backgrounds are diboson production: $ZZ \to 4\mu$, $WZ \to 3\mu + \nu$ or $WW \to 2\mu + 2\nu$; $t\bar{t}$ production: $t\bar{t} \to \mu^+ \nu b \mu^- \bar{\nu} \bar{b}$; $b\bar{b}$ production (charge mis-identification may occur); and boson plus jets: W+jets, Z+jets where $W \to \mu\nu$, $Z \to \mu^+ \mu^-$ and the jets produce real or fake muons.

The Standard model backgrounds and signal processes have been generated with PYTHIA 6.323.

5.1   Signal Monte Carlo simulation

PYTHIA Monte Carlo allows process:

$$p\bar{p} \to Z^0/\gamma X \to H^{--}H^{++}X, \tag{5.1}$$

with the H$^{\pm\pm}$ forced to decay to like-sign muon pairs. The signal samples are generated in steps of 10 GeV in the mass range $90 < M(\text{H}^{\pm\pm}) < 200$ GeV with the d0reco version p17.09.06. The CAF trees for the signal samples were produced using the TMBanalyze p18.08.00 software package. Momenta of the simulated muons are smeared using the ApplyMuonSmear processor in the caf_util package.

5.2   Background Monte Carlo simulation

The integrated luminosities corresponding to the number of generated events for all background Monte Carlo samples and cross sections used in this analysis are shown in Table 5.2. These integrated luminosities corresponding to generated events are used for the normalization of the generated samples. All Monte Carlo background samples are processed with the d0reco versions p17.09.01 and p17.06.02. The CAF trees for the simulated MC background samples were produced using the TMBanalyze p18.05.00 software package.

5.2.1 $Z \to \mu\mu$ background

The Z$\to \mu\mu$ background sample was generated on the farms. The generation of Z decays includes the Drell-Yan contribution. The generation is broken into smaller mass windows so that a sufficient statistics/luminosity is obtained even

for the tails of the mass distribution. The $Z/\gamma \to \mu\mu$ cross section is calculated with CTEQ6L1 PDFs as $\sigma(Z/\gamma \to \mu\mu) = \sigma_{\mathrm{LO}} \times K_{\mathrm{QCD}}(Q^2)$, with the LO cross section calculated by PYTHIA LO PDF and the K_{QCD} at NNLO with NLO PDF, calculated according to [96]. This Z$\to \mu\mu$ background sample contains Z $+$ $b\bar{b} \to \mu\mu$ $+ b\bar{b}$. The Z $+$ $b\bar{b}$ sample has been generated and analyzed separately. After all selection the remaining events of the Z $+$ $b\bar{b}$ sample is found to be nothing. Z $+$ $b\bar{b}$ contributes very small fraction of Z$\to \mu\mu$ + jets. It is negligible after final selection.

5.2.2 $Z \to \tau\tau$ background

The Z$\to \tau\tau$ background is not the type of background that contributes to like-sign backgrounds significantly. However, similarly to $Z \to \mu\mu$ sample, some of the events might contain a high-p_T track that is badly reconstructed with the opposite sign of the charge. An event that was generated as an opposite-sign event is, in such a case, considered to be the same-sign event and it there-fore contributes to the same-charged background. The transverse momentum distribution of muons in this sample is obviously much softer than in Z$\to \mu\mu$ events due to the 3-body decay of τ-leptons. Thus the invariant mass of Z$\to \tau\tau$ peaks sooner (in lower masses) and falls down to zero much faster than in case of the Z$\to \mu\mu$ background.

5.2.3 $t\bar{t}$ and di-boson backgrounds

The $t\bar{t}$ cross section is calculated at NNLO in [97] and the WW, ZZ and WZ cross sections are calculated in [98] with MCFM using CTEQ6L1 PDFs. Here since ZZ decay to all possible leptons (e, /mu, /tau), the number of ZZ background events at the preselection level appears to be much large than $ZZ \rightarrow 4\mu$. $ZZ \rightarrow 4\mu$ has been analyzed separately. The remaining events after each selection is given in Table 5.1. The contribution of $ZZ \rightarrow 4\mu$ is found to be 0.39 after final cut. The contribution of $ZZ \rightarrow 4\tau \rightarrow 4\mu$ and $ZZ \rightarrow 2\tau2\mu \rightarrow 4\mu$ is determined by subtracting 0.39 events from 0.5 events in this analysis. 0.11 events is found to be the contribution of $ZZ \rightarrow 4\tau \rightarrow 4\mu$ and $ZZ \rightarrow 2\tau2\mu \rightarrow 4\mu$. It would make no big difference at the end. It is, however, better to include all final states of the Z decays.

Selection	$ZZ \rightarrow 4\mu$	$ZZ \rightarrow 4l$ or $2l + 2\nu$
S1	1.1	11
S2	0.98	9
S3	0.81	5
S4	0.49	0.6
S5	0.39	0.5

Table 5.1: The remaining events after each selection for $ZZ \rightarrow 4\mu$ and $ZZ \rightarrow 4l$ or $2l + 2\nu$.

Process	Mass Range [GeV]	$\sigma \times \text{Br[pb]}$	$\text{L[pb}^{-1}]$
$Z/\gamma^* + X \rightarrow \mu\mu + X$	$15 < M < 60$	455 ± 16.8	3253.16
$Z/\gamma^* + X \rightarrow \mu\mu + X$	$60 < M < 130$	242 ± 8.2	5332.93
$Z/\gamma^* + X \rightarrow \mu\mu + X$	$130 < M < 250$	1.96 ± 0.6	97831.63
$Z/\gamma^* + X \rightarrow \mu\mu + X$	$250 < M < 500$	0.167	287500
$Z/\gamma^* + X \rightarrow \tau\tau + X$	$15 < M < 60$	455 ± 16.8	2062.31
$Z/\gamma^* + X \rightarrow \tau\tau + X$	$60 < M < 130$	242 ± 8.2	5011.36
$Z/\gamma^* + X \rightarrow \tau\tau + X$	$130 < M < 250$	1.96 ± 0.6	82270.41
$t\bar{t} \rightarrow bbll\nu\nu$		0.70 ± 0.04	147857
$WW \rightarrow 2l + 2\nu$		1.08	332024
$WZ \rightarrow 3l + \nu$		0.1104	2411685
$ZZ \rightarrow 4l$ or $2l + 2\nu$		0.071	2873239

Table 5.2: This table shows the integrated luminosities corresponding to the number of generated events for all background Monte Carlo samples and cross sections used in this analysis.

5.2.4 W+jets background

The W+jets MC sample has been analyzed with the same selection criteria. The NLO cross section $\times$ branching ratio of 2583 pb^{-1} has been used to normalize the W+jets MC sample. Only 2.5 events pass the isolation cut (S2). While the muon from the W is isolated, the other muon is inside a jet. This is why the second muon barely pass the isolation cut. Once the like-sign requirement is applied, there is no event left. The contribution of W+jets in this analysis, therefore, is found to be negligible.

Selection	Muon ID (medium)	Isolation (S2)
$Z \rightarrow \mu\mu$	0.96	1.00
Signal (140 GeV)	0.93	1.00

Table 5.3: The average DATA/MC corrections for $Z \rightarrow \mu\mu$ and signal.

5.3 Reconstruction efficiency corrections

5.3.1 Muon ID and isolation correction

Data to MC muon reconstruction and isolation efficiency scale factors have been applied to the simulated muons to take into account the difference between the reconstruction efficiencies in data and Monte Carlo. These scale factors are available in the software package muid_eff v02-00-00. By using this package the correction is automatically taken into account event by event. The average DATA/MC corrections for $Z \rightarrow \mu\mu$ and signal are given in Table 5.3.

5.3.2 Trigger efficiency correction

Trigger corrections are not applied to the Monte Carlo sample. Instead, the Monte Carlo samples are normalized to the data using the Z bosons in the data between 60GeV to 130GeV after requiring the preselection and isolation cuts (S1 and S2) which are defined in Section 4.3. A effective integrated luminosity of about 1050 pb^{-1} is determined by applying this normalization. In the muon $p_T > 15$GeV range, the trigger efficiency is essentially flat as a function of p_T. There is no trigger bias shown in Figure 5.1 which is the ratio of the distribution of the di-muon invariant mass and leading p_T with trigger
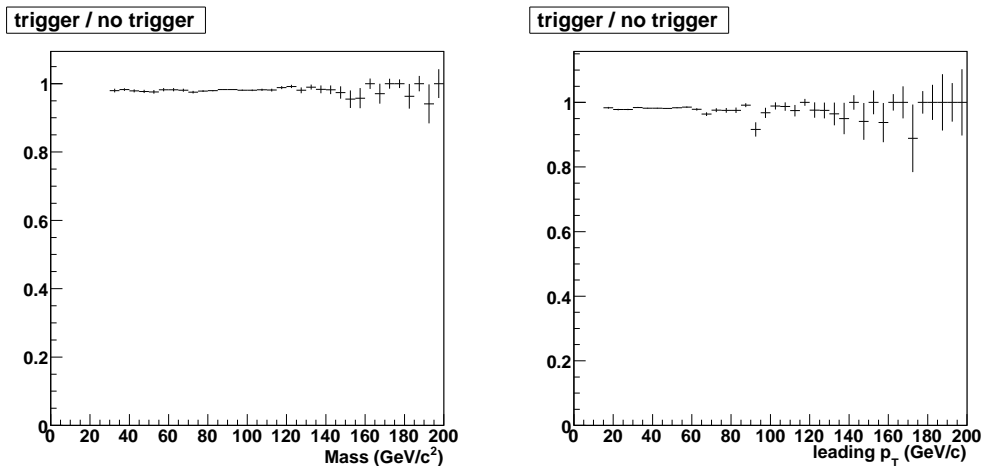
Figure 5.1: The ratio of the distribution as a function of the di-muon invariant mass and leading p_T with trigger requirement to without trigger requirement.

requirement to without trigger requirement. The data quality package (dq-defs package, tag v2006-10-10) [95] has been applied to the MC CAFE trees and the normalization of the number of events were done before the application of the data quality selection.

5.3.3   charge flip rate correction

The charge flip rate is obtained from both data and the simulated $Z \to \mu\mu$. Since the simulated $Z \to \mu\mu$ underestimates the charge flip rate an additional correction factor is applied to $Z \to \mu\mu$ MC. The charge flip probability is described in great details in Chapter 7.

5.3.4 Z-p_T re-weighting

It is already known that the p_T distribution of the Z bosons from the PYTHIA simulation does not properly describe the data. Therefore a weight is applied to each MC event according to the results given in Ref. [102], where the PYTHIA samples are tuned for the different Z/γ^* mass ranges as a function of p_T using $146\,\mathrm{pb}^{-1}$ of RunI data. The measurement for RunII data agrees well with RunI measurement in the di-em channel with resummed NLO calculations and with a tuned version of the leading order parton shower MC PYTHIA. The ratio of the tuned versus default MC is fitted using a modified Fermi function. The fits are performed in four different mass bins (15GeV < M < 30GeV, 30GeV < M < 60GeV, 60GeV < M < 130GeV, 130 GeV < M < 250GeV).

Chapter 6

QCD background

The QCD background is one of the main background in this analysis. The QCD background is the natural source of a large like-sign di-muon background. Like-sign muon pairs in these events are produced through neutral B-hadron mixing. Simulation of this background with PYTHIA does not give satisfactory results. Th estimation of the QCD background contribution, therefore, is achieved by using data sample. In this chapter the estimation of the QCD background contribution and the efficiency for QCD are will be presented.

6.1 The estimation of QCD background

The QCD background contribution was estimated directly from the data sample. The previous analysis has shown that the QCD background is mostly from semileptonic decays of $b\bar{b}$, where a cascade decay by one of the b quarks can lead to a like-sign muon pair. All estimations of the QCD background were made after applying the preselection (S1). Differential distributions of QCD background were obtained by inverting the isolation cut ($\sum_{cell,i} E_T^i \geq 2.5$ GeV

and $\sum_{tracks,i} p_T^i \geq 2.5$ GeV) for both muons. $N_{\text{data}}^{\text{non}-\text{iso}}$ is defined as the number of the events in this selection: the number of events after preselection (S1) with the two muons not fulfilling the isolation criteria. We extrapolate the QCD estimate from the non-isolated region to the isolated region of the phase space by applying a normalization factor f_{QCD}. The number of like-sign events $N_{\text{QCD}}^{\pm\pm}$ is estimated from the excess of like-sign events $N_{\text{data}}^{\pm\pm}$ above the expected contribution $N_{\text{MC}}^{\pm\pm}$ from all standard model backgrounds: $N_{\text{QCD}}^{\pm\pm} = N_{\text{data}}^{\pm\pm} - N_{\text{MC}}^{\pm\pm}$. Here $N_{\text{data}}^{\pm\pm}$ and $N_{\text{MC}}^{\pm\pm}$ are defined as the number of data and MC events after the preselection (S1) in like-sign sample (S4), respectively. The normalization factor f_{QCD} for the QCD sample is obtained by taking the ratio of the number of like-sign QCD events to the number of non-isolated events in the like-sign sample ($N_{\text{data}}^{\text{non}-\text{iso},\pm\pm}$) at the preselection level (S1). The normalization factor f_{QCD} is defined as

$$f_{\text{QCD}} = \frac{N_{\text{data}}^{\pm\pm} - N_{\text{MC}}^{\pm\pm}}{N_{\text{non}-\text{iso}}^{\pm\pm}} = \frac{N_{\text{QCD}}^{\pm\pm}}{N_{data}^{\text{non}-\text{iso},\pm\pm}} \qquad (6.1)$$

The QCD background contribution at preselection level (S1) before applying the like-sign requirement (S4) is obtained by multiplying f_{QCD} to the number of non-isolated events in the unlike-sign sample, $N_{\text{data}}^{\text{non}-\text{iso},\pm\mp}$ without the like-sign requirement (S4):

$$N_{\text{QCD}}^{\pm\mp} = f_{\text{QCD}} \times N_{\text{data}}^{\text{non}-\text{iso},\pm\mp} \qquad (6.2)$$

6.2 The isolation efficiency for QCD

The isolation efficiency is obtained in the like-sign sample. Assuming that events remaining after subtracting Monte Carlo from data are all QCD events,
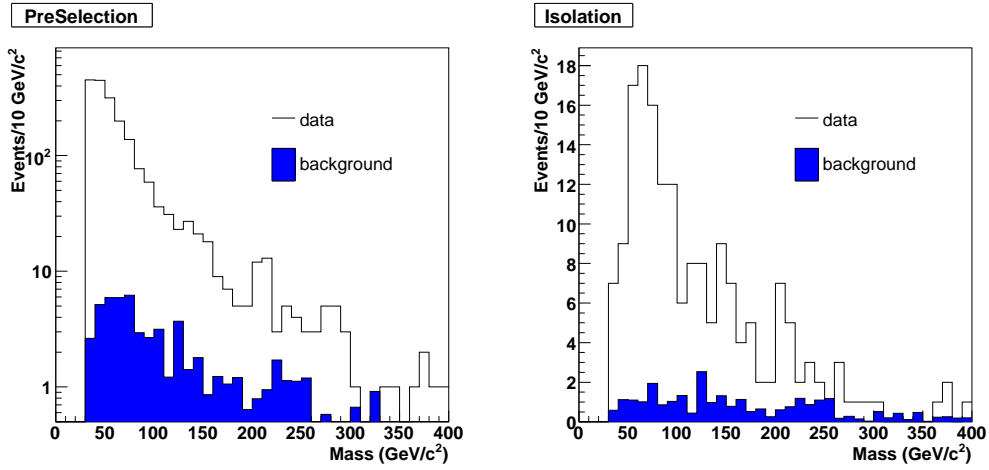
Figure 6.1: In the left plot the di-muon invariant mass distributions for data and all MC backgrounds at the preselection (S1) are shown in like-sign sample. In the right plot the di-muon invariant mass distributions are shown after the isolation requirement (S2) in like-sign sample. The data after subtracting MC backgrounds are considered as QCD events in like-sign sample. The number of data and all Monte Carlo backgrounds after each selections (S1 and S2) in like-sign sample are given in Table 6.1.
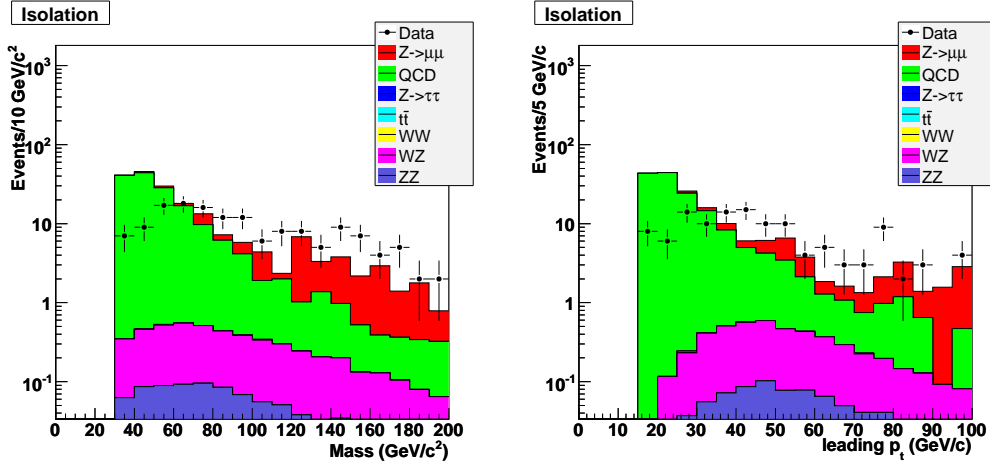
Figure 6.2: The di-muon invariant mass and leading p_T distributions after requiring the preselection (S1) and isolation cuts (S2) in like-sign sample (S4) without applying the p_T dependent correction factor. In the low mass range QCD derived from non-isolated sample is not described well.

the isolation efficiency for QCD is defined as

$$\epsilon_{\text{iso}} = \frac{N_{\text{data}}^{\text{iso},\pm\pm} - N_{\text{MC}}^{\text{iso},\pm\pm}}{N_{\text{data}}^{\pm\pm} - N_{\text{MC}}^{\pm\pm}} = (8.07 \ \pm \ 0.7)\% \qquad (6.3)$$

where $N_{\text{data}}^{\text{iso},\pm\pm}$ and $N_{\text{MC}}^{\text{iso},\pm\pm}$ are the number of data and MC events after the isolation requirement (S2) in like-sign sample (S4), respectively.

The di-muon invariant mass distributions of data and MC backgrounds used for this calculation are shown in Figure 6.1. To get an estimation of the QCD contribution after applying the isolation requirement (S2), the isolation efficiency from QCD is multiplied to the QCD contribution. The number of data and Monte Carlo backgrounds after each selections (S1 and S2) in like-sign sample are given in Table 6.1.
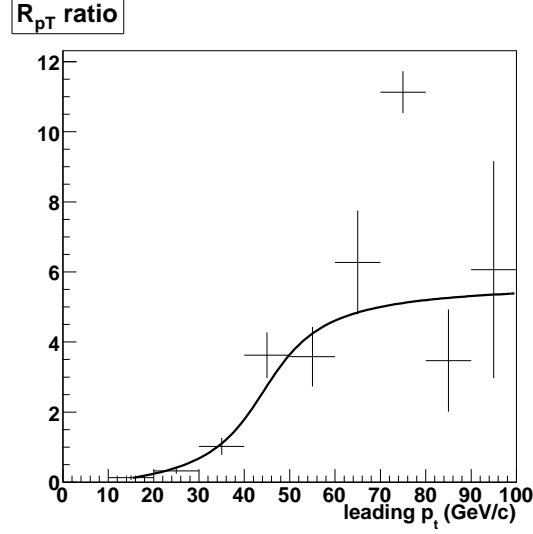
Figure 6.3: The fit for the p_T dependent correction obtained with $\Delta\phi > 2.5$. Two 5 GeV bins are merged into one 10 GeV bin to get the fit function. The arctangent function is used to fit the ratio.

In the like-sign sample, comparison of data and MC shows that the p_T distribution of the leading muon is not well described (see Figure 6.2) due to a p_T dependence of the isolation probability in the QCD sample. The p_T dependent correction is derived in the like-sign sample using the leading muon p_T. However, to avoid signal bias, the data in the range $\Delta\phi > 2.5$ are used(see Figure 8.6). The ratio for the p_T dependence is defined as

$$f(p_T) = \frac{(N_{\text{data}}^{\text{iso}} - N_{\text{MC}}^{\text{iso}})|_{\Delta\phi>2.5}}{N_{\text{QCD}}^{\text{iso},\pm\pm}} \qquad (6.4)$$

where $N_{\text{QCD}}^{\text{iso}}$ is the QCD contribution derived from non-isolated sample as described earlier.

The p_T dependence of the correction factor is shown in Figure .6.3 and the

following function is used to fit the ratio

$$f(p_T) = \frac{1}{2}\tan^{-1}(\frac{x}{10} - 4.5) + 2.6 \qquad (6.5)$$

The value of the function is applied as an additional event weight. After using this function QCD contribution after the isolation cut described the data better (see Figure 8.6). The number of each events for this estimation are given in Table 6.2.

Table 6.1: This table shows the number of data and Monte Carlo backgrounds after each selections (S1 and S2) in like-sign sample. The number of data events remaining after subtracting Monte Carlo backgrounds is considered as QCD events in like-sign sample.

Selection (S4)	S1	S2
data	1966	187
MC backgrounds	59	27

Table 6.2: This table shows the number of $N_{\text{non}-\text{iso}}$ and QCD after each selections (S1 and S2). The first raw is corresponding to the events without like-sign requirement while the second raw to the events with like-sign requirement. The number of events in second and third column are the number of QCD events after the preselection (S1) and the isolation requirement (S2) respectively.

Selection	$N_{\text{non}-\text{iso}}$	$N_{\text{data}}^{\text{non}-\text{iso}} \times f_{\text{QCD}}$ $= N_{\text{QCD}}$	$N_{\text{data}}^{\text{non}-\text{iso}} \times f_{\text{QCD}} \times \epsilon_{\text{iso}}$ $= N_{\text{QCD}}^{\text{iso}}$
without like-sign cut	3334	5244	423
with like-sign cut (S4)	1206	1897	153

Chapter 7

Charge flip probability

There is no main background in standard model such as like-sign muons. The charge flip, therefore, plays a key role in the background contribution. In this chapter, it will be shown where the charge flip could occur, how it affect the transverse momentum of the mis-identified muon and the charge flip probability for data and simulated $Z \to \mu\mu$.

7.1 Understanding of the mis-identified muons

There are two sources that cause charge to be mis-identified. The first source of charge mis-identification is due to the limited CFT acceptance at high η. Tracks in the region with CFT detector $|\eta| > 1.63$ have less than 16 CFT hits 3.14. The less hits a muon has, the more the charge of the muon tends to be mis-identified. The second source is from very high p_T tracks. The uncertainty on the measured curvature and a possible residual mis-alignment can cause a charge flip. These effects are included in the Monte Carlo simulation but they are underestimated.
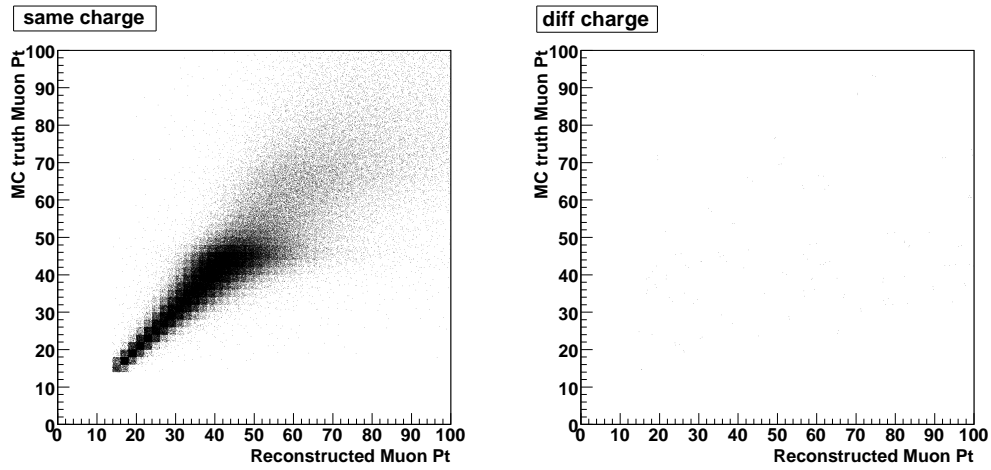
Figure 7.1: When the charge of the MC truth muon is same as the reconstructed muon, the p_T of the reconstructed muon increases in proportion as the p_T of the MC truth increases in left plot. If the charge of the muon is mis-identified, the p_T of the reconstructed muon does not correlate with the p_T of the MC truth in right plot.

The plots in Figure 7.1 shows if the reconstructed muon is mis-identified, the transverse momentum of the reconstructed muon is distorted. In Figure 7.1 the correlation between the p_T of the reconstructed muon and the p_T of the MC truth muon is shown using MC $Z \rightarrow \mu\mu$ at preselection level. When the charge of the MC truth muon is same as the reconstructed muon, the p_T of the reconstructed muon increases in proportion as the p_T of the MC truth increases in the left plot. If the charge of the muon is mis-identified, the p_T of the reconstructed muon does not correlate with the p_T of the MC truth in the right plot.

Interesting variables to plot are the p_T and physics η of leading p_T tracks in charge mis-identification events and the number of SMT and CFT hits associated to charge mis-identified tracks, it is shown in Figures 7.2 and 7.3. The distributions show that the charge mis-identification events in Monte Carlo are mainly due to fewer CFT hits that are associated to the track when it is traversing the central tracker in a $|\eta|$ region above 1.63.

It can be easily shown for events where one of the tracks is charge mis-identified, that whereas the invariant mass calculated using the true Monte Carlo information peaks at around 91 GeV/c^2, the invariant mass distribution calculated using reconstructed kinematic variables is distorted towards higher values. That can be understood from the fact that charge mis-identified tracks are typically assigned much higher transverse momenta than what the particle's transverse momentum it has been generated with.
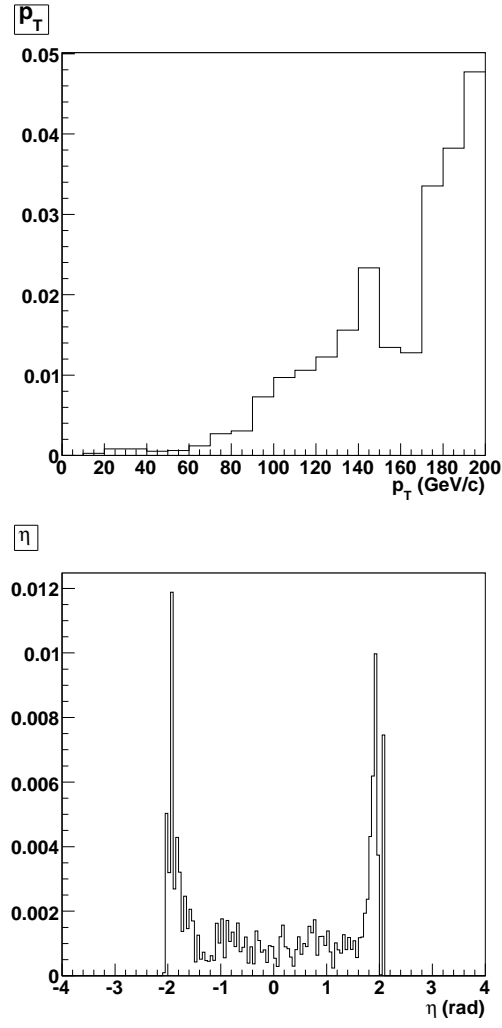
Figure 7.2: Charge flip rate for p_T (top) and η (bottom).
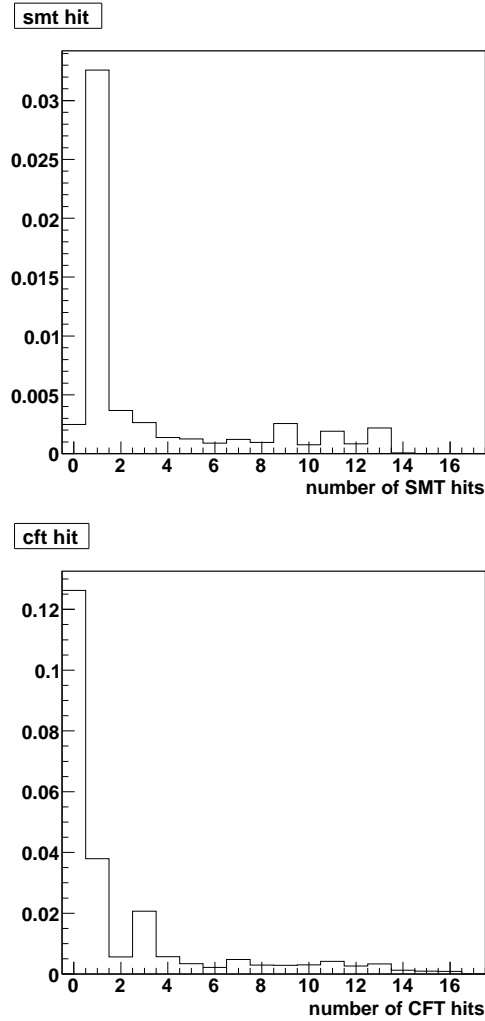
Figure 7.3: Charge flip rate for the number of SMT hits (top) and CFT hits (bottom).
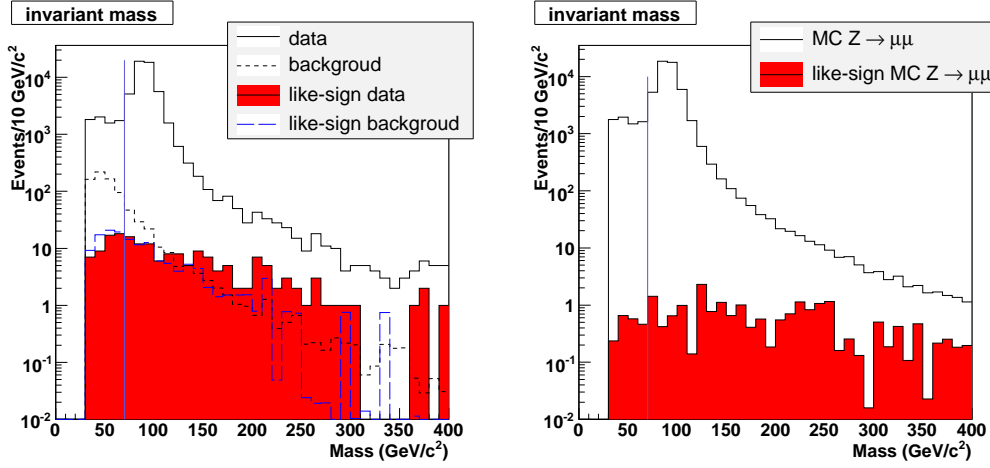
Figure 7.4: The di-muon invariant mass distribution for data and Monte Carlo Z→ μμ are shown respectively. The open histogram is drawn without like-sign requirement and the red histogram is drawn with like-sign requirement.

7.2 Calculation of the charge flip probability

Since the mis-identification of charge occurs mainly in Z→ μμ and the resulting mis-measured muon typically has high p_T, the di-muon invariant mass above 70GeV is used to measure the charge flip probability. This selection also reduces the most QCD background, since most QCD background are peaked in the low mass range. For the calculation of the charge flip rate, the preselection cut (S1) and the isolation cut (S2) are required. The charge mis-identification rate is obtained by dividing the number of events in the selection with like-sign requirement (S1,S2 and S4) by the number of events without like-sign requirement (S1 and S2) The charge flip rate is calculated for both data sample and $MC_{Z→μμ}$. In the case of the measurement in data, backgrounds are subtracted from the data sample. The background includes all MC backgrounds and QCD

contribution except $\mathrm{MC}_{Z\to\mu\mu}$.

The di-muon invariant mass distributions for like-sign and without like-sign requirement for data and MC are shown in Figure 7.4. The number of events above 70GeV the di-muon invariant mass are shown in Table 7.1.

$$\epsilon_{\mathrm{data}}^{\mathrm{flip}} = (\ 9.4\ \pm\ 1.3\ ) \times 10^{-4} \tag{7.1}$$

$$\epsilon_{\mathrm{MC}_{Z\to\mu\mu}}^{\mathrm{flip}} = (\ 3.9\ \pm\ 0.9\ ) \times 10^{-4} \tag{7.2}$$

The errors are statistical.

Since the charge flip rate in the Monte Carlo simulation is underestimated, the ratio of the rate $\epsilon_{\mathrm{data}}^{\mathrm{flip}}$ from data to the $\epsilon_{\mathrm{MC}_{Z\to\mu\mu}}^{\mathrm{flip}}$ from $\mathrm{M}_{Z\to\mu\mu}$ is considered as a correction. The ratio k_{flip} is defined as

$$k_{\mathrm{flip}} = \frac{\epsilon_{\mathrm{data}}^{\mathrm{flip}}}{\epsilon_{\mathrm{MC}_{Z\to\mu\mu}}^{\mathrm{flip}}} = 2.41\ \pm 0.67 \tag{7.3}$$

The ratio is applied only to the $Z \to \mu\mu$ MC sample when estimating the like-sign contribution.

Table 7.1: This table shows the numbers of data, backgrounds and $\mathrm{MC}_{\mathrm{Z}\to\mu\mu}$ events above 70 GeV the di-muon invariant mass for the charge flip rate calculation, where backgrounds exclude $\mathrm{MC}_{\mathrm{Z}\to\mu\mu}$. The first raw is corresponding to the events without like-sign requirement while the second raw to the events with like-sign requirement.

Selection	data	backgrounds	$\mathrm{MC}_{\mathrm{Z}\to\mu\mu}$
S1 and S2	51386	145	51196
S1, S2 and S4	127	79	19

7.3 Cosmic ray muon runs

To obtain the rate for charge mis-identification in the data, the usage of cosmic ray runs has been considered. Cosmic rays are an excellent tool for this kind of study, because the events are clean, all cosmic ray events must be opposite-charge (it follows from the CPT theorem) and there are many of them. The sample of cosmic ray muon is obtained by requiring timing cut and acolinearity cuts: $A = \pi - |\Delta\phi| + |\sum\theta - \pi|$ (see Section 4.4). The muons are also required to be isolated. The isolation requirement is the same as the requirement defined in Section 4.3. For simplicity, the ratio of the number of opposite-sign muons (21194 events) to the number of like-sign muons (771 events) is considered as the charge flip rate for cosmic ray muon. The range of $30 < M < 400$ GeV is considered. The charge flip rate of cosmic ray muon is determined to be 3.6×10^{-2}. This is much larger than the flip rate from $Z \to \mu\mu$. It could be explained from the fact that cosmic ray muons tend to have higher transverse
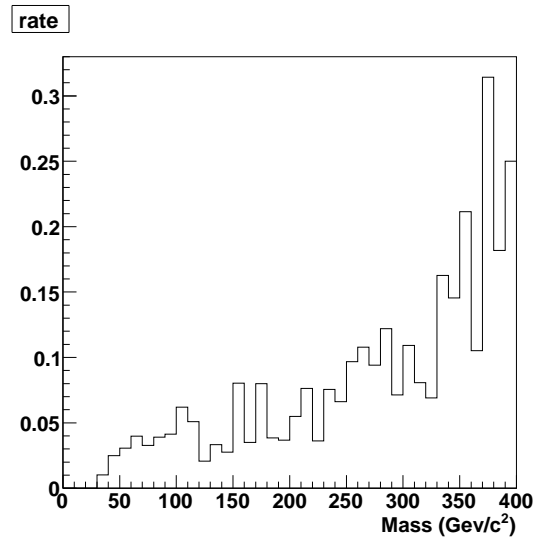
Figure 7.5: The flip rate for the di-muon invariant mass of cosmic ray.

momentum which cause the muon to be mis-identified easily. The charge flip rate for the di-muon invariant mass of cosmic ray is shown in Figure 7.5.

Chapter 8

Comparison of data and Monte Carlo

In this chapter the normalization of Monte Carlo to the data, comment on their agreement after each cut applied in this analysis, will be described. The agreement in terms of the invariant mass, acolinearity, leading muon p_T and second muon p_T will be demonstrated. Since the third muon is required the distribution of the third muon p_T will be shown as well. This is an important piece of the analysis. In any search analysis, one has to demonstrate the understanding of backgrounds. One has to show not only that all relevant backgrounds are taken into account; none of them is missing or underestimated, but also the adequate understanding of all cuts has to be demonstrated. Both aspects can be understood from a cut flow tables for all di-muon combinations (Table 8.1) and like-sign di-muon combinations (Table 8.2). Any inadequate description of the data with Monte Carlo shows up in the cut flow table as a discrepancy between the number of events expected for a given simulated physics background sample, and/or the sum of background samples, and the number of

events measured in the data. It can be obvious from the difference in number of events after each cut, or, in contrary, after one of the cuts only. Therefore, one has to decide, whether a missing contribution to the background, the physics nature of the generated Monte Carlo sample, some detector related issue or the normalization are to be blamed.

8.1   Normalization of Monte Carlo to data

Normalized number of events $N_{S\{i\}}^{norm}$ remaining in each sample after every selection $S\{i\}$, where $i = 1, \ldots, 5$, is normalized to the data as follows

$$N_{S\{i\}}^{norm} = \frac{N_{expected}}{N_{generated}} \times N_{S\{i\}}. \tag{8.1}$$

In this formula, $N_{expected} = \sigma \times \int L_{effective}$ is the total number of expected events given the integrated luminosity of the data sample and the cross section of the sample; $N_{generated}$ is the total number of simulated events in Monte Carlo sample and $N_{S\{i\}}$ is the total number of events that pass a given selection $S\{i\}, i = 1, \ldots, 5$. The number of expected Monte Carlo events is based on the NNLO (NLO if signal) cross sections for all processes given in Table 5.2. The effective integrated luminosity is obtained by using Z peak. The Z peak range is considered as 60–130 GeV for both data and MC $Z \rightarrow \mu\mu$. The effective integrated luminosity is defined as

$$\mathcal{L}_{eff} = \frac{N_{data}^{S1\&S2}}{\sigma(Z \rightarrow \mu\mu) \times B} \times \frac{N_{Z\rightarrow\mu\mu}^{gen}}{N_{Z\rightarrow\mu\mu}^{S1\&S2}} \tag{8.2}$$

where $N_{data}^{S1\&S2}$ is the number of data events in the invariant mass plot within the interval 60–130 GeV after the preselection (S1) and the isolation requirement (S2). $N_{Z\rightarrow\mu\mu}^{S1\&S2}$ is the same just for MC $Z \rightarrow \mu\mu$. $N_{Z\rightarrow\mu\mu}^{gen}$ is the number of the

generated MC $Z \rightarrow \mu\mu$ in the range 60–130 GeV. $\sigma(Z \rightarrow \mu\mu) \times B$ is the cross section times branching ratio. The $\sigma \times B$ of 242 pb^{-1} is used (see Table 5.2).

This formula can be read the following way: $\frac{N_{\text{data}}^{S1\&S2}}{\sigma(Z \rightarrow \mu\mu) \times B}$ would give the luminosity if the detector would be 100% efficient. Since the efficiency is not 100% at all, it should be corrected by the Detector acceptance. The acceptance would be $\frac{N_{Z \rightarrow \mu\mu}^{S1\&S2}}{N_{Z \rightarrow \mu\mu}^{gen}}$. The first term need to be divided by this acceptance which lead to the formula quoted above.

The number $\mathcal{L}_{eff}$ is used for the normalization for all MC.

The number of remaining events after each cut are shown in Table 8.1. The distributions of the di-muon invariant mass, $\Delta\phi$ between two muons, leading p_T and second p_T are shown in Figure 8.1–8.7. In the events with more than one pair of muons that fulfills each of selections, the invariant mass and $\Delta\phi$ between two muons are calculated only for the pair which has the muons with highest transverse momentum. There is a good agreement between data and the Monte Carlo simulation plus QCD, both for the normalization and for the shape of the di-muon invariant mass and the $\Delta\phi$ distributions after each selection.

The third muon does not have any requirements on the number of SMT and CFT hits. However, if the third muon fulfills the CFT and SMT hit cuts in S1, then it is considered as a candidate muon in construction of a di-muon invariant mass. The p_T distribution for the third muon is shown in Figure 8.8. The data agrees well with the simulated backgrounds plus QCD.

discrepancy

In the di-muon invariant mass distribution there is a discrepancy above 200 GeV. This discrepancy appears to be a bump in the range 200-240 GeV and 260-300 GeV. One possible explanation is that this discrepancy is from mis-identified muons of Z and cosmic ray. Although cosmic veto using timing cut is applied in this analysis, that could not reject all cosmic muons. The charge flip rate of cosmic ray muons is large (see Figure 7.3). The muons from Z decay turned out to be the main source that caused this discrepancy. The leading p_T muon from Z decay tends to be mis-identified. From the fact that charge mis-identified tracks are typically assigned much higher transverse momenta than what the particle's transverse momentum it has been generated with, the leading p_T muons shift to high momentum area. It results in high missing transverse energy in the opposite direction. Figure 8.9 shows that the direction of leading muon is opposite to the missing E_T. Therefore the discrepancy could be explained by the mis-identified muon. The bump happened to appear in this high mass range above 200GeV due to lack of statistics.

8.2   Like-sign background

The idea is to construct a set of selection criteria, or 'cuts', which should preferentially select the doubly-charged Higgs boson signal over the background processes. Any statistically significant excess could be evidence for a doubly-charged Higgs boson signal.

When the muons are required to be of like-sign charge most of the background from Z $\rightarrow \mu\mu$ are removed. Since the isolation requirement is not applied at this selection level (S1/S4) the most of the background in Figure 8.5 is from QCD contribution. The invariant mass for like-sign dimuons and their

Table 8.1: Expected number of Monte Carlo background and QCD events and number of observed events after each selection cut. The simulation of Z decays includes the Drell-Yan contribution. Only statistical uncertainties are given in the Table.

Selection	Preselection	Isolation	$\Delta\phi < 2.5$	Like sign	Third muon
	S1	S2	S3	S4	S5
Signal (140 GeV)	20.7	18.7	16.4	11.8	10.2
$Z \to \mu\mu$	69236	58325	4942	9.2	0.5±0.4
QCD	5244	423	40.5	14.2	0.5±0.2
$Z \to \tau\tau$	328	269	20.0	< 0.01	< 0.01
$t\bar{t}$	38	20	14	0.03	<0 .01
WW	40	34	20	< 0.01	< 0.01
WZ	19	16	11	3.0	1.6±0.03
ZZ	11	9	5	0.6	0.5±0.01
Total background	74917±123	59096±111	5052±33	27±1.7	3.1±0.5
Data	74086	59347	4623	35	3
$S/\sqrt{S+B}$	0.08	0.08	0.23	1.89	2.79

$\Delta\phi$ distributions in the data and Monte Carlo are shown in Figure 8.5–8.6. The number of remaining events after each cut with like-sign requirement are shown in Table 8.2.

Table 8.2: Expected number of Monte Carlo backgrounds and QCD and number of observed events after each selection cut with like-sign requirement.

Selection (Like-sign)	Preselection S4 & S1	Isolation S2	$\Delta\phi < 2.5$ S3
Signal (140 GeV)	16.6	13.5	11.8
$Z \to \mu\mu$	115	59	9.2±1
QCD	1897	153	14.2±1
$Z \to \tau\tau$	3	0.2	0 < 0.01
$t\bar{t}$	7	0.04	0.03±0.01
WW	0.08	0.04	< 0.01
WZ	5.2	4.3	3.0±0.04
ZZ	1.1	0.9	0.6±0.02
Total background	2028	217	27±1.7
Data	1966	187	35

8.3   Normalization of signal sample

In the figures (Figure 8.1–8.7) the distribution of a left-handed doubly-charged Higgs signal with a mass $M(\mathrm{H}^{\pm\pm}) = 140$ GeV are shown, with the normalization given by the NLO cross section, taking into account the experimental efficiencies. The number of expected signal events after each selection is shown

in Table 8.3 for different masses. Total signal efficiencies lie in the range30%-35%, and they are nearly independent of mass.

The trigger efficiency in signal samples is assumed to be flat and close to 100% in transverse momentum, i.e. no trigger turn-on dependence is taken into account. There are two reasons for this assumption:

- there are 3 muons reconstructed on average in the signal sample. It means that the trigger efficiency must be very high. It will therefore depend much less on the pT of reconstructed muons.

- transverse momentum of reconstructed muons is as hard, or as a matter of fact, even harder than the one of muons that come from Z decays. One should keep in mind that $H^{\pm\pm}$ bosons are typically Lorentz boosted. This is why pT of muons from $H^{\pm\pm}$ boson decays is higher.

Muons from doubly-charged Higgs decays are boosted. This is why the mean of the $\Delta\phi$ distribution is at around 1.7–2.0 for Higgs masses below 200 GeV/c^2. The average muon multiplicity of signal events is 3. This is also a reason why the acolinearity selection (S3) does not alter signal efficiency too much (Table 8.3, selections (S3) and (S4)).

Figure 8.1: Distribution of the di-muon invariant mass, $\Delta\phi$ between the two muons, leading p_T and second p_T for data compared to the sum of Monte Carlo backgrounds and QCD after the preselection (S1). The signal expected for a left-handed $H^{\pm\pm}$, with $M(H^{\pm\pm}) = 140$ GeV/c^2, is also shown by the open histogram.
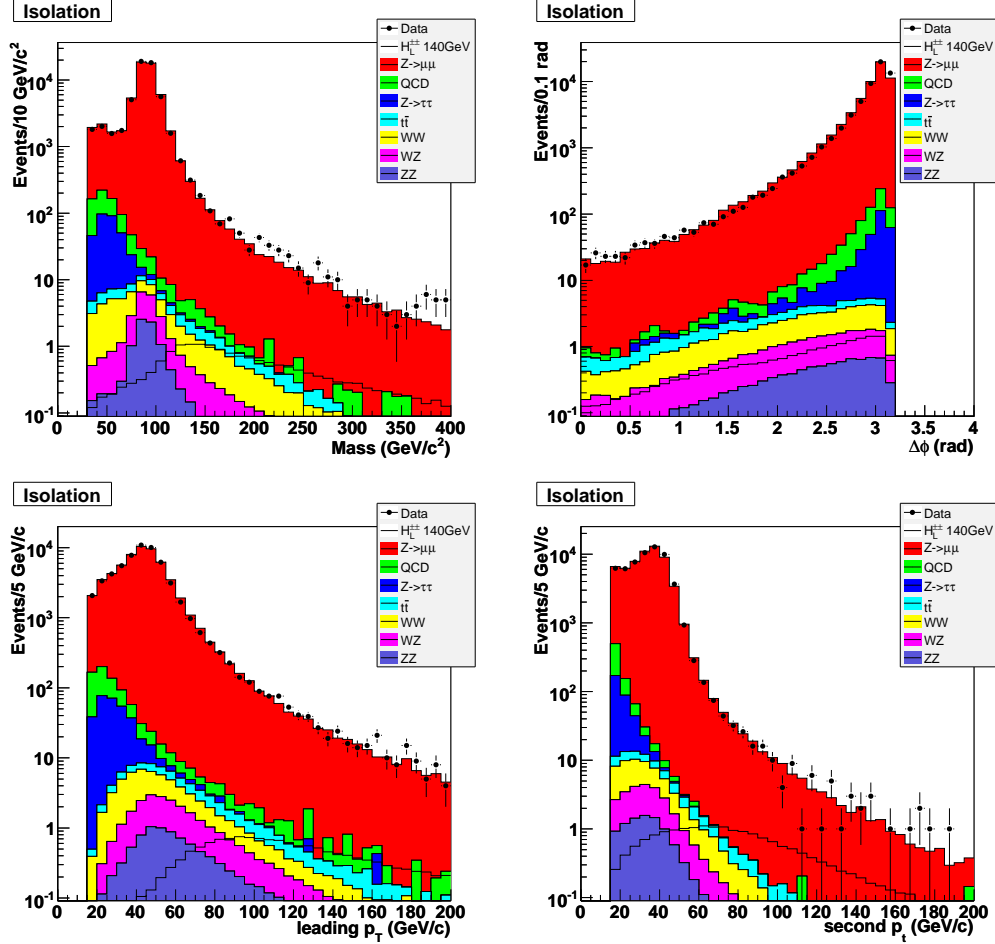
Figure 8.2: Distribution of the di-muon invariant mass, $\Delta\phi$ between the two muons, leading p_T and second p_T for data compared to the sum of Monte Carlo backgrounds and QCD after the isolation requirement (S1-S2). The signal expected for a left-handed $H^{\pm\pm}$, with $M(H^{\pm\pm}) = 140$ GeV/c^2, is also shown by the open histogram.
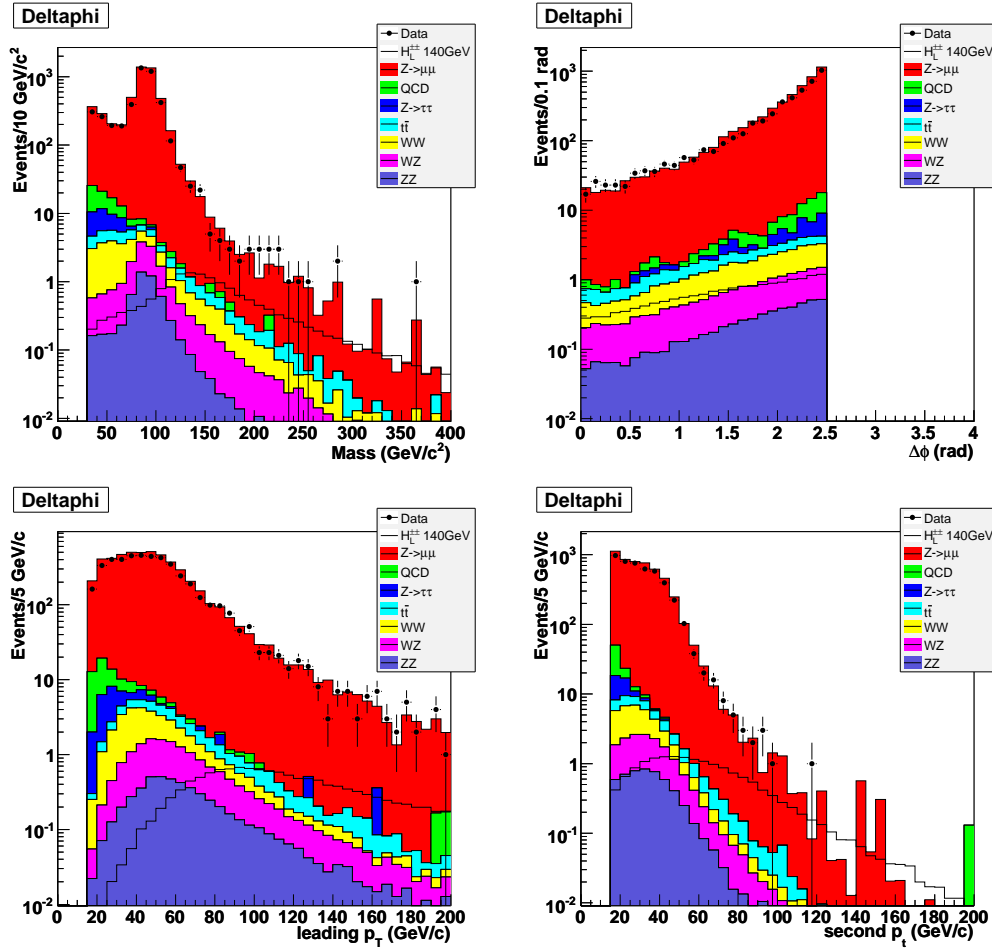
Figure 8.3: Distribution of the di-muon invariant mass, $\Delta\phi$ between the two muons, leading p_T and second p_T for data compared to the sum of Monte Carlo backgrounds and QCD after the $\Delta\phi$ requirement (S1-S3). The signal expected for a left-handed $H^{\pm\pm}$, with $M(H^{\pm\pm}) = 140$ GeV/c², is also shown by the open histogram.
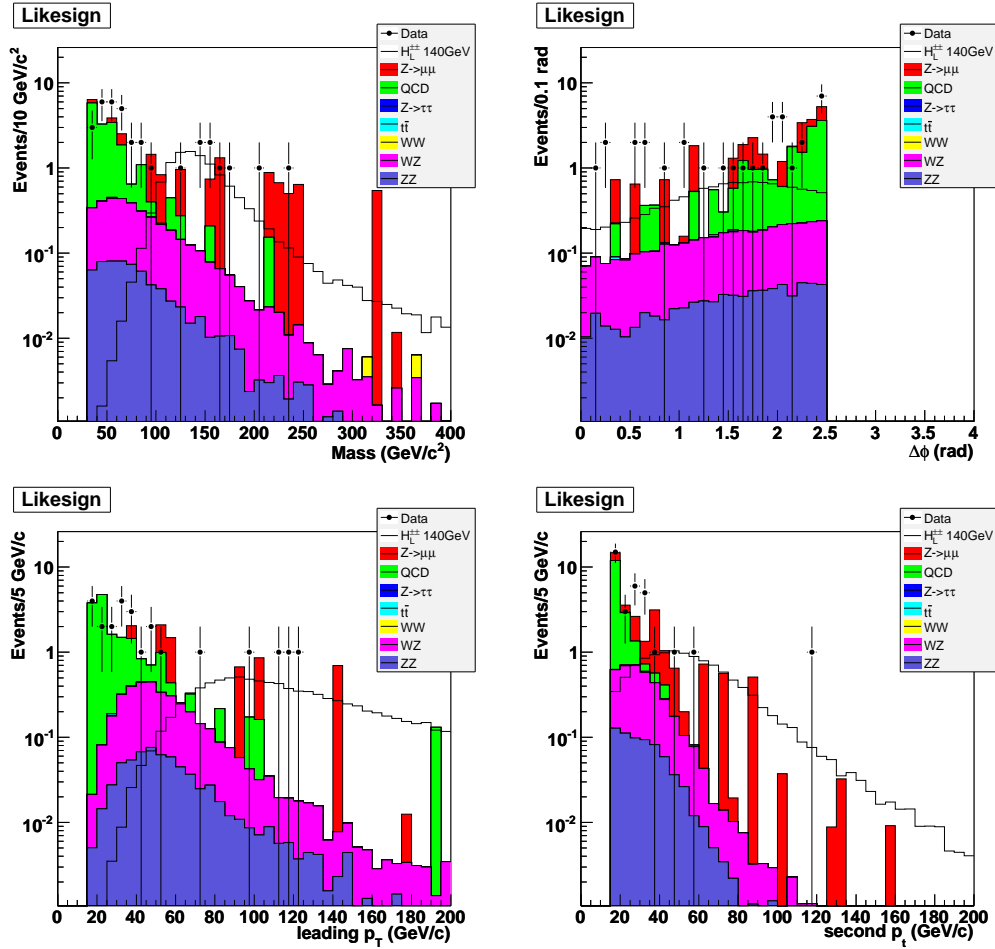
Figure 8.4: Distribution of the di-muon invariant mass, $\Delta\phi$ between the two muons, leading p_T and second p_T for data compared to the sum of Monte Carlo backgrounds and QCD after the like-sign requirement (S1-S4). The signal expected for a left-handed $H^{\pm\pm}$, with $M(H^{\pm\pm}) = 140$ GeV/c^2, is also shown by the open histogram.
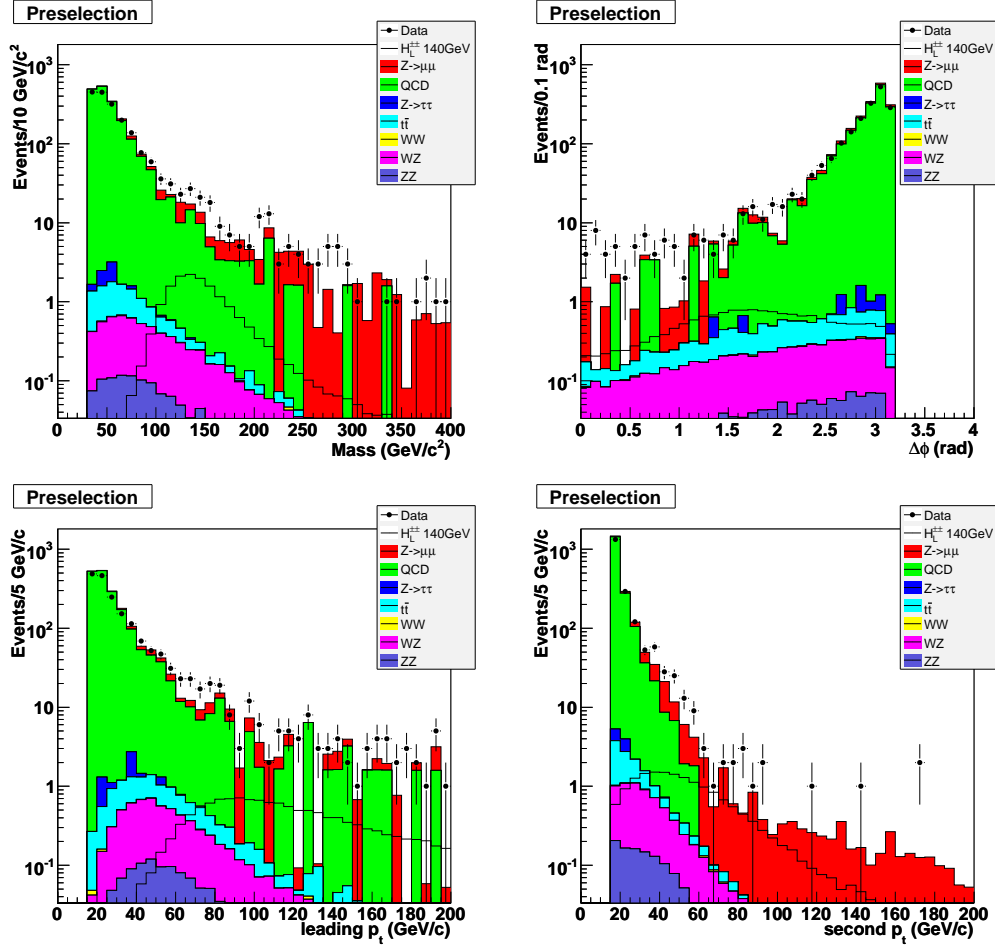
Figure 8.5: Distribution of the di-muon invariant mass, $\Delta\phi$ between the two muons, leading p_T and second p_T for data compared to the sum of Monte Carlo backgrounds and QCD after the preselection (S1) with the like-sign requirement (S4). The signal expected for a left-handed $H^{\pm\pm}$, with $M(H^{\pm\pm})$ = 140 GeV/c^2, is also shown by the open histogram.
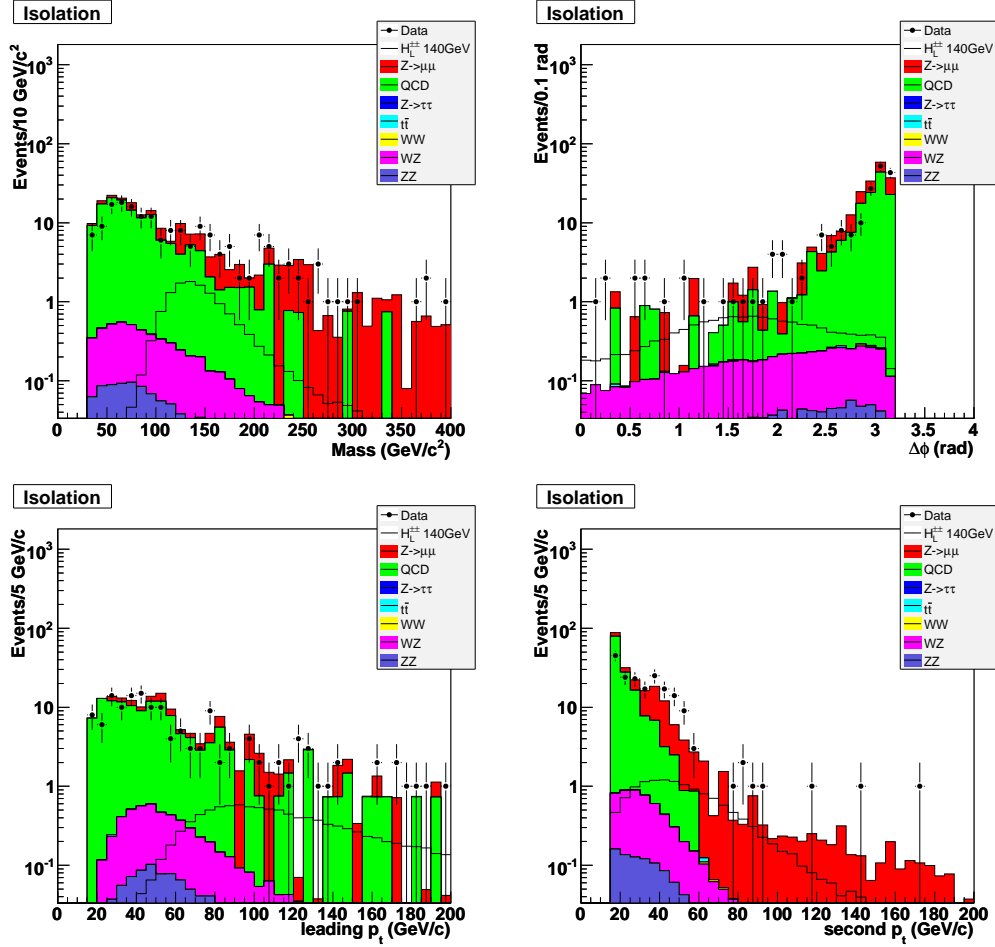
Figure 8.6: Distribution of the di-muon invariant mass, $\Delta\phi$ between the two muons, leading p_T and second p_T for data compared to the sum of Monte Carlo backgrounds and QCD after the isolation (S1-S2) with the like-sign requirement (S4). The signal expected for a left-handed $\mathrm{H}^{\pm\pm}$, with $M(\mathrm{H}^{\pm\pm})$ = 140 GeV/c^2, is also shown by the open histogram.
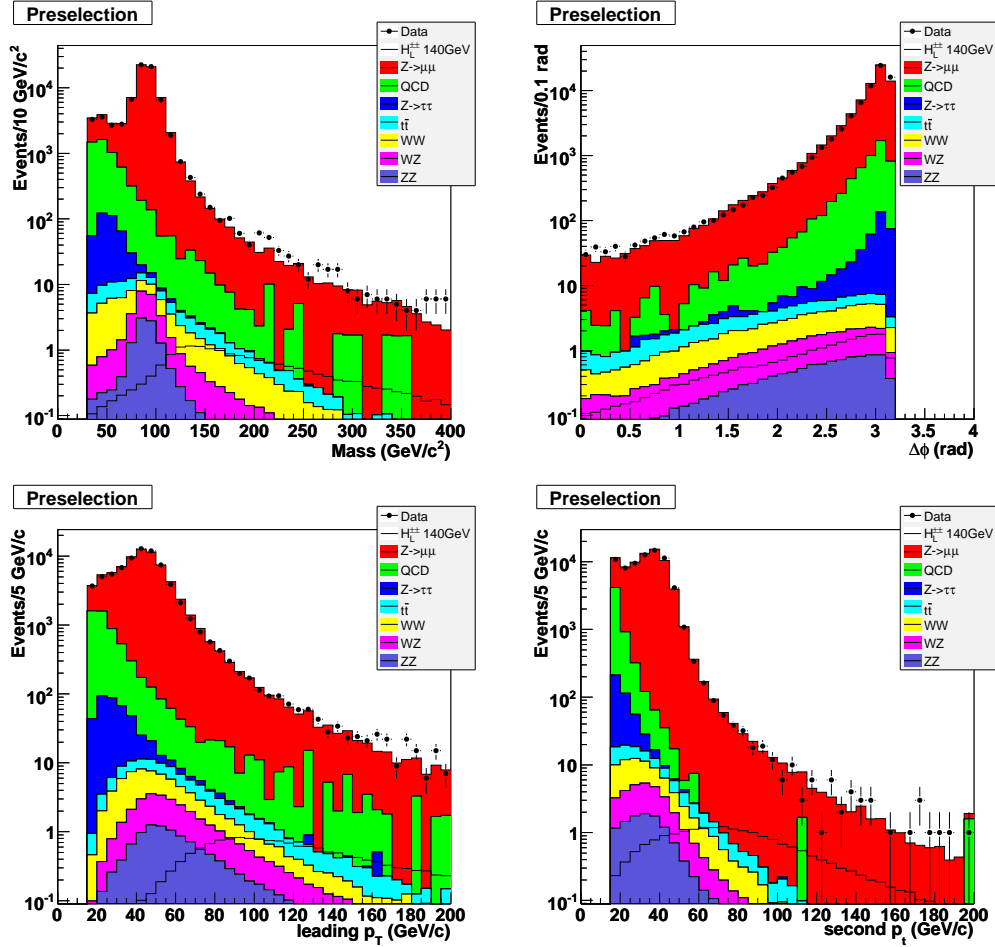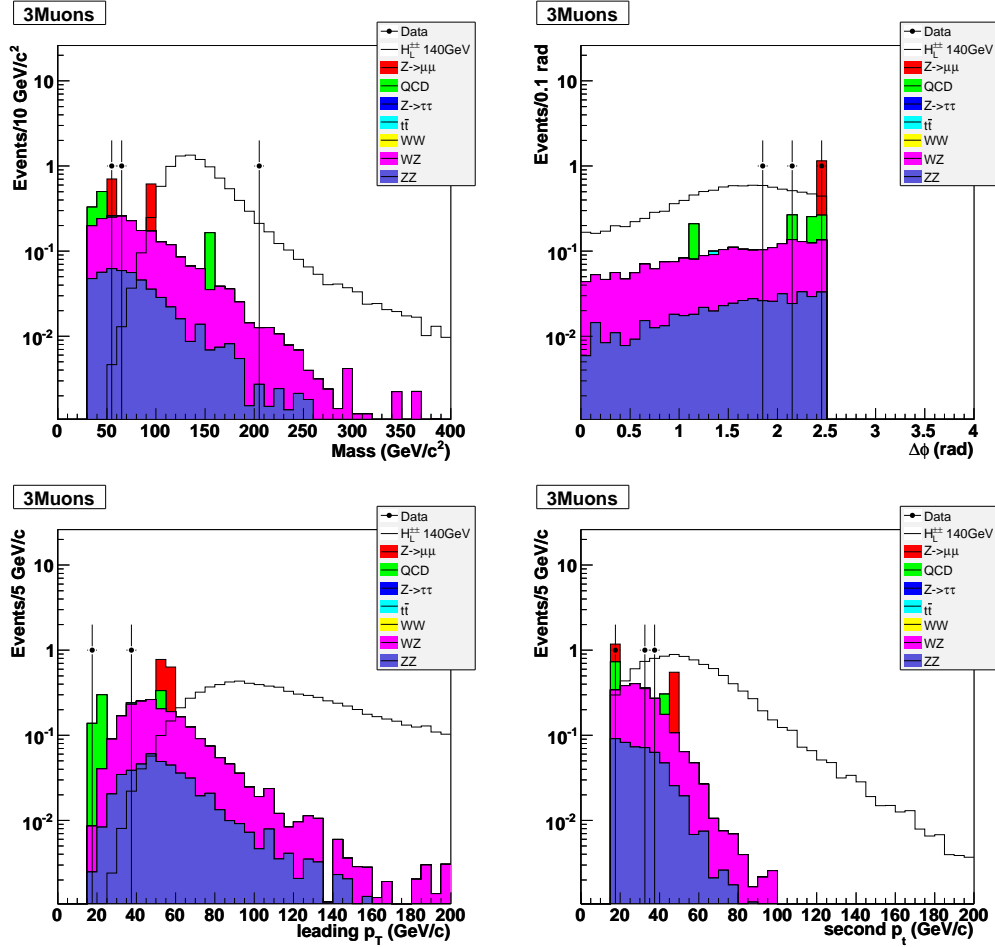
Figure 8.7: Distribution of the di-muon invariant mass, $\Delta\phi$ between the two muons, leading p_T and second p_T for data compared to the sum of Monte Carlo backgrounds and QCD after the third muon requirement (S1-S5). The signal expected for a left-handed $H^{\pm\pm}$, with $M(H^{\pm\pm}) = 140$ GeV/c², is also shown by the open histogram.

M (GeV)	100	120	140	160	180	200
$N = \sigma L$	126.7	59.2	29.7	15.7	8.5	4.8
S1	86.3	40.1	20.5	10.8	5.7	3.2
S2	77.6	36.1	18.5	9.7	5.1	2.9
S3	66.2	31.4	16.3	8.7	4.6	2.6
S4	49.0	22.8	11.7	6.1	3.2	1.8
S5	41.7	19.7	10.1	5.3	2.8	1.5
$\epsilon(\pm 1\%)$	33%	33%	34%	34%	33%	32%

Table 8.3: Number of expected signal events after each cut and efficiency for each mass point. The first row gives the number of expected events using the NLO cross section for left-handed $H^{\pm\pm}$ boson. The simulation is done in 10 GeV mass steps, but only every second mass point from 100 GeV is shown.
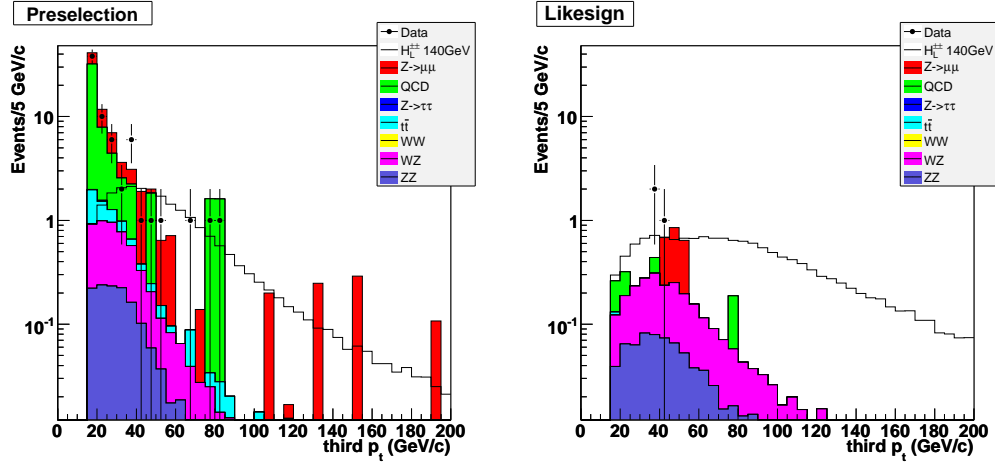
Figure 8.8: Distribution of the third transverse momentum p_T for data compared to the sum of Monte Carlo backgrounds and QCD. Preselection (S1) and like-sign (S4) were required respectively. The signal expected for a left-handed $H^{\pm\pm}$, with $M(H^{\pm\pm}) = 140$ GeV/c², is also shown by the open histogram.
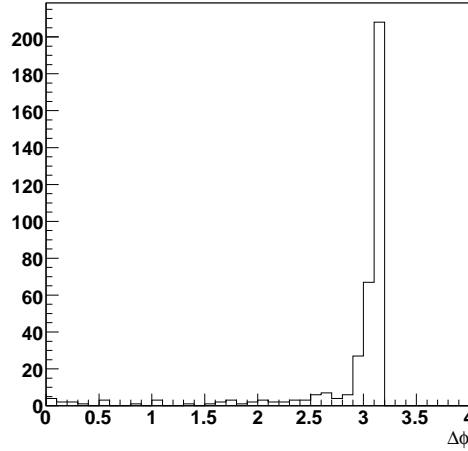

Figure 8.9: The direction of leading muon is opposite to the missing E_T.

Chapter 9

Cut optimization

In this chapter it will be shown how cut optimization has been performed. It is easy to apply cuts that reduce the amount of backgrounds practically to zero, but they might also represent an efficiency hit, i.e. reduce the signal sensitivity on the other hand. That has to be avoided at any cost. The cut optimization therefore is to develop a set of selections that allow to reduce the Standard Model backgrounds significantly but at the same time do not change the signal efficiency too much.

It is important to emphasize that any cut optimization should be performed 'blindly'. It means that one should never look on the candidate events and optimize selection criteria so that some of them are removed. It has to be done vice versa, looking at $S/\sqrt{S+B}$ ratio optimize the cuts, for instance, and just then check whether the set of candidate events remains the same, or went through some changes.

Some selections such as preselection and like-sign cut can barely be changed or modified, but since the third muon cut is required, there are cuts that need to be optimized in order to improve the signal sensitivity and keep the level

of backgrounds low at the same time. This is a purpose of the study that is presented in this chapter.

The cut optimization is a very sensitivity study, it can be also easily understood that there is a need for a long-term stability of the analysis in new particle searches. The reason for that is that it is a poor practice if cuts are change too dramatically from one iteration of the analysis to another. It immediately raises a question whether the selections are not suited to achieve higher limits too conveniently. The best way is to decide for a set of rather conservative, however needed and easily to be justified selections, and keep them unchanged for a long time. Indeed, the cut optimization is a must. Of course, later, when there is more statistics(luminosity), the cut optimization might be re-visited and newer values applied, it should not change the results significantly however.

And that is what has exactly been done in this analysis.

9.1   Preselection cut

This selection requires at least two medium muons, both with a matched central track, where each of the selected tracks has a transverse momentum greater than 15 GeV/c. The selected central track is required to have at least 2 SMT hists and more than 5 CFT hits. It is required that the invariant mass reconstructed in an event is above 30 GeV/c^2.

Practically, the only candidates for a possible cut optimization are (a) the quality of muon, (b) the requirement on transverse momenta of central tracks matched to a muon, and (c) the quality requirement on the number of SMT and CFT hits associated with a central track.

When the quality of muon is required to be loose, the remaining number of data and signal events after final cut are 15 events and 12.5 events, respectively. The number of data events increased by 5 times while the number of signal events increased by 1.2 times (see Table 8.1). This simple calculation shows that requiring a loose quality of muon deteriorates the sensitivity. There are also indications that loose muons suffer from higher background and fake rates [99].

It is a good idea to place the p_T cut as low as possible, however there is no need to require muons with p_T less than 10 – 12 GeV/c, because the focus of this analysis is on high-p_T isolated muons, muons that have a harder transverse momentum spectrum than those observed in $Z \rightarrow \mu\mu$ events. A region above the Z mass peak is an interval of interest in this analysis. This is why any lowering of the transverse momentum requirement is actually contra-productive.

The same can be said about the quality criteria on tracks matched to muons. This criteria is very weak, in order to calculate the invariant mass of a high-mass dimuon system, a precise measurement of the transverse momentum is needed. It is essential to have good track, i.e. tracks with as many hits as possible, because this is is where the momentum measurement and its precision comes from. Even for high-p_T track, it is important to have a measurement in the silicon tracker, as a matter of fact, it is even more important for very high-p_T tracks because in order to do a good measurement, as large as possible between the measurement closet to the beam pipe and the further-most measurement is needed. In earlier days, the analysis was performed without this requirement, but this cut was soon introduced because axial tracks matched to muons started to be a problem. The transverse momentum measurement for

axial only tracks is poor, many events with high invariant masses have been therefore selected. What was common for them was that they all contained axial only tracks (at least one track per event). The muon which has poor track tend to have high probability of flipping charge as the track has less hits as well. In this sense, it actually might be a good idea to tighten the selection a little bit, meaning to require more hits. On the other hand, it might not be such a good idea because of the hit to the signal efficiency that is affected by the cut. It is well known that an existing Monte Carlo does not describe the data all too well in terms of number of hits associated to tracks. In alternative language, the same requirement on number of hits on the track is much harder in Monte Carlo than in data. One has to be cautious about it. To conclude, introduction of 2 SMT hits and 5 CFT hits on the track quality seems to be the optimal way [100], and that is the approach taken in this analysis.

9.2   Isolation cut

The definition of an isolated muon is given in Section 4.3. The definition of the isolation cut is not questioned in this study, the optimization was performed in[101]. However, it is possible to optimize the way isolation requirement has been applied. In this analysis this optimization is not implemented. The way isolation chosen is like following. The two muons that enter to the calculation of an invariant mass and acolinearity must be isolated.

9.3   Acolinearity cut

The $\Delta\phi$ cut is applied to remove back-to-back $Z \rightarrow \mu\mu$ and some of the remaining muons from the semi-leptonic decays of b quarks in jets that were not removed by the isolation requirement. In this analysis the decision has been made to apply it at 2.5.

The acolinearity cut optimization has been performed with following three cases.

(a) **Dropping the cut entirely**

This optimization arises from the fact that I required third muons as a final cut. Since at least one pair out of three muons can have dphi ¡ 2.5, this cut seemed to be doing nothing. But one should be aware of the third muon quality that has no SMT hit and CFT hit requirement (see the definition of the third muon in Chapter 4).

(b) **Applying the cut to two muons**

The two muons should passe the preselection (S1) and the isolation requirement (S2), If there are the third muon which has good quality track of two SMT hits and five CFT hits, the event will be selected since at least one pair has $\Delta\phi < 2.5$.

(c) **Applying the cut to all muons**

The event if neither of any muon pairs has $\Delta\phi > 2.5$ is selected. In addition to the two muons that pass S1 and S2, other good muons are considered so that all muon pair has $\Delta\phi < 2.5$. So if any one pair with $\Delta\phi > 2.5$ exists, the event is not selected.

Table 9.1 shows the number of events after the final selection (S5) in backgrounds and signal ($M_{H^{\pm\pm}} = 140$ GeV/c^2). In the case (a), the number of $Z \to \mu\mu$ is about two times larger than the case (b). The contribution of QCD increased by a factor of 6 compared to the case (b). The number of dibosons increased by a factor of 1.5. The number of total background increased by a factor of 2.3 while the number of signal increased by a factor of 1.1. This increasing can be understand from the fact that most of $Z \to \mu\mu$ and QCD are back-to-back. The difference between the number of events in (a) and the number of events (b) can be also explained by the ratio of how many third muons fulfilled the SMT and CFT hit requirement. The ratio of how many third muons fulfilled the SMT and CFT hit requirement is found to be less than 0.01% for both $Z \to \mu\mu$ and QCD. Requiring the third muon, therefore, does not mean that the acolinearity cut is not satisfied automatically.

The best results are achieved using definition (b) applying the cut to two muons. Definition (b) has been finally applied in this analysis.

9.4 Like-sign cut

What the final state is two like-sign muons with additional third muon. Even though dropping like-sign cut is considerable, it would cause $Z \to \mu\mu$ to remain to the end of the final selection. Dropping like-sign cut, therefore, is not feasible.

Selection	(a)	(b)	(c)
$Z \to \mu\mu$	1.3	0.5	< 0.01
QCD	2.8	0.5	0.5
WZ	2.3	1.6	0.58
ZZ	0.64	0.5	0.13
Total background	7	3.1	1.23
Signal	11	10.2	2.47
$S/\sqrt{S+B}$	2.59	2.79	1.29

Table 9.1: Number of background and signal events after final cut for each backgrounds with (a) dropping $\Delta\phi$ cut , (b) applying the cut to the two muons that passed S1 and S2 and (c) applying the cut to all muon pairs. The sensitivity is given in last row. Th events from $Z \to \tau\tau$, $t\bar{t}$ and WW are found to be nothing remained after final cut for all three conditions.

9.5   Third muon cut

Any analysis for the doubly-charged Higgs boson, H$^{\pm\pm}$, has not yet been performed with the third muon requirement. The definition of the third muon need to be studied to get the best result. This analysis has looked up two cases. The first case is that the third muon has no requirement of having 2 SMT hits and 5 CFT hits while the second case has such hit requirements.

If the muon has reconstructed badly without satisfying hit requirement, the probability of flip charge is going up. That leads to bad di-muon invariant mass construction. That's the reason why this badly reconstructed third muon has not been considered for muon selection. Table 9.2 shows the sensitivity for

two cases.

M (GeV)	(a)	(b)
Signal (140GeV)	10.2	9.4
$Z \rightarrow \mu\mu$	0.5	0.5
QCD	0.5	0.3
di-bosons	2.1	2.0
Total background	3.1	2.8
$S/\sqrt{S+B}$	2.79	2.70

Table 9.2: Number of background and signal events after final cut for each backgrounds with (a) the third muon which is not required to have good quality track cut (b) the third muon which is required to have good quality track cut.

The quality of the third muon corresponds to signal efficiency. This requirement reduced the signal efficiency by 86%. That requirement enhanced sensitivity.

Chapter 10

Candidate events

This chapter will present the remaining events which pass the preselection, isolation, acolinearity, same-charge cuts and third muon cut. Each event is identified by a run and event number. The kinematic parameters of all doubly-charged Higgs boson candidate events will be shown. The di-muon invariant mass is calculated using the kinematic properties of the muon pair that pass the selection criteria (Section 4.3). All analysis and muon selection criteria have been discussed in Section 4.3.

10.1 Candidate details

Three events remain in the data after all selections. The run and event numbers as well as the invariant mass combinations among all muons in these events are given in the Table 10.1 and the kinematic properties of the individual muons in Table 10.2.

The largest remaining background after the third muon requirement is WZ background with 1.6 events. The contribution from Z$\to \mu\mu$ is 0.5 events. The

	Run	Event	$M(\mu_1\mu_2)$	$M(\mu_1\mu_3)$	$M(\mu_2\mu_3)$	Missing E_T
(1)	175666	1137583	260.353(−+)	205.602(−−)	144.15(+−)	138.20 GeV
(2)	203564	14775029	103.199(+−)	86.3628(+−)	67.1431(−−)	10.52 GeV
(3)	205114	3409480	124.463(+−)	24.6714(+−)	50.4876(−−)	43.72 GeV

Table 10.1: Run, event number and the invariant masses of the three possible pairings of selected muons for the candidate events. Muons are numbered in the highest p_T order. The charges of the muons are given in parentheses.

expected QCD contribution is 0.5 events.

10.2 Interpretation of candidate events

This section suggests a possible explanation of the candidate event nature. The explanation is based on information listed in Table 10.1 and Table 10.2.

Event (1) has two negatively charged muons and one positively charged muon. The missing transverse energy in the event is very large, approximately 140 GeV/c^2 with correcting for muon transverse momentum. Table 10.1 gives calculated invariant masses for all di-muon permutations in this event. All three di-muon combinations are far away from the Z boson mass. All three muons are tight and isolated. The transverse momentum of the first muon is about 241 GeV/c, that seems to be a little bit too high. Not many tracks are reconstructed with such a high transverse momentum, thus some kind of mis-reconstruction is possible. The second muon has no SMT hits. Even though all three di-muon combinations are far away from the Z boson mass the ex-

Muon	Charge	p_T(GeV)	η	ϕ	N_{SMT}	N_{CFT}	Quality
Event(1) Run 175666 event 1137583
μ_1	-1	241.0	0.07	2.11	8	16	tight
μ_2	$+1$	40.0	-1.52	5.30	0	16	tight
μ_3	-1	31.9	1.37	4.59	3	16	tight
Event(2) Run 203564 event 14775029
μ_1	$+1$	40.3	0.23	2.16	4	16	tight
μ_2	-1	39.7	-1.51	4.45	8	16	tight
μ_3	-1	35.7	-1.38	0.35	8	14	tight
Event(3) Run 205114 event 3409480
μ_1	$+1$	36.9	-1.54	1.77	10	15	tight
μ_2	-1	17.2	1.61	5.99	8	15	tight
μ_3	-1	15.5	-0.57	1.55	8	16	tight

Table 10.2: Transverse momentum p_T, charge, pseudorapidity η, azimuthal angle ϕ and number of SMT and CFT hits for all muons in the candidate events. Event(2) contains another not selected tight muon which has momentum of 12.3 GeV.

planation of this event by mis-identified reconstruction can not be ruled out. The reason is that transverse momentum of the mid-identified muon tends to be random. This event is therefore consistent with being a WZ event.

Event (2) has two negatively charged muons and one positively charged muon. All three muons have transverse momenta well above 15 GeV/c. This event also contains a fourth muon that matches to a low p_T central track. The fourth muon is not considered in this analysis. All muons are tight and isolated. No significant missing transverse energy is observed. There is at least one Z candidate in this event. The second candidate event seems to be consistent with being a ZZ event.

Event (3) has two negatively charged muons and one positively charged muon. All three muons have transverse momenta above 15 GeV/c. This event has a muon which has $\eta > 1.6$. This could be the case of flipping charge from $Z \to \mu\mu$+jets.

Chapter 11

Limit setting

In the absence of excess above background, the final step is to take the Monte Carlo samples generated, the data and set the mass limit on doubly-charged Higgs boson mass. This chapter presents the procedure for computing approximate confidence levels for searches for new particles where the expected signal and background levels are small enough to require the use of Poisson statistics. The limit calculation are performed using TLimit which has been adapted from the programs MCLIMIT [103]. This program is based on Modified Frequentist approach (The CL_S method). It was used by the CERN LEP Higgs working group.

11.1 Confidence Level computation for searches with small statistics

The interpretation of results of searches for new particles and phenomena near the sensitivity limit of an experiment is a common problem in particle physics. The confidence level computation for searches with small statistics are de-

scribed in detail in [103] and [104]. The loss of sensitivity may be due to a combination of small signal rates, the presence of background comparable to the expected signal, and the loss of discrimination between models due to insufficient experimental resolution. The search for Higgs bosons at LEP was such an experiment.

Frequently, the signals are marginal, and it is therefore more convincing if several channels are combined. That improves the confidence level (CL) significantly, especially if the sensitivity is limited by the collected luminosity and not by the kinematic boundaries.

The method is based on binning the search results (invariant mass, acolinearity etc.) in their discriminant variables and treating each bin as a statistically independent counting search. This uniform representation is then easy to be combined. As it can be seen later in this chapter, this is a strong statement with profound consequences.

11.2   Modified Frequentist Approach Confidence Levels

In this analysis we set the limit at 95% confidence level (CL). Assuming two hypothesis 'signal+background' and 'background', the experiment should be able to distinguish between them. The 'signal+background' hypothesis is excluded at 95% if supposedly the 'signal+background' hypothesis is true, 95% of experiments like the one performed must look more 'signal+background'-like than the one that was actually performed.

The problem is to find an estimator (also known as a test statistic) which orders the outcome of the experiments by their 'signal+background'- or 'background'-

likeness. Such an estimator is a test statistics. In a more mathematical language, for the case of n independent counting search analyses, one may define a test statistic X which discriminates 'signal+background'- like outcomes from 'background'-like ones. An optimal choice for the test statistic is the likelihood ratio [145, 146, 147, 148].

For the case of n independent counting search analyses, one may define a test statistic X which discriminates signal-like outcomes from background-like ones. An optimal choice for the test statistic is the likelihood ratio [109, 110, 111]. If the estimated signal in the ith channel is s_i, the estimated background is b_i, and the number of observed candidates is d_i, then the likelihood ratio can be written as

$$X = \prod_{i=1}^{n} X_i, \tag{11.1}$$

with

$$X_i = \frac{e^{(s_i+b_i)}(s_i + b_i)^{d_i}}{d_i!} / \frac{e^{b_i} b_i^{d_i}}{d_i!}. \tag{11.2}$$

This test statistic has the properties that the joint test statistic for the outcome of two channels is the product of the test statistics of the two channels separately, and that it increases monotonically in each channel with the number of candidates d_i.

The confidence level for excluding the possibility of simultaneous presence of new particle production and background (the $s + b$ hypothesis), is

$$CL_{s+b} = P_{s+b}(X \leq X_{obs}), \tag{11.3}$$

i.e., the probability, assuming the presence of both signal and background at their hypothesized levels, that the test statistic would be less than or equal to

that observed in the data. This probability is the sum of Poisson probabilities

$$P_{s+b}(X \le X_{obs}) = \sum_{X(d'_i) \le X(d_i)} \prod_{i=1}^{n} \frac{e^{-(s_i+b_i)}(s_i + b_i)^{d'_i}}{d'_i!}, \qquad (11.4)$$

where $X(d_i)$ is the test statistic computed for the observed set of candidates in each channel d_i, and the sum runs over all possible final outcomes d'_i which have test statistics less than or equal to the observed one.

The confidence level $(1 - CL_{s+b})$ may be used to quote exclusion limits although it has the disturbing property that if too few candidates are observed to account for the estimated background, then any signal, and even the background itself, may be excluded at a high confidence level. It nonetheless provides exclusion of the signal at exactly the confidence level computed. Because the candidates counts are integers, only a discrete set of confidence levels is possible for a fixed set of s_i and b_i.

A typical limit computation, however, involves also computing the confidence level for the background alone,

$$CL_b = P_b(X \le X_{obs}), \qquad (11.5)$$

where the probability sum assumes the presence only of the background. This confidence level has been suggested to quantify the confidence of a potential discovery, as it expresses the probability that background processes would give fewer than or equal to the number of candidates observed. Figure 11.1 shows how the confidences in these hypotheses, CL_s and CL_{s+b} are determined. Then the Modified Frequentist confidence level CL_s is computed as the ratio

$$CL_s = CL_{s+b}/CL_b. \qquad (11.6)$$

This confidence level is a natural extension of the common single-channel $CL = 1 - CL_s$ [3, 4], and for the case of a single counting channel is identical to it.

The task of computing confidence levels for experimental searches with one or more discriminating variables measured for each event reduces to the case of combining counting-only searches by binning each search analyses results in the measured variables. Each bin of, e.g., the reconstructed mass, then becomes a separate search channel to be combined with all others, fol- lowing the strategy of [114] and the neutrino-oscillation example of [115]. In this case, the expected signal in a bin of the reconstructed mass depends on the hypothesized true mass of the particle and also on the expected mass resolution. If the error on the reconstructed mass varies from event to event such that the true resolution is better for some events and worse for others, then the variables s, b, and d may be binned in both the reconstructed mass and its error to provide the best representation of the available information. By exchanging information in bins of the measured variables, different experimental collaborations may share all of their search result information in an unambiguous way without the need to treat the measured variables in any way during the combination.

For convenience, one may add the s_i's, the b_i's, and the d_i's of channels with similar s_i/b_i and retain the same optimal exclusion limit, just as the data from the same search channel may be combined additively for running periods with the same conditions. The same search with a new beam energy or other experimental difference should of course be given its own set of bins (which may be combined with others of the same s_i/b_i).
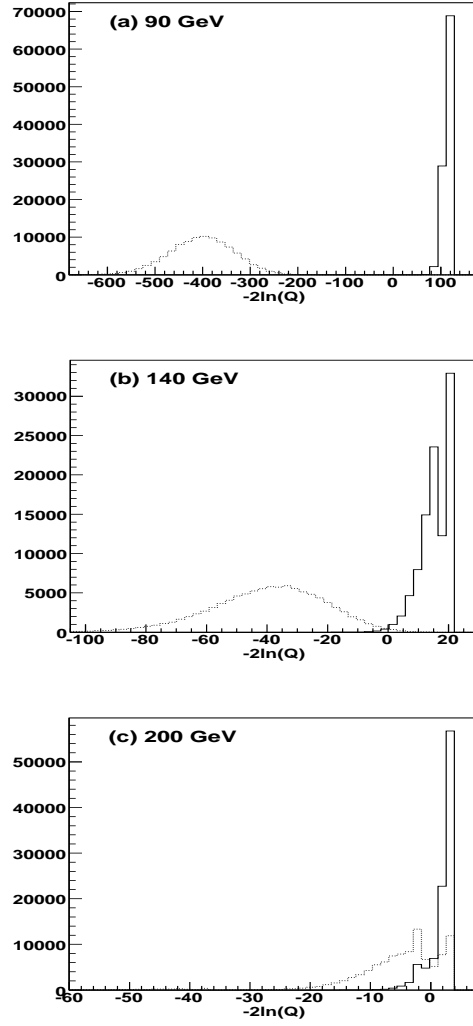
Figure 11.1: A solid line is for background. A dashed line is for signal+background. The evolution of the pdfs with falling search sensitivity from (a) to (c) as the Higgs mass hypothesis is increased and the production cross-section falls. (a) a light higgs with large cross section (b) moderate higgs with moderate cross section (c) a heavy higgs with small cross section.

Chapter 12

Systematic uncertainties

In this chapter the systematic uncertainties for limit calculation are discussed. The source can be divided into two categories: (a) systematic uncertainties that are related to the normalization of Monte Carlo to data, (b) systematic uncertainties contributing from other sources, e.g. charge flip correction and QCD isolation efficiency. Both contributions have to be taken into account to set the correct limit on the mass of a doubly-charged Higgs boson in this analysis. The following various systematic uncertainties on signal and background are taken into account in the limit.

- The systematic uncertainty on the luminosity is estimated to be 6.5%.

- The systematic uncertainty on muon ID correction is 0.7% [116].

- The inclusive Z→ $\mu\mu$ production is normalized to the data using the di-muon data between 60 – 130 GeV after selection S2. The $BR \times \sigma(Z \rightarrow \mu\mu)$ is given in Table 5.2. The systematic error on the normalization using NNLO Mote Carlo background production cross sections is taken to be 5%.

- The theoretical uncertainty on the NLO $H^{\pm\pm}$ production cross section originates from the choice of parton distribution functions and variations of the renormalization and factorization scales. The total contribution is about 10% [55].

- PDF uncertainties $< 4\%$.

- The 27% uncertainty on the k_{flip} ratio applied to like-sign $Z \rightarrow \mu\mu$ is considered. This uncertainty is obtained from the statistical errors of fake rates with following formula.

$$\frac{\sigma_{k_{flip}}}{k_{flip}} = \sqrt{\frac{\sigma_{\epsilon_{\mathrm{data}}}}{\epsilon_{\mathrm{data}}} + \frac{\sigma_{\epsilon_{\mathrm{MC}_{\mathrm{Z}\rightarrow\mu\mu}}}}{\epsilon_{\mathrm{MC}_{\mathrm{Z}\rightarrow\mu\mu}}}} \tag{12.1}$$

- The 9% uncertainty on the QCD isolation efficiency is taken into account. This uncertainty is obtained from the statistical errors of the number of QCD with following formula.

$$\frac{\sigma_{\epsilon_{\mathrm{iso}}}}{\epsilon_{\mathrm{iso}}} = \sqrt{\frac{\sigma_{N_{\mathrm{data}}^{\mathrm{iso},\pm\pm}}}{N_{\mathrm{data}}^{\mathrm{iso},\pm\pm}} + \frac{\sigma_{N_{\mathrm{data}}^{\pm\pm}}}{N_{\mathrm{data}}^{\pm\pm}}} \tag{12.2}$$

The main contribution to the limit setting were found to be to the uncertainties on the normalization of the Monte Carlo backgrounds to data and on the signal cross section. These uncertainties weakens the limit on the mass by about 6 GeV/c^2.

Chapter 13

Results and Conclusions
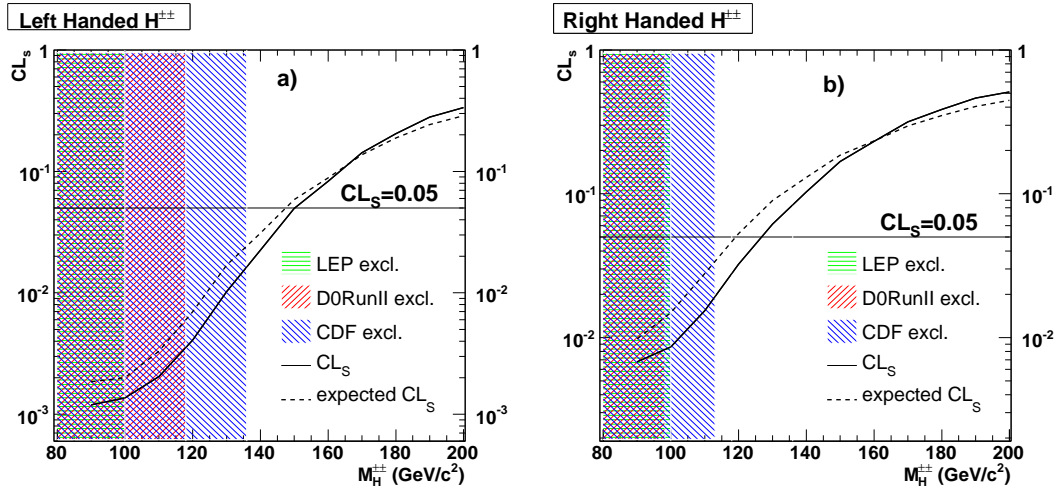
Figure 13.1: Confidence level of the signal, $CL_S = CL_{S+B}/CL_B$, as a function of the mass $M(\mathrm{H}^{\pm\pm})$ of a) left-handed and b) right-handed doubly-charged Higgs boson. The systematic uncertainties are taken into account.

A search for $\mathrm{p\bar{p}} \rightarrow \mathrm{H}^{++}\mathrm{H}^{--} \rightarrow \mu^+\mu^+\mu^-\mu^-$ has been performed. The number of events observed is consistent with expectations from standard model backgrounds. The number of events observed is consistent with expectations

from standard model backgrounds. The three data events and the background events of 3.1±0.5 remained after final cut. Since no excess is observed we proceed to set limits using the CL_S method. We use the di-muon invariant mass distributions to calculate the confidence level. Statistical and systematic errors are considered. The limit calculation are performed using TLimit which has been adapted from the programs MCLIMIT [103]. In Figure 13.1 the confidence level for signal, $CL_S = CL_{S+B}/CL_B$, is shown as a function of the di-muon invariant mass $M(\mathrm{H}^{\pm\pm})$ for a doubly-charged Higgs boson in the absence of signal. The median expected CL_S given the data sample luminosity indicates the sensitivity of the experiment under assumption there is no signal. The cross section limit as a function of the di-muon invariant mass is shown in Figure 13.2 with the cross section of left- and right-handed doubly charged Higgs bosons from theory.

A 95% confidence level mass limit of 150 GeV for left-handed and a mass limit of 126.5 GeV for right-handed doubly-charged Higgs bosons is obtained taking into account the systematic uncertainties described in Chapter 12. This significantly extends the current mass limits of $M(\mathrm{H}_L^{\pm\pm}) > 136$ GeV for left-handed doubly-charged Higgs boson from CDF collaboration. Both mass limits are related to the production cross section of a doubly-charge Higgs boson. The production cross section of a doubly-charged Higgs boson. The production cross section limits are ≤ 20 fb for both a left-handed and a right-handed doubly-charged Higgs boson.
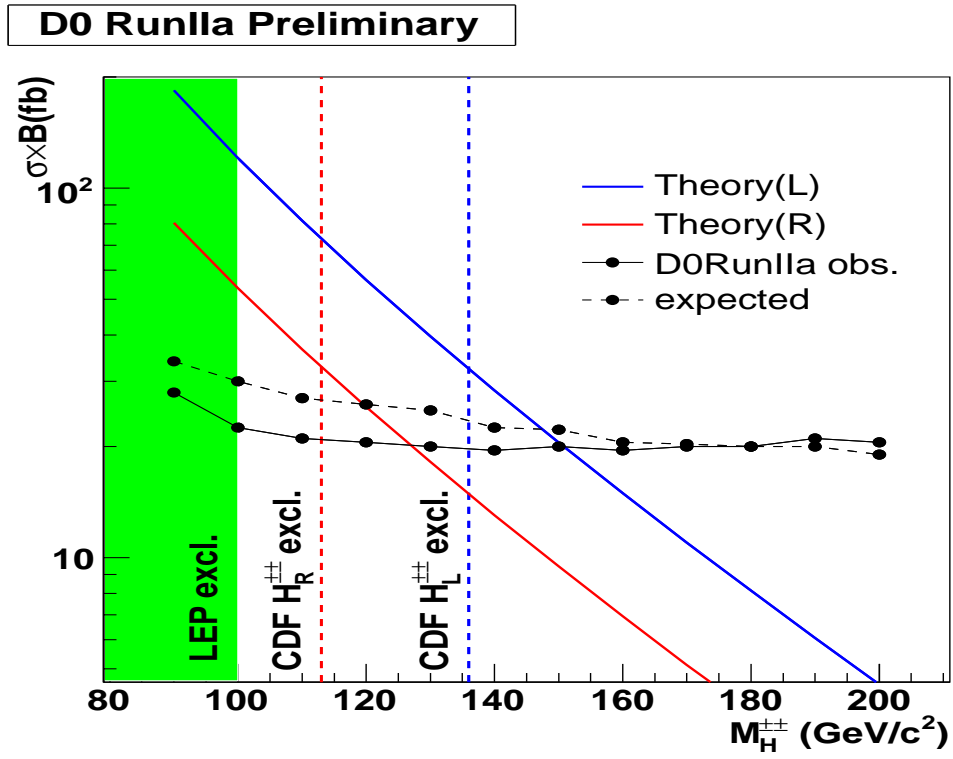
Figure 13.2: The cross section limit as a function of the di-muon invariant mass $M(\mathrm{H}^{\pm\pm})$ at 95% confidence level. The systematic uncertainties are taken into account.

Appendix A

Temperature Control and Monitoring for the CFT

A.1 Detector

Since the fiber detector itself contains no heat generating components, the main possible sources (and sinks) of heat are the Silicon Tracker, and the superconducting coil.

Calculations for the coil show that even in the case of a quench the change in temperature in the outer CFT cylinder would be negligible. A catastrophic failure of the magnet's vacuum jacket could cause a significant drop in the temperature of the outer fiber cylinder, but the system has been designed to ensure that the risk of such a failure is extremely small.

A series of interlocks will ensure that the power to the silicon tracker is shut off in the event of any problem with the silicon cooling system. This will eliminate the risk of heating up the innermost CFT cylinder. When the silicon cooling system is operating, however, the outer region of the silicon detector

will be well below room temperature. To keep the inner CFT cylinder from cooling down, dry gas will flow in the gap between the outside of the silicon tracker and the inner fiber cylinder [117].

A.2 VLPC Temperature Control and Monitoring

The temperature control system for the operation and monitoring of the VLPC readout system is discussed in detail in the VLPC cassette TDR [2]. The following is a brief overview of the system and its key components.

The 1024 channel VLPC cassettes are segmented into eight modules of 128 channels each. Each module has a heater/sensor card (HSC) containing one temperature sensor and 2 heaters. The card is mounted on the bottom of the isotherm which keeps all the VLPCs at a common operating temperature. Since all eight modules within a cassette are thermally coupled, it is expected that a single temperature sensor will be used to control all the heaters within the cassette.

The temperature sensor is a standard 1/4 Watt carbon film resistor with a nominal resistance of 100 Ω at room temperature. The resistance is inversely proportional to temperature and increases to about 500 Ω at 6.5 K, with a sensitivity on the order of 100 Ω per Kelvin. The resistors are mounted on the HSC and then calibrated at Fermilab. The precision of the calibration is better than 1 mK = 0.1 Ω at a temperature of 6.5 K.

The heater resistors are standard metal film resistors of 500 Ω nominal value, 1/8 Watt, which exhibit a resistance of 500 Ω also in the operating temperature range.

Several industrial controllers have been successfully tested for compliance with electrical noise and temperature stability requirements. It is intended to integrate the temperature control and monitoring of the VLPC system into the overall D0 cryogenics control using FIX-DMACS.

Appendix B

Calibration System of the CFT

The calibration system for the fiber tracking detector is being designed to perform several functions. The system will enable the gains of each fiber VLPC channel to be determined, allow monitoring of the stability of the VLPC readout over time, provide a measure of each scintillating fiber's attenuation length as the experiment progresses, and the calibration system will serve as a useful debugging tool during the commissioning of the tracker.

In order to determine the gains of the VLPC channels, the calibration system must be capable of illuminating each VLPC pixel with a small amount of light, typically a few photons. One way to do this is by exciting the scintillating fibers with a radioactive source, but this method has been judged to be difficult and impractical. A second method is to introduce visible light into the fibers, which in turn "pipe" the light down to the VLPCs. This method was successfully employed in the system test. In the test, red LEDs were used to inject light into each scintillating fiber via short (2 meter) clear waveguide fibers mated to the scintillating fibers at the non-readout end of the tracker. Each of the 3,072 LEDs were under computer control and were individually selectable.
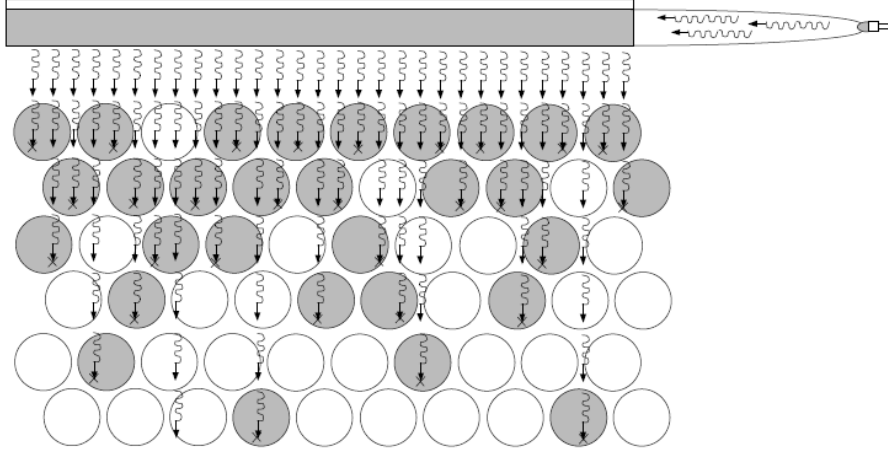
Figure B.1: Blue LED light calibration scheme

More details of this calibration system can be found in reference [119].

Given the success of the calibration method used in the system test, a similar scheme was initially envisaged for the fiber tracker. However, the limited space at the ends of the tracking cylinders make it very difficult to introduce light into the ends of the scintillating fibers. A new method has been devised which uses the availability of new, fast blue LEDs to introduce light through the cladding walls and into the active core of the fiber. The idea, shown schematically in Figure B.1, takes advantage of the fact that the 3HF dye in the fibers have a small, but finite absorption in the blue wavelength range ($\sim$450 nm). When blue light is incident upon several layers of scintillating fiber, as shown in the figure, a small amount is absorbed in the top layer and excites the 3HF dye, producing scintillation photons which are detected by the VLPC. However, since the absorption in this wavelength is small, most of the light travels on into subsequent layers of fiber. In this way the light source can

excite fibers several layers deep, as shown in the figure.

Initial tests of this method were performed at Notre Dame. In these tests, a small number of LEDs (usually two) were inserted into a lucite block covered with a thin diffusing material. The block was placed above a stack of three doublet layers of scintillating fiber. Each fiber layer was 96 fibers wide, but since the readout system available contained only 32 channels of VLPC, very 12th fiber was read out from four of the six fiber layers for a given test. Data were taken for a variety of LED types [120], and at different locations in the lucite block. The results firmly established proof of principle of the technique. As few as two LEDs easily provided enough light to excite fibers in all six layers across the entire 96 fiber ribbon width, and the spectra obtained were adequate for determining the VLPC gain.

In order to apply the blue LED calibration method to the fiber tracker, a means of distributing the light over of the cylindrical geometry of the tracker is necessary. A promising solution to this problem is the optical flat panel, illustrated in Figure B.2. These can be fabricated in several ways, but the basic design consists of a single, thin ribbon of small (typically 500 mm diameter) clear fibers which have been degraded in a certain region so that light is emitted through their cladding wall. At one end of the ribbon, the fibers are bundled together, potted and finished to allow mating with an LED or external optical fiber. Thus external light entering the flat panel through the ends of the fibers is distributed uniformly across a flat, predetermined area. These devices are commonly used in the fabrication of flat panel displays for computers. The panels are extremely light, flexible, and conform easily to a cylindrical surface.

Test samples have been obtained from two manufacturers of these panels [121] and measurements have been performed at Notre Dame to determine
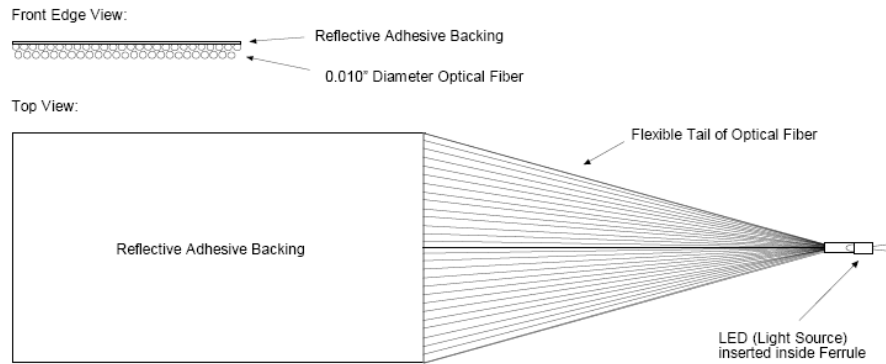
Figure B.2: Schematic view of an optical flat panel

the feasibility of using such devices for the calibration system. The test apparatus was essentially identical to that described above, except that the lucite block with embedded LEDs was replaced with a single optical panel illuminated with a blue LED. The results were very encouraging. Figure B.3 shows spectra from the bottom layer of the 6 layer deep fiber ribbon. The four plots correspond to four fibers spanning the width of the 96 fiber wide ribbon. The spectra clearly show that: 1) sufficient light penetrates the six fiber layers to provide a calibration of even the bottom layer, and 2) the illumination provided by a flat panel with a single LED is very uniform over a ribbon width of order 100 fibers. For the final calibration design, two methods of illuminating the optical panels are under study. In the first method, each panel would have a blue LED coupled directly to its bundle of fibers, at the detector. Each LED, in turn, would be mounted on a small printed circuit board which would provide the necessary electronics to drive the LED. This board is under design at Notre Dame. In the second method, the blue LEDs would be located
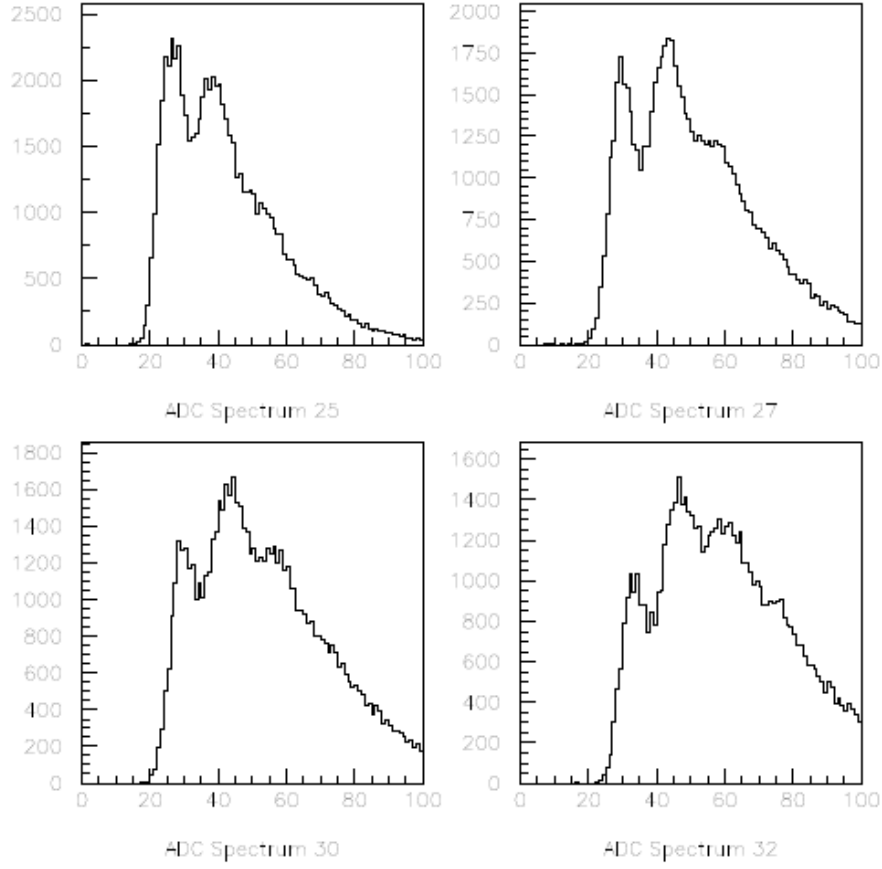
Figure B.3: Spectra from four fibers at the bottom of a six layer deep fiber ribbon, illuminated from above by an optical flat panel with a blue LED.

external to the tracker, and the LED light would be fed to the optical panels via a fiber waveguide. Test prototypes of both methods will be constructed at Notre Dame and compared before the final design decision is taken.

The mounting scheme for the final calibration system is shown schematically in Figure B.4. The flat optical panels are mounted around every scintil-
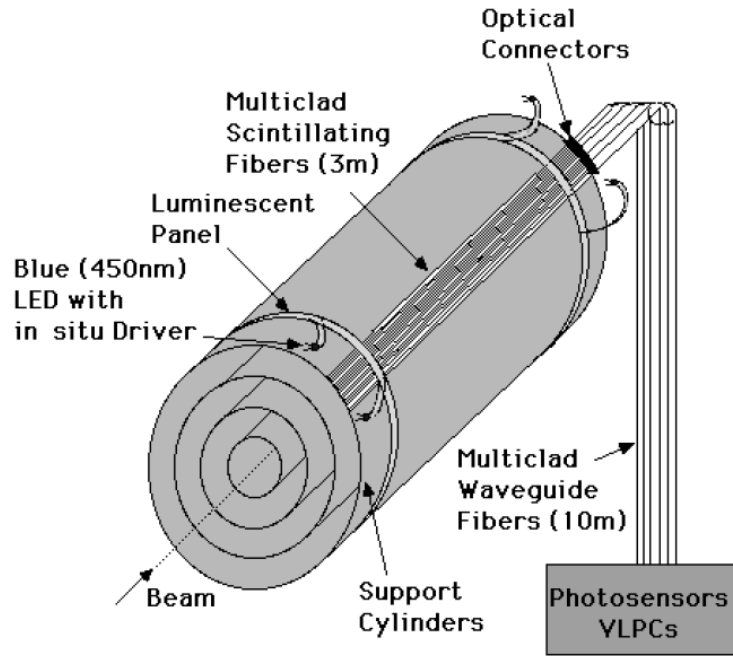
Figure B.4: Illustration of the mounting scheme of flat optical panels for the CFT calibration system

lating fiber cylinder in bands near each end of the cylinder. The bands will be plastic extrusions cut to length to fit each cylinder. Placing two bands on each cylinder provides an extra margin of safety against the failure of an individual optical element. Also, by comparing the total light seen at both ends of the tracker, potential changes in the quality of the scintillating fiber can be monitored over time.

Bibliography

[1] N. G. Deshpande, J. F. Gunion, B. Kayser, Phys. Rev. **D44** (1997) 837.

[2] J. F. Gunion, J. Grifols, A. Mendez, B. Kayser, and F. Olness, Phys. Rev. **D40** (1989) 1546.

[3] J. F. Gunion, C. Loomis, K. T. Pitts, *Searching for Doubly Charged Higgs Bosons at Future Colliders*, hep-ph/9610237;

T. Rizzo, Phys. Rev. D25 (1982) 1355 and Addendum-ibid D27 (1983) 657.

[4] N. Arkani-Hamed et al., JHEP 0208 (2002) 021.

[5] J. F. Gunion, H. E. Haber, G. Kane, S. Dawson, *The Higgs Hunter's Guide*, Frontiers in Physics.

[6] J. F. Gunion, R. Vega, J. Wudka, Phys. Rev. **D42** (1990) 1673.

[7] M. Bando, T. Sato and T. Takahashi, Phys. Rev. **D52** (1995) 3076.

[8] B. Brahmachari, Phys. Rev. **D52** (1995) 1.

[9] B. Brahmachari and R. N. Mohapatra, Phys. Lett. **B357** (1995) 566.

[10] E. Ma, Phys. Rev. **D51** (1995) 236.

[11] D. G. Lee and R. N. Mohapatra, Phys. Rev **D52** (1995) 4125.

[12] J. C. Pati and A. Salam, Phys. Rev. **D10** (1974) 275.

[13] R. N. Mohapatra and J. C. Pati, Phys. Rev. **D11** (1975) 566, 2558.

[14] G. Senjanovic and R. N. Mohapatra, Phys. Rev. **D12** (1975) 1502.

[15] R. N. Mohapatra and R. E. Marshak, Phys. Lett. **91B** (1980) 222.

[16] K. Huitu et al., Nucl. Phys. **B487** (1997) 27.

[17] Morris L. Swartz, Phys. Rev. **D40** (1989) 1521.

[18] T. Yanagida, in Proceedings of *Workshop on Unified Theory and Baryon Number in the Universe, eds.* O. Sawada and A. Sugamoto (KEK 1979)

[19] R. Mohapatra, P. Pal, *Massive Neutrinos in Physics and Astrophysics,* World Scientific Lecture Notes in Physics - Vol. 41, World Scientific Publishing Co. Pte. Ltd., Singapore, ISBN 981-02-0434-5, p. 96-122, (1991).

[20] M. Gell-Mann, P. Ramond and R. Slansky in Supergravity, eds. P. van Niewenhuizen and D. Z. Freedman (North Holland 1979)

[21] Muon (g-2) Collaboration, BNL, *Measurement of the Negative Muon Anomalous Magnetic Moment to 0.7 ppm,* hep-ex/0401008, submitted to Phys. Rev. in January 2004.

[22] J. S. Hagelin, Nucl. Phys. **B193** (1983) 123,
A. J. Buras, W. Slominski, and H. Steger, ibid **B245** (1984) 369.

[23] A. Halprin, Phys. Rev. Lett **48** (1982) 1313.

[24] T. M. Huber et al., Phys. Rev. Lett. **61** (1988) 2189.

[25] F. Cuypers, S. Davidson, *Bileptions: Present Limits and Future Prospects,* PSI-PR-96-21, MPI-PhT/96-45, hep-ph/9609487.

[26] TASSO Collaboration, M. Althoff *et al.*, Zeitschrift für Physik, **C22** (1984) 13, W. Braunschweig *et al., ibid.* **37** (1988) 171.

[27] PLUTO Collaboration, C. Berger *et al.,* Zeitschrift für Physik, **C27** (1985) 341.

[28] HRS Collaboration, M. Derrick *et al.,* Phys. Lett. **B166** (1986) 463,

M. Derrick *et al.,* Phys. Rev. **D34** (1986) 3286.

[29] MAC Collaboration, E. Fernandez *et al.,* Phys. Rev. **D35** (1987) 10.

[30] See for example, R. Engfer and H. K. Walter, Annu. Rev. Nucl. Part. Sci. **36** (1986) 327,

R. E. Shrock, *Report No. ITP-SB-88-28* (1988) (unpublished)

[31] G. K. Leontaris, K. Tamvakis, and J. D. Vergados, Phys. Lett. **B162** (1985) 153.

[32] R. N. Mohapatra, *Quarks, Leptons and Beyond,* proceedings of the NATO Advanced Study Institute, Munich, Cermany, 1983. Edited by H. Fritzsch *et al.*(NATO ASI Series B, Vol 122) (Plenum, New York, 1985),p.219.

[33] U. Bellgardt *et al.,* Nucl. Phys. **B299** (1988) 1.

[34] A. J. Davies, Xiao-Gang He, Phys. Rev. **D43** (1991) 225.

[35] J. P. Leveille, Nucl. Phys. **B137** (1978) 63.

[36] M. L. Schwartz, Phys. Rev. **D40** (1989) 1521,

M. Lusignoli and S. Petrarca, Phys. Lett. **B226** (1989) 397.

[37] M. Mohapatra, Phys. Rev. **D46** (1992) 2990.

[38] A. Zee, Phys. Lett. **B93** (1980) 389.

[39] G. K. Leontaris, K. Tamvakis, J.D. Vergados, Phys. Lett. **B162** (1985) 153.

[40] J. A. Coarasa, A. Mendez, J. Sola, Phys. Lett. **69** (1992) 2475.

[41] J. D. Bjorken, S. Weinberg, Phys. Rev. Lett. **38** (1977) 622.

[42] R. D. Bolton *et al.,* Phys. Rev. **D38** (1988) 2077.

[43] G. W. Bennett, *et al.,* Phys. Rev. Lett. **89**, (2002) 101804. Result published on 2000 data.

[44] A. Yamamoto *et al.,* Nucl. Instrum. Methods Phys. Res. **A491** (2002) 23.

[45] X. Fei, V. W. Hughes and R. Prigl, Nucl. Instrum. Methods Phys. Res. **A394** (1997) 349.

[46] J. Ouyang *et al.*, Nucl. Instrum. Methods Phys. Res. **A374** (1996) 215, S. A. Sedykh *et al.*, Nucl. Instrum. Methods Phys. Res. **A455** (2000) 346.

[47] E. Efstathiadis *et al.*, Nucl. Instrum. Methods Phys. Res. **A496** (2003) 8.

[48] Y. K. Semertzidis *et al.*, Nucl. Instrum. Methods Phys. Res. **A503** (2003) 458.

[49] M. Davier, S. Eidelman,A. Höcker, Z. Zhang, Eur. Phys. J. **C3** (2003) 503.

[50] S. Ghozzi and F. Jegerlehner, hep-ph/0310181, Phys. Lett. **B**, in Press (2004).

[51] OPAL Collab., G. Abbiendi et al., Phys. Lett. **B526** (2002) 221; OPAL Collab., P.D. Action et al., Phys. Lett. **B295** (1992) 347.

[52] L3 Collab., P.Achard, Phys. Lett. **B576** (2003) 18.

[53] DELPHI Collab., J. Abdallah et al., Phys. Lett. **B552** (2003) 127.

[54] OPAL Collab., G. Abbiendi et al., Phys. Lett. **B577** (2003) 93.

[55] M. Mühlleitner, M. Spira, Phys.ReV. **D68** (2003) 117701.

[56] W. Furmanski and R. Petronzio, Zeitschrift für Physik C11 (1982) 293.

[57] V. N. Gribov and L. N. Lipatov, Yad. Fiz. 15 (1972) 781,

G. Altarelli and G. Parisi, Nucl. Phys. **B126** (1977) 298,

Y. L. Dokshitzer, Sov. Phys. JETP 46 (1977) 641.

[58] William Joseph Thompson, Search for the Top Quark in the Muon + Jets channel at D0, PhD Thesis, State University of New York at Stony Brook, Stony Brook, New York, February 1994.

[59] Scott Stuart Snyder, Measurement of the Top Quark Mass at D0, PhD Thesis, State University of New York at Stony Brook, Stony Brook, New York, May 1995.

[60] V. Abazov, et al., in preparation for submission to Nucl. Instrum. Methods Phys. Res. A, and T. LeCompte and H.T. Diehl, The CDF and D0 Upgrades for Run II, Ann. Rev. Nucl. Part. Sci. 50 (2000) 71.

[61] S. Eidelman et al., Phys. Lett. **B592**, 1 (2004).

[62] A. Peisert, Instrumentation in High Energy Physics, ed. F. Sauli, World Scientific, New Jersey, p. 3, (1992).

[63] T. Bose, *Search for B_S^0 oscillations at D0*, Ph.D. Thesis, Columbia University, New York (2005).

[64] UTFit Collaboration, M. Bona *et, al*, hep-ph/0606167, hep-ph/0605213, (2006); updated results at http://utfit.romai,infn.it.

[65] R. Yarema et al., A Beginners Guide to the SVXIIe, Fermilab-TM-1892, October 1996.

[66] M. Utes, SVX Sequencer Board, D0 Engineering Note 3823.110-EN-480, November 1997.

[67] S. Abachi, et al., Nucl. Instrum. Methods Phys. Res. **A338** (1994) 185.

[68] R&D and Optimization Progress Report, D0 Note 1322 (1992).

[69] Step 1 and Beyond, D0 Note 1421 (1992).

[70] D0 Note 1733 (1992).

[71] Magnetic Tracking, D0 Note 1933 (1993).

[72] Electron ID, D0 Submission to the PAC (January, 1994).

[73] S. Mishra and P. McBride, B Physics at Hadron Colliders, Proceedings of the 1993 Snowmass Workshop (1993).

[74] D0 Note 1846 (1993).

[75] C. W. Fabjan, ed. Thomas Ferbel, Experimental Techniques in High-energy Nuclear and Particle Physics,"Second Edition", World Scientific, Singapore, (1991).

[76] C. W. Fabjan, T. Lundlam, Calorimetry in High Energy Physics, Ann. Rev. Nucl. Part. Sci. 32, (1982).

[77] C. W. Fabjan, Detectors for Elementary Particle Physics, CERNPPE/ 94-61, (1996).

[78] C. W. Fabjan et al., Nucl. Inst. and Meth. 141, (1977).

[79] S. Abachi et al., Nucl. Instr. Meth., **A338** (1994) 185-253.

[80] S. Hagopian, The Run II D0 Muon System at the Fermilab Tevatron, submitted to World Scientific, January 2002.

[81] D0 Collaboration, S. Abachi et al., The D0 Upgrade - the Detector and its Physics, FERMILAB-PUB-96-357-E, October 1997.

[82] T. LeCompte and H. T. Diehl, Annu. Rev. Part. Sci. 50, 71 (2000).

[83] D0 Collaboration, S. Abachi et al., The D0 Upgrade - Forward Preshower, Muon System and Level 2 Trigger, D0 Note 2894, FERMILAB-FN-641.

[84] D0 Collaboration, S. Abachi et al., Nucl. Instrum. Methods **A338**, 185 (1994).

[85] D0 Collaboration, B. Baldin et al., Technical Design of the Central Muon System, D0 Note 3365.

[86] D0 Collaboration, G. Alexeev et al., Technical Design of the Forward Muon Tracking Detector Based on Mini-drift Tubes, D0 Note 3366.

[87] D0 Collaboration, V. Abramov et al., Technical Design of the D0 Forward Trigger Scintillation Counters, D0 Note 3237.

[88] D0 Collaboration, G. C. Blazey et al., The D0 Run II Trigger, Xth IEEE Real Time Conference, Beaune, France, 22-26 September 1997, Editor C. E. Vandoni, 83-87.

[89] N. Parashar et al., Real-Time Data Processing in the Muon System of the D0 Detector, IEEE Trans. Nucl. Sci., 47, 276, (2000), FERMILABConf-01-083-E (July 2001).

[90] C. Leonidopoulos, The Muon Trigger at D0 , Proceedings of CHEP 2001 Conference, Beijing, China, Sept 2001.

[91] D0 Upgrade Collaboration, D0 Silicon Tracker Technical Design Report, D0 Note 2169, Fermilab, (1994);

R. Yarema et al., A Beginners Guide to the SVX II Chip, Fermilab-TM-1892, (1994);

D0 Collaboration, The D0 Silicon Microstrip Vertex Detector, NIM paper in preparation.

[92] DØ Collab., Phys. Rev. Lett. **93**, 141801 (2004).

[93] CDF Collab., Phys. Rev. Lett. **93**, 221802 (2004).

[94] Common Sample Group,

http://www-d0.fnal.gov/Run2Physics/cs/skimming/fixPass2p170903.html.

[95] D0 Data Quality Coordination,

http://www-d0.fnal.gov/computing/data_quality/d0_private/forusers.html.

[96] T.Nunnemann, *NNLO Cross-Sections for Drell-Yan, Z and W Production using Modern Parton Distribution Functions*, D0 Note 4476.

[97] N.Kidonakis, R. Vogt, hep-ph/0410367.

[98] http://www-clued0.fnal.gov.gov/~nunne/cross-sections/mcfm_cross-sections.html.

[99] D0 Note 5157, "*Muon Identification Certification for p17data*", section 11.4.

[100] S. Khanov, *A Search for the Associated Higgs Boson Production* $p\bar{p} \to WH \to WWW^* \to l^{\pm}l^{\pm}jj$, D0 Note 5021.

[101] Common Analysis Format,

http://www-d0.fnal.gov/Run2Physics/cs/caf.

[102] B. Tiller, T. Nunnemann, D0 Note 4660.

[103] T. Junk, Nucl. Inst. and Meth., **A434** (1999) 435;

see also http://thomasj.home.cern.ch/thomasj/searchlimits/ecl.html.

[104] P. Bock, CONFL10: A statistics program to compute confidence levels for exclusion or discovery of a signal over background, June 2001.

[105] A. G. Frodesen, O. Skeggestad et al., *Probability and Statistics in Particle Physics*, Universitetsforlaget, 1979, ISBN 82-00-01906-3.

[106] W. T. Eadie, D. Drijard, F. E. James, M. Roos, and B. Sadoulet, *Statistical Methods in Experimental Physics*, North-Holland, 1971, ISBN 0 7204 02395.

[107] M. G. Kendall and A. Stuart, *The Advanced Theory of Statistics*, vol. 2, 2nd ed., ch. 24., Ch. Grin & Company Limited, London, 1967, SBN 85264 011 0.

[108] A. L. Read, *Optimal Statistical Analysis of Search Results based on the Likelihood Ratio and its Application to the Search for the MSM Higgs Boson at $\sqrt{s} = 161$ and 172 GeV*, DELPHI 97-158 PHYS 737 (1997).

[109] A. G. Frodesen, O. Skeggestad, and H. Tfte, *Probability and Statistics in Particle Physics*, Universitetsforlaget, 1979, ISBN 82-00-01906-3.

[110] W. T. Eadie, D. Drijard, F. E. James, M. Roos, and B. Sadoulet, *Statistical Methods in Experimental Physics*, North-Holland, 1971, ISBN 0 7204 02395.

[111] Maurice G. Kendall and Alan Stuart, *The Advanced Theory of Statistics*, vol. 2, 2nd ed., ch. 24. Charles Griffen & Company Limited, London, 1967, SBN 85264 011 0.

[112] B. Escoubes, S. De Unamuno, and O. Helene, *Nucl. Instr. and Meth.* A257, 346 (1987); O. Helene, *Nucl. Instr. and Meth.* **A228**, 120 (1984) and A212, 319 (1983).

[113] Particle Data Group, R. M. Barnett, et al., Phys. Rev. **D54** 1, (1996), and earlier editions.

[114] A. Favara and M. Pieri, *Confidence Level Estimation and Analysis Optimization*, hep-ex/9706016 (1997).

[115] G. J. Feldman and R. D. Cousins, Phys. Rev. **D57**, 3873 (1998).

[116] D0 Note, *"Muon Identification Certification for p17data"*.

[117] J. Warchol (private communication)

[118] "D0 Fiber Tracker 1024 Channel VLPC Cassette Technical Design Report and Specification".

[119] B. Baumbaugh et al., IEEE Trans. Nucl. Sci., Vol. 42, No. 4, 1995, 383-386.

[120] Ledtronics Inc., 4009 Pacific Coast Highway, Torrance, CA 90505; Nichia America Corp., 3775 Hempland Rd., Mountville, PA 17554.

[121] Lumitex Inc., 8443 Dow Circle, Strongsville, OH 44136; Poly-Optical Products Inc., 17475 Gillette Ave., Irvine, CA 92714.